NASA/TM—2013-218081

Understanding the Flow Physics of Shock Boundary-Layer Interactions Using CFD and Numerical Analyses

David J. Friedlander
Glenn Research Center, Cleveland, Ohio

October 2013

NASA STI Program . . . in Profile

Since its founding, NASA has been dedicated to the advancement of aeronautics and space science. The NASA Scientific and Technical Information (STI) program plays a key part in helping NASA maintain this important role.

The NASA STI Program operates under the auspices of the Agency Chief Information Officer. It collects, organizes, provides for archiving, and disseminates NASA's STI. The NASA STI program provides access to the NASA Aeronautics and Space Database and its public interface, the NASA Technical Reports Server, thus providing one of the largest collections of aeronautical and space science STI in the world. Results are published in both non-NASA channels and by NASA in the NASA STI Report Series, which includes the following report types:

- TECHNICAL PUBLICATION. Reports of completed research or a major significant phase of research that present the results of NASA programs and include extensive data or theoretical analysis. Includes compilations of significant scientific and technical data and information deemed to be of continuing reference value. NASA counterpart of peer-reviewed formal professional papers but has less stringent limitations on manuscript length and extent of graphic presentations.

- TECHNICAL MEMORANDUM. Scientific and technical findings that are preliminary or of specialized interest, e.g., quick release reports, working papers, and bibliographies that contain minimal annotation. Does not contain extensive analysis.

- CONTRACTOR REPORT. Scientific and technical findings by NASA-sponsored contractors and grantees.

- CONFERENCE PUBLICATION. Collected papers from scientific and technical conferences, symposia, seminars, or other meetings sponsored or cosponsored by NASA.

- SPECIAL PUBLICATION. Scientific, technical, or historical information from NASA programs, projects, and missions, often concerned with subjects having substantial public interest.

- TECHNICAL TRANSLATION. English-language translations of foreign scientific and technical material pertinent to NASA's mission.

Specialized services also include creating custom thesauri, building customized databases, organizing and publishing research results.

For more information about the NASA STI program, see the following:

- Access the NASA STI program home page at *http://www.sti.nasa.gov*

- E-mail your question to *help@sti.nasa.gov*

- Fax your question to the NASA STI Information Desk at 443–757–5803

- Phone the NASA STI Information Desk at 443–757–5802

- Write to:
  STI Information Desk
  NASA Center for AeroSpace Information
  7115 Standard Drive
  Hanover, MD 21076–1320

NASA/TM—2013-218081

Understanding the Flow Physics of Shock Boundary-Layer Interactions Using CFD and Numerical Analyses

David J. Friedlander
Glenn Research Center, Cleveland, Ohio

National Aeronautics and
Space Administration

Glenn Research Center
Cleveland, Ohio 44135

October 2013

Acknowledgments

The author would like to acknowledge the support from the Air Force Research Laboratory, Air Vehicle Directorate, AFRL/RB and the interaction with the U.S. Air Force Collaborative Center for Aeronautical Sciences as well as the NASA Fundamental Aeronautics Program for supporting this research. The author would also like to thank NASA's High End Computing Program (HECC) for providing super-computing resources that were vital in this endeavor. Also appreciated is the base grid (of which all grids used in this thesis were derived from) and grid modification codes that were developed by Marshall Galbraith and guidance from Daniel Galbraith. A special thanks goes to Dr. Mark Turner, Dr. Paul Orkwis, and Dr. Nicholas Georgiadis for all their guidance and support with this thesis work.

Level of Review: This material has been technically reviewed by technical management.

Available from

NASA Center for Aerospace Information
7115 Standard Drive
Hanover, MD 21076–1320

National Technical Information Service
5301 Shawnee Road
Alexandria, VA 22312

Available electronically at http://www.sti.nasa.gov

Understanding the Flow Physics of Shock Boundary-Layer Interactions Using CFD and Numerical Analyses

David J. Friedlander
National Aeronautics and Space Administration
Glenn Research Center
Cleveland, Ohio 44135

Abstract

Mixed compression inlets are common among supersonic propulsion systems. However they are susceptible to total pressure losses due to shock/boundary-layer interactions (SBLI's). Because of their importance, a workshop was held at the 48th American Institute of Aeronautics and Astronautics (AIAA) Aerospace Sciences Meeting in 2010 to gauge current computational fluid dynamics (CFD) tools abilities to predict SBLI's. One conclusion from the workshop was that the CFD consistently failed to agree with the experimental data. This thesis presents additional CFD and numerical analyses that were performed on one of the configurations presented at the workshop.

The additional analyses focused on the University of Michigan's Mach 2.75 Glass Tunnel with a semi-spanning 7.75 degree wedge while exploring key physics pertinent to modeling SBLI's. These include thermodynamic and viscous boundary conditions as well as turbulence modeling. Most of the analyses were 3D CFD simulations using the OVERFLOW flow solver. However, a quasi-1D MATLAB code was developed to interface with the National Institute of Standards and Technology (NIST) Reference Fluid Thermodynamic and Transport Properties Database (REFPROP) code to explore perfect verses non-ideal air as this feature is not supported within OVERFLOW. Further, a grid resolution study was performed on the 3D 56 million grid point grid which was shown to be nearly grid independent. Because the experimental data was obtained via particle image velocimetry (PIV), a fundamental study pertaining to the effects of PIV on post-processing data was also explored.

Results from the CFD simulations showed an improvement in agreement with experimental data with certain settings. This is especially true of the v velocity field within the streamwise data plane. Key contributions to the improvement include utilizing a laminar zone upstream of the wedge (the boundary-layer was considered transitional downstream of the nozzle throat) and the necessity of mimicking PIV particle lag for comparisons. It was also shown that the corner flow separations are highly sensitive to the turbulence model. However, the center flow region, where the experimental data was taken, was not as sensitive to the turbulence model. Results from the quasi-1D simulation showed that there was little difference between perfect and non-ideal air for the configuration presented.

Table of Contents

Abstract iii

List of Figures viii

List of Tables xiii

Nomenclature xiv

1 Background 1

1.1 Introduction . . . 1

1.2 Experimental Research Literature Survey . . . 3

1.3 Computational Research Literature Search . . . 4

2 Geometry and Numerical Modeling 10

2.1 Geometry and Mesh . . . 10

2.2 Solver . . . 13

3 Case Overviews 15

3.1 CFD Cases with OVERFLOW . . . 15

3.2 PIV Exploration . . . 18

4 Flat Plate 20

4.1 Overview . . . 20

4.2 Results . . . 21

5 Quasi-1D Code 24

5.1 Overview . . . 24

5.2 Calorically Perfect Code . . . 25

5.3 Non-Ideal Code . . . 28

5.4 Quasi-1D Exploration . . . 31

6 Grid Resolution Study 33

7 Results **37**

7.1 Standard Case . . . 37

7.2 Particle Lag Effects . . . 38

7.3 Isothermal Case . . . 41

7.4 Trip Case . . . 45

7.5 Turbulence Modeling Effects . . . 47

7.6 Metrics . . . 50

7.7 Blockage Revisited . . . 54

8 Conclusions/Future Work **56**

References **58**

A Velocity Contours **64**

B Velocity Profiles **68**

B.1 Standard Case . . . 68

B.2 Combined Case . . . 71

B.3 Modified Geometry, Isothermal, and Trip Cases . . . 74

B.4 TKE and MUT Cases . . . 77

B.5 Standard Case with Various Turbulence Models . . . 80

C Combined Case with Various Turbulence Models **83**

D Shock Angle Calculation **88**

E Simulation Checklists **91**

E.1 Initial . . . 91

E.2 Standard Case . . . 92

E.3 Isothermal Case . . . 93

E.4 Modified Geometry Case . . . 94

E.5 All-Laminar Case . . . 95

E.6 Trip Case . . . 96

E.7 Combined Case . . . 97

E.8 TKE Case . . . 98

E.9 MUT Case . . . 99

E.10 Standard Case with SST-GY 100
E.11 Standard Case with BSL 101
E.12 Flat Plate with SST 102
E.13 Flat Plate with K-Omega 103
E.14 Flat Plate with SST-GY 104
E.15 Flat Plate with BSL 105

List of Figures

1 A supersonic mixed compression inlet (used with permission from Pitt Ford and Babinsky [1]). 1

2 Sketch of the oblique shock / boundary-layer interaction (used with permission from Touber and Sandham [2]). 1

3 Iso-surfaces of density gradients in the downstream direction around the wedge, colored by the derivative of the density gradients in the downstream direction (from Galbraith [3]). . . . 2

4 Datum groove, 8mm wide groove and variations (from Holden and Babinsky [4]). 3

5 Three-dimensional bumps (from Holden and Babinsky [4]). 4

6 Velocity profiles 94 mm downstream of micro-ramp controlled SBLI, h = 3 mm (used with permission from Pitt Ford and Babinsky [1]). 4

7 Mach number contours of the converged mesoflap array simulations, (used with permission from Ghosh et al. [5]). 5

8 Contours of the skin friction coefficient of a flat plate SBLI with time averaged (top) and instantaneous (bottom) snapshots (from Morgan et al. [6]). 6

9 Comparison of RANS and LES results on a square duct (from Medic et al. [7]). 6

10 Configurations run with DNS, LES, and RANS (used with permission from Knight et al. [8]). 7

11 Flow pattern sketches for the experiment (left) and DNS (right) for a 24 degree compression corner (from Wu et al. [9]). 8

12 Comparison of the size of the separation bubble with (new) and without (old) a dissipation limiter (from Wu and Martin [10]). 8

13 Skin friction distribution (RANS models) for a 28 degree compression corner at Mach 5 (used with permission from Edwards et al. [11]). 9

14 Cut-away view of the University of Michigan Glass Tunnel (from Lapsa [12]). 10

15 Schematic of the University of Michigan Glass Tunnel with upstream flow straightener and seeder (from Lapsa [12]). Note units are in inches. 11

16 7.75 degree wedge geometry. Dimensions courtesy of Lapsa [12]. 11

17 Grid throat region packing with original (left) and final (right). 12

18 Side view of the grid representing the tunnel and 7.75 degree wedge with center-span wedge and throat inserts shown. 12

19 Sample modified nozzle contour. Note the difference between the old and new throat heights is exaggerated compared to what was actually used. 16

20 Momentum thickness Reynolds number at the bottom wall (half-span) for the laminar case. . 17

21 Momentum thickness Reynolds number at the bottom wall, center-span. 17
22 Measured particle response through an oblique shock (from Lapsa [12]). The velocity component normal to the shock, u_n, is normalized by the pre-shock (u_{n1}) and post-shock (u_{n2}) velocities and shown as a function of the shock-normal direction, n. An exponential fit to the data reveals the particle relaxation time, $\tau p = 5.5$ µs. 19
23 Flat plate 2D grid and boundary conditions [13]. 20
24 Skin friction coefficient profiles. 21
25 u^+ verses y^+ for the various turbulence models at $Re_x = 4.2E6$. 22
26 Normalized turbulent parameters for various turbulence models at $Re_x = 4.2E6$ 23
27 Normalized turbulent parameters at various freestream turbulent viscosities at $Re_x = 4.2E6$. 23
28 Sample enthalpy verses entropy diagram for calculating across an oblique shock for a non-ideal gas. 1: total conditions at Station 1, 1S: static conditions at Station 1, 2S: static conditions at Station 2, 2: total conditions at Station 2. 24
29 Oblique shock notation. 25
30 Percentage differences between non-ideal and perfect air for various parameters. 32
31 Percentage differences of the shock angle between non-ideal and perfect air for varying wedge angles. 32
32 Streamwise cross-sections at center-span for the various grid levels. 33
33 L2 residuals for the Standard case. 34
34 u velocity profiles within the streamwise plane. 35
35 Data plane location in reference to the grid. 37
36 u velocity (left) and v velocity (right) streamwise contours for the experiment (top) and Standard case (bottom). 38
37 Bottom wall separation underneath the wedge for the Standard case. 38
38 v velocity streamwise contours for the experiment (top), short lag (middle-top), medium lag (middle-bottom), and long lag (bottom). 39
39 Select velocity profiles at the most-upstream axial location ($x = 18.191$ mm) for the Standard case. 40
40 Select velocity profiles at the first intersecting spanwise plane ($x = 20.76$ mm) for the Standard case. 40
41 Select velocity profiles at the most-upstream axial location ($x = 18.191$ mm) for the Combined case. 41

42 Select velocity profiles at the first intersecting spanwise plane ($x = 20.76$ mm) for the Combined case. . . . 41
43 Freestream thermal boundary-layer at $x = -63.9$ mm. Temperature cut off is at 99% freestream (121.2 K). . . . 42
44 Temperature profiles at the most-upstream axial location ($x = 18.191$ mm). . . . 43
45 Total temperature centerspan profile at the bottom wall with the following stations marked: 1. Throat, 2. Trip location, 3. Start of the tunnel straight section, 4. Wedge leading edge, 5. Wedge trailing edge. . . . 43
46 Select velocity profiles at the most-upstream axial location ($x = 18.191$ mm). . . . 44
47 u velocity difference contours. . . . 44
48 v velocity difference contours. . . . 44
49 Static temperature difference contours. . . . 45
50 Select velocity profiles at the most-upstream axial location ($x = 18.191$ mm). . . . 45
51 Select velocity profiles at the first intersecting spanwise plane ($x = 20.76$ mm). . . . 46
52 Turbulent kinetic energy profiles. . . . 46
53 Select velocity profiles at the most-upstream axial location ($x = 18.191$ mm). . . . 47
54 Select velocity profiles at the first intersecting spanwise plane ($x = 20.76$ mm). . . . 48
55 Turbulent kinetic energy profiles. . . . 48
56 Velocity profiles at the most-upstream axial location ($x = 18.191$ mm) for various turbulence models, Standard Case. . . . 49
57 Velocity profiles at the first intersecting spanwise plane ($x = 20.76$ mm) for various turbulence models, Standard Case. . . . 49
58 Bottom wall separation underneath the wedge for the Standard case with various turbulence models. . . . 50
59 Point locations within the centerspan plane. Mach number contour of the Standard case CFD solution is shown. . . . 52
60 Shock angle verses Mach number. . . . 53
61 Bottom wall separation underneath the wedge for the Isothermal and Modified Geometry cases. 54
62 Bottom wall separation underneath the wedge for the Trip and Combined cases. . . . 55
A.1 u velocity contours for the Standard (left) and Combined (right) cases with lag. . . . 64
A.2 u (left) and v (right) velocity contours for Isothermal and Modified Geometry cases. . . . 65
A.3 u (left) and v (right) velocity contours for Trip and Combined cases. . . . 65
A.4 u (left) and v (right) velocity contours for TKE and MUT cases. . . . 66

A.5 u (left) and v (right) velocity contours for the Standard case with SST-GY and BSL. 66
A.6 u (left) and v (right) velocity contours for the Combined case with SST-GY and BSL. 67
B.1 Velocity profiles at $x = 26.76$ mm, Standard case. 68
B.2 Velocity profiles at $x = 30.76$ mm, Standard case. 68
B.3 Velocity profiles at $x = 34.76$ mm, Standard case. 69
B.4 Velocity profiles at $x = 38.76$ mm, Standard case. 69
B.5 Velocity profiles at $x = 41.76$ mm, Standard case. 70
B.6 Velocity profiles at $x = 53.76$ mm, Standard case. 70
B.7 Velocity profiles at $x = 26.76$ mm, Combined case. 71
B.8 Velocity profiles at $x = 30.76$ mm, Combined case. 71
B.9 Velocity profiles at $x = 34.76$ mm, Combined case. 72
B.10 Velocity profiles at $x = 38.76$ mm, Combined case. 72
B.11 Velocity profiles at $x = 41.76$ mm, Combined case. 73
B.12 Velocity profiles at $x = 53.76$ mm, Combined case. 73
B.13 Velocity profiles at $x = 26.76$ mm, various cases. 74
B.14 Velocity profiles at $x = 30.76$ mm, various cases. 74
B.15 Velocity profiles at $x = 34.76$ mm, various cases. 75
B.16 Velocity profiles at $x = 38.76$ mm, various cases. 75
B.17 Velocity profiles at $x = 41.76$ mm, various cases. 76
B.18 Velocity profiles at $x = 53.76$ mm, various cases. 76
B.19 Velocity profiles at $x = 26.76$ mm, TKE and MUT cases. 77
B.20 Velocity profiles at $x = 30.76$ mm, TKE and MUT cases. 77
B.21 Velocity profiles at $x = 34.76$ mm, TKE and MUT cases. 78
B.22 Velocity profiles at $x = 38.76$ mm, TKE and MUT cases. 78
B.23 Velocity profiles at $x = 41.76$ mm, TKE and MUT cases. 79
B.24 Velocity profiles at $x = 53.76$ mm, TKE and MUT cases. 79
B.25 Velocity profiles at $x = 26.76$ mm, Standard case with various turbulence models. 80
B.26 Velocity profiles at $x = 30.76$ mm, Standard case with various turbulence models. 80
B.27 Velocity profiles at $x = 34.76$ mm, Standard case with various turbulence models. 81
B.28 Velocity profiles at $x = 38.76$ mm, Standard case with various turbulence models. 81
B.29 Velocity profiles at $x = 41.76$ mm, Standard case with various turbulence models. 82
B.30 Velocity profiles at $x = 53.76$ mm, Standard case with various turbulence models. 82
C.1 Velocity profiles at $x = 18.191$ mm, Combined case with various turbulence models. 83

C.2 Velocity profiles at $x = 20.76$ mm, Combined case with various turbulence models. 84
C.3 Velocity profiles at $x = 26.76$ mm, Combined case with various turbulence models. 84
C.4 Velocity profiles at $x = 30.76$ mm, Combined case with various turbulence models. 85
C.5 Velocity profiles at $x = 34.76$ mm, Combined case with various turbulence models. 85
C.6 Velocity profiles at $x = 38.76$ mm, Combined case with various turbulence models. 86
C.7 Velocity profiles at $x = 41.76$ mm, Combined case with various turbulence models. 86
C.8 Velocity profiles at $x = 53.76$ mm, Combined case with various turbulence models. 87
C.9 Bottom wall separation underneath the wedge for the Combined case with various turbulence models. 87
D.1 Shock angle diagram/nomenclature. 89
D.2 Velocity profiles for determining shock line end location (Standard case shown). 89
D.3 Arc length profile for determining shock line end location (Standard case shown). 89
D.4 Derivative profiles for determining shock line end location (Standard case shown). 90

List of Tables

1 Summary of CFD Cases. 18

2 Various flow parameters used to determine grid convergence. 35

3 Mass flow rates (kg/s) used to determine grid convergence. 35

4 Coordinates for grid resolution study. 36

5 Workshop error metric comparisons. 51

6 u velocity and velocity differences. 52

7 Shock angle comparisons. 53

Nomenclature

Acronyms

AGS	Abu-Ghannam and Shaw
AIAA	American Institute of Aeronautics and Astronautics
CFD	Computational Fluid Dynamics
DNS	Direct Numerical Simulation
LES	Large-Eddy Simulation
NIST	National Institute of Standards and Technology
PIV	Particle Image Velocimetry
RANS	Reynolds-Averaged Navier-Stokes
SBLI	Shock Boundary Layer Interaction
SST	Shear Stress Transport
UM	University of Michigan
VG	Vortex Generator
a	speed of sound
$A/A*$	geometric throat area ratio
$b*$	throat blockage parameter
C	constant
c_f	skin friction coefficient
c_p	specific heat at constant pressure
$E(f)$	error metric of f
$e(f)_n$	local error of f
f	function/lookup
h	enthalpy

i, n	index
k	turbulent kinetic energy
L	length scale
l	arc length
M	Mach number
m	power coefficient
$\dot{m}*$	geometric throat mass flow rate
p	pressure
R	specific gas constant
r_c	thermal recovery factor
Re	Reynolds number
s	entropy
T	temperature
u, v	streamwise and transverse velocity components
V	velocity
x, y, z	cartesian coordinates
$\tilde{x}$, $\tilde{y}$	adjusted cartesion coordinates
y^+, u^+	wall coordinates

Greek Symbols

β	shock angle
γ	ratio of specific heats
θ	turning/wedge angle
κ	Von Karmin constant
μ	dynamic viscocity

ρ density

τ time constant

Subscripts

$_1$ upstream

$_2$ downstream

$_{\infty}$, $_{Inf}$ freestream condition

$_n$ normal

$_{ref}$ reference condition

$_*$ sonic condition

$_T$ turbulent

$_t$ total condition

1 Background

1.1 Introduction

Mixed compression inlets are often found in supersonic aircraft propulsion systems with a typical mixed compression inlet shown in Fig. 1. These inlets are susceptible to shock boundary-layer interactions (SBLI) with a typical SBLI shown in Fig. 2. As one can see, SBLI's are not trivial in nature and beyond the situation shown in Fig. 2, are very three dimensional flows, shown in Fig. 3. SBLI's are a concern for supersonic aircraft propulsion system designs as the separation induced by the shock interacting with the turbulent boundary-layer results in a total pressure loss that is not accounted for in inviscid theory. As mixed compression inlets become more at the forefront of aviation technology, it becomes crucial to understand SBLI's and how they affect propulsion system performance. This can be achieved in several ways, including fundamental and flow control experiments as well as computational work, all of which will be discussed further in the next sections.

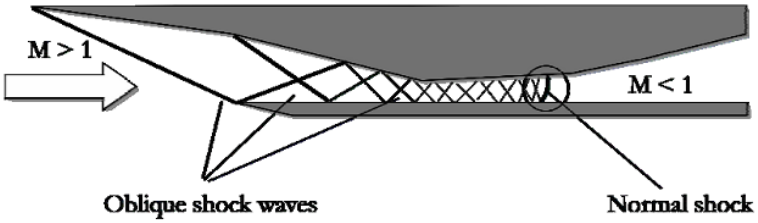

Figure 1: A supersonic mixed compression inlet (used with permission from Pitt Ford and Babinsky [1]).

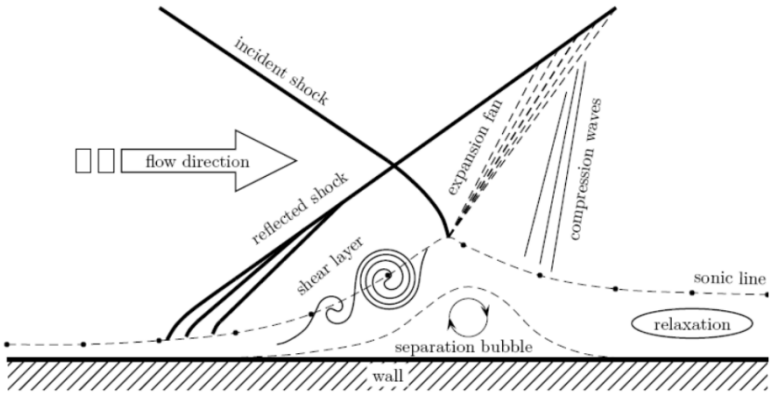

Figure 2: Sketch of the oblique shock / boundary-layer interaction (used with permission from Touber and Sandham [2]).

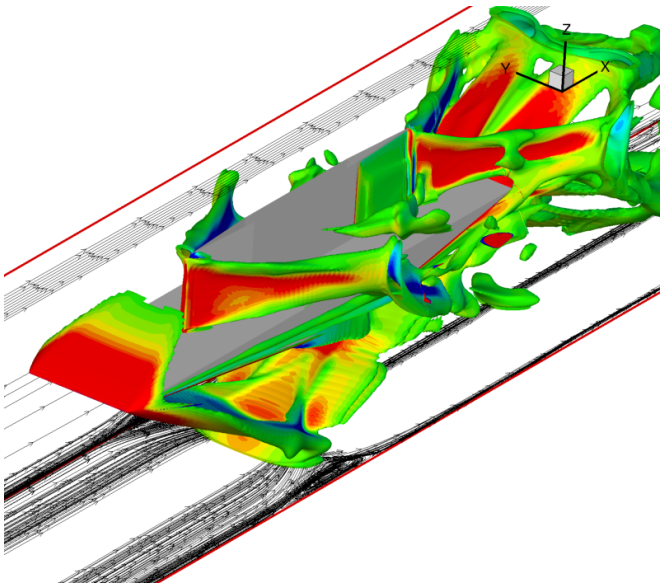

Figure 3: Iso-surfaces of density gradients in the downstream direction around the wedge, colored by the derivative of the density gradients in the downstream direction (from Galbraith [3]).

In order to determine how effectively computational fluid dynamics (CFD) tools can currently predict SBLI's, a workshop was held at the 48th American Institute of Aeronautics and Astronautics (AIAA) Aerospace Sciences Meeting featuring an array of CFD analyzes [14, 15, 16] with experimental data sets provided by the Institut Universitaire des Systemes Thermiques Industriels [17] and the University of Michigan (UM) [18]. The CFD results from the workshop are summarized in DeBonis et al. [19] with workshop conclusive remarks documented in works by Benek et al. [20, 21] as well as Hirsch [22]. One key conclusion of the workshop was that the CFD analyses failed to match experimental data. Because of the complex nature of SBLI's, it is of great interest within the aero-propulsion and CFD communities to see if there are ways to improve CFD methods or more effectively use existing methods. This will enable better prediction of SBLI's as well as aid in future inlet design.

Thus further CFD analyses were performed at the University of Cincinnati's Gas Turbine Simulation Laboratory as a compliment to work done by Galbraith [3, 23] in hopes to better understand the computational factors involved in calculating SBLI's as well as to explore alternatives to the error metric used in the workshop. One of the data sets provided to the workshop by UM was their Glass Tunnel with a semi-spanning 7.75 degree wedge at a freestream Mach number of 2.75. The UM experimental data was obtained using stereo particle image velocimetry (PIV) techniques [18]. The CFD analyses presented here focus on that particular UM case while exploring various key physics associated with SBLI's, including, but not limited to, heat transfer boundary conditions, geometry sensitivities, laminar verses turbulent flow assumptions, and turbulence modeling. Special attention was paid to the u and v velocity components,

particularly around the oblique shock off the leading edge of the wedge. This is because it was felt that the CFD and post-processing calculations from the workshop missed the peak u velocity as well as the location of the shock as defined by the v velocity profile. If the upstream profiles are not in agreement, it is fair to say that the solutions downstream should not agree. Aside from the CFD cases, a preliminary exploration into the effects on PIV obtained data is also presented.

1.2 Experimental Research Literature Survey

The workshop was not the first and certainly not the last time SBLI's have been examined both experimentally and numerically. Experiments by Holden and Babinsky [4] attempted SBLI flow control via a series of streamwise grooves and bumps, shown in Figs. 4 and 5, with hopes of smearing the shock footprint. They showed that the flow fields inherent with SBLI's are highly sensitive to geometry deviations, such as the slot and bump geometries, or for that matter any foreign debris or geometry imperfections. Another experiment by Holden and Babinsky [24] explored the use of vortex generators (VG's) for SBLI flow control. Two types were tested: wedge-shaped, more commonly known as micro-ramps, and counter rotating vanes. It was found that the use of the VG's greatly reduced the separation region of the SBLI interaction region, with the vane type VG's going as far as to eliminate the separation region completely. Experiments by Pitt Ford and Babinsky [1] as well as by Lapsa [12] also explored the effects of micro-ramps on SBLI flow fields. Pitt Ford and Babinsky showed that micro-ramps located upstream of the interaction region can break up the separation bubble but not completely eliminate it while increasing downstream velocities, shown in Fig. 6. Lapsa showed that the use of inverse micro-ramps can decrease the displacement thickness and thus allow for less separation around the interaction region.

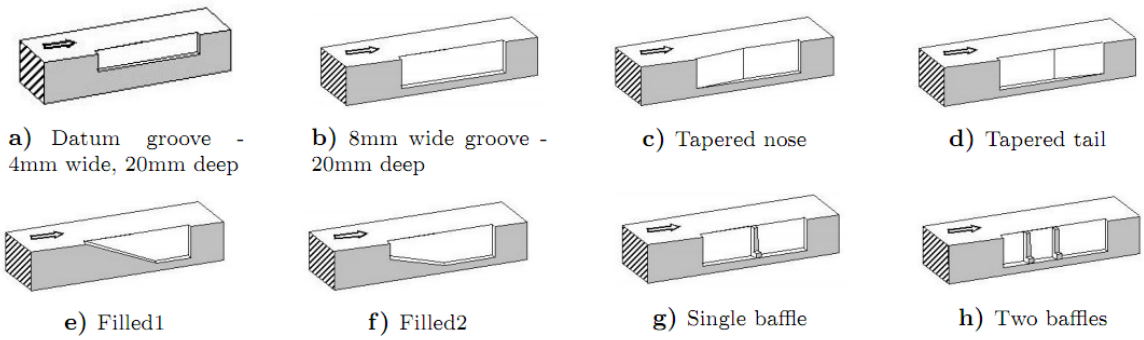

Figure 4: Datum groove, 8mm wide groove and variations (from Holden and Babinsky [4]).

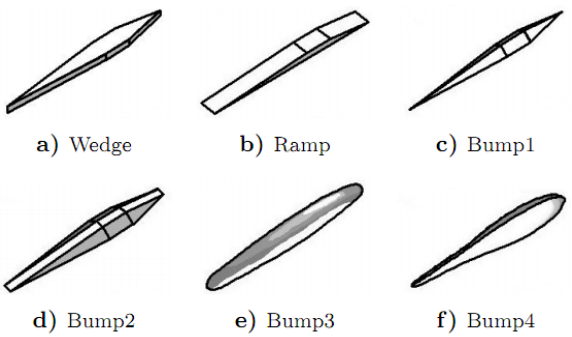

Figure 5: Three-dimensional bumps (from Holden and Babinsky [4]).

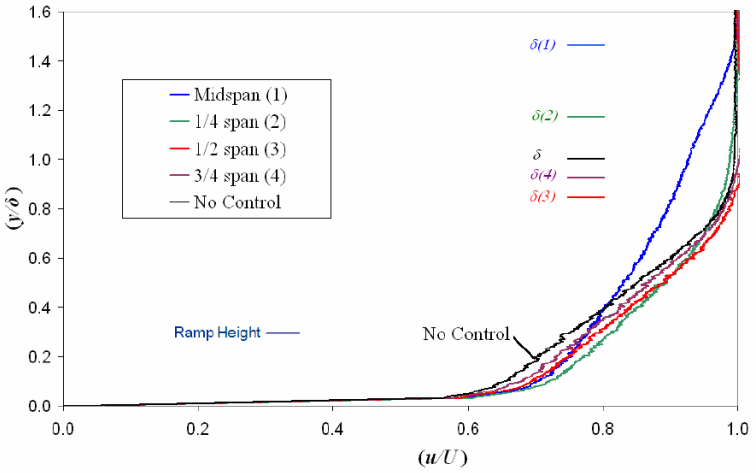

Figure 6: Velocity profiles 94 mm downstream of micro-ramp controlled SBLI, h = 3 mm (used with permission from Pitt Ford and Babinsky [1]).

While the above mentioned experiments focused mostly on flow control, more fundamental experiments have been performed in order to understand the nature of SBLI's. An experiment performed by Babinsky et al. [25] explored the importance of corner flows in relation to SBLI's. They showed that the corner flow separations have a coupled effect with the separation bubble of the interaction region of SBLI's. Thus by decreasing the corner flow separation it was shown that the interaction region separation would be reduced and approach a 2D nature. This coupling nature was also shown in a prior experiment by Titchener et al. [26].

1.3 Computational Research Literature Search

Over the years there have been plenty of numerical simulations exploring all facets of SBLI's: from flow control to numerical modeling efforts. For flow control, Ghosh et al. [5] investigated the use of aeroelastic mesoflaps via two and three dimensional simulations, shown in Fig. 7. The simulations utilized both

Reynolds-Averaged Navier-Stokes (RANS) and Large-Eddy/Reynolds-Averaged Navier-Stokes (LES/RANS) means for solving the flow equations. The simulations showed that the use of mesoflaps for flow control resulted in a slightly larger interaction region compared to the non-controlled case.

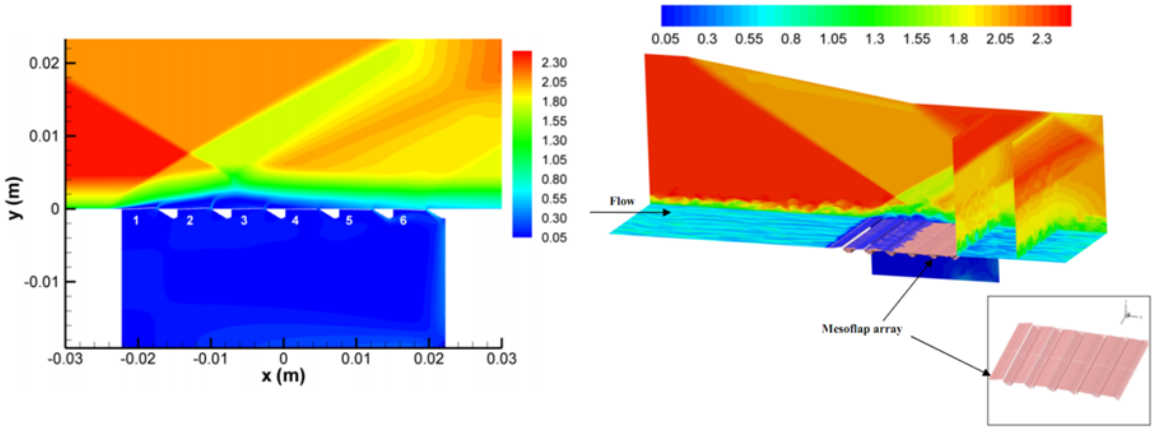

Figure 7: Mach number contours of the converged mesoflap array simulations, (used with permission from Ghosh et al. [5]).

Morgan et al. [6] performed LES simulations with a flat plate geometry to explore SBLI's. An instantaneous as well as time-averaged snapshot of the skin friction coefficient within the interaction region is shown in Fig. 8. It can be seen that the time-averaged snapshot greatly smooths out the chaotic nature of the SBLI, including the separation region. In fact, the instantaneous snapshot shows that the separation region consists of many separation bubbles and not just a single separation zone as shown in the time-averaged snap shot. This is important as steady RANS simulations only have the capability to reproduce time-averaged behavior unlike LES instantaneous solutions. The comparison between LES and RANS solutions were further explored by Medic et al. [7] using a simple square duct with results shown in Fig. 9. It can be seen that the RANS solution over predicts the boundary layer growth at the duct corners relative to the LES solution. This over prediction can have a tremendous effect in SBLI simulations, especially when using a tunnel-like geometry, due to the coupling effects between the corner flows and interaction region separation discussed earlier. Other LES solution efforts have been conducted by Hunt and Nixon [27], based on experimental data obtained by Dolling and Murphy [28], as well as by Jamalamadaka et al. [29].

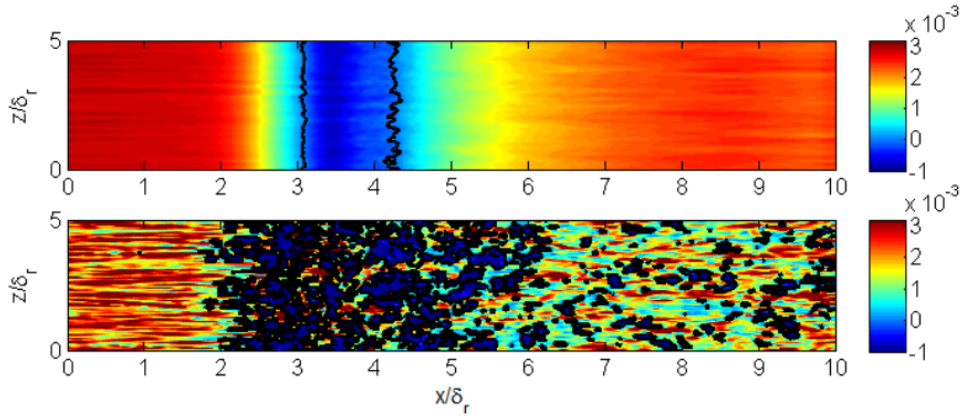

Figure 8: Contours of the skin friction coefficient of a flat plate SBLI with time averaged (top) and instantaneous (bottom) snapshots (from Morgan et al. [6]).

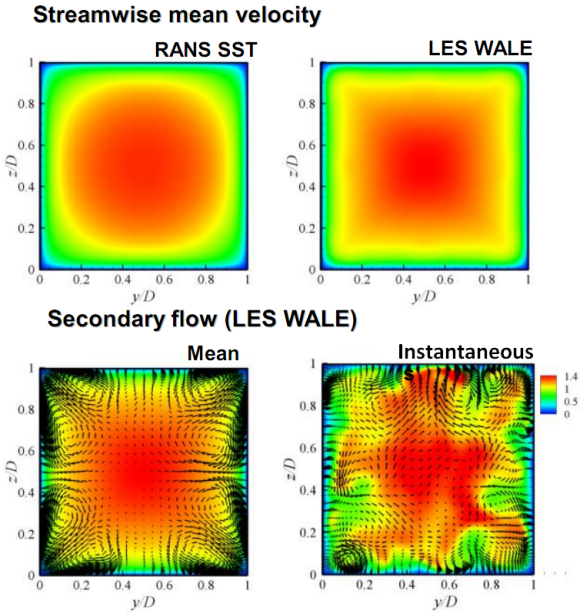

Figure 9: Comparison of RANS and LES results on a square duct (from Medic et al. [7]).

Further, a series of simulations were performed by Knight et al. [8] exploring SBLI's. Five configurations were run, shown in Fig. 10, and utilized Direct Numerical Simulations (DNS), LES, and RANS. There were a multitude of lessons learned from these simulations, especially regarding the RANS simulations. With RANS, the case of the 3D single fin correctly predicted the secondary separation region with use of the Wilcox-Durbin model. However, the RANS simulation of the 3D double fin failed to accurately predict the surface heat transfer using the linear and weakly non-linear Wilcox-based models. This is common for RANS simulations of SBLI flows, as also shown by simulations conducted by Knight and Degrez [30]. Other overviews of SBLI simulations involving DNS, LES, and LES/RANS methods can be found in works by

Zheltovodov [31] and Edwards [32], the latter of which touches briefly on experiments exploring the effects of heat transfer on SBLI's by Zheltovodov et al. [33, 34].

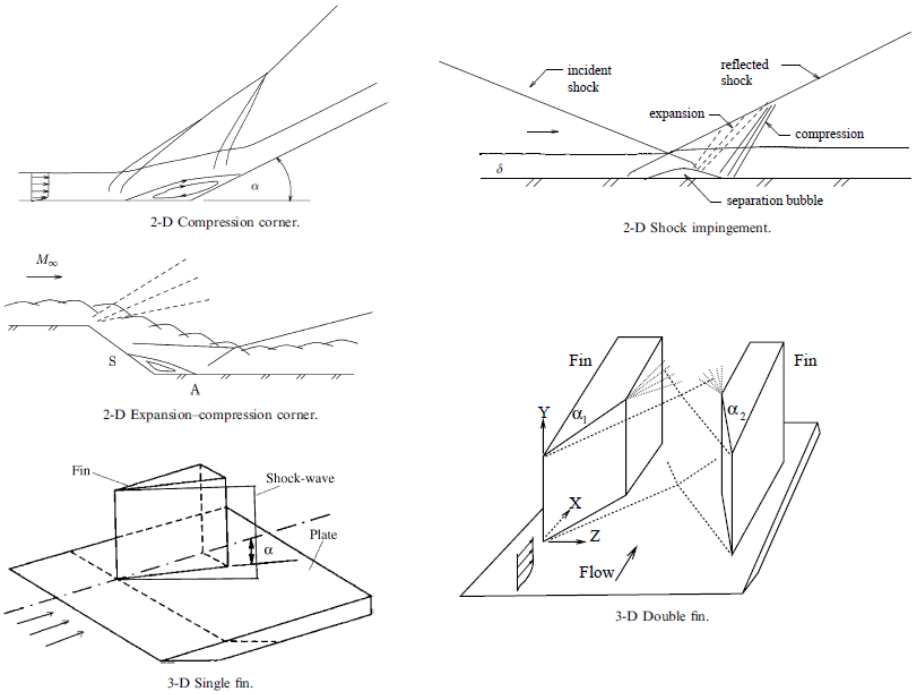

Figure 10: Configurations run with DNS, LES, and RANS (used with permission from Knight et al. [8]).

Wu et al. [9, 35, 36, 37, 10, 38, 39] have performed a series of DNS simulations on a 24 degree compression ramp with experimental data provided by Bookey et al. [40]. Originally they showed that the DNS simulations under predicted the separation region within the SBLI interaction, as shown in Fig. 11. Numerical code bugs as well as the incoming conditions to the corner were eliminated as factors of the discrepancy due to the agreement between the DNS simulation and the experimental data upstream of the compression corner. In turn, they determined that numerical modeling of SBLI's is sensitive to the numerical dissipation and suggested the use of a limiter on the dissipation schemes. Rerunning the DNS simulations with the limiter showed great improvements in predicting the size of the separation region, shown in Fig. 12.

Continuing with the compression corner theme, Edwards et al. [11] used LES/RANS to explore a 28 degree compression corner flow interaction. Menter's Shear Stress Transport (SST) [41] turbulence model was used for the RANS portion. Although the simulations captured the shock behavior well, it was noted that there was a great dependence on the shear stress transport limiter within the SST turbulence model, shown in Fig. 13. Further analyses of the SST and other k-omega based turbulence models as related to SBLI's have been performed by Georgiadis and Yoder [42] as well as Tan and Jin [43]. One draw back to LES/RANS method used was the need to calibrate the blending function constant per case. This was

eliminated by Giesking et al. [44, 45] by using an estimate of the outer-layer length scale based on the resolved turbulent kinetic energy, ensemble-averaged modeled turbulence kinetic energy, and ensemble-averaged and time-resolved turbulence frequencies. This estimated length scale, in conjunction with the inner-layer length scale, was then used to determine to blending function model constant.

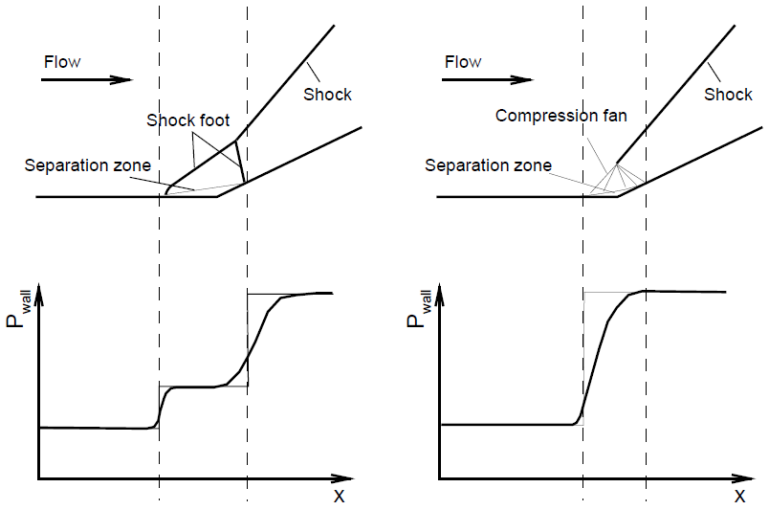

Figure 11: Flow pattern sketches for the experiment (left) and DNS (right) for a 24 degree compression corner (from Wu et al. [9]).

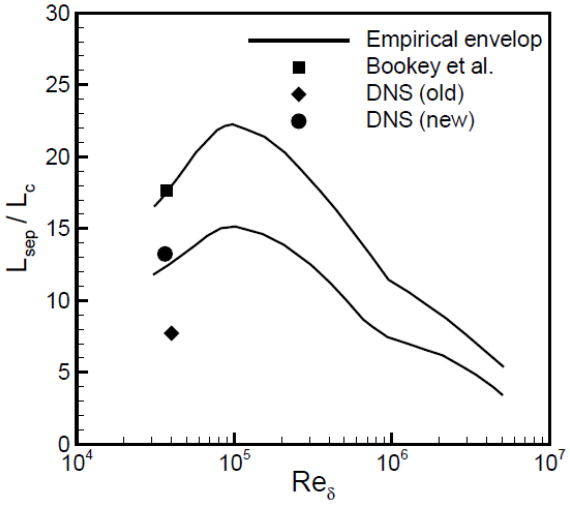

Figure 12: Comparison of the size of the separation bubble with (new) and without (old) a dissipation limiter (from Wu and Martin [10]).

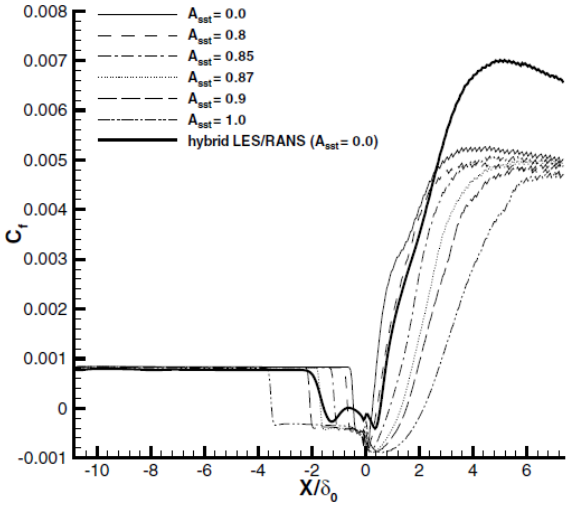

Figure 13: Skin friction distribution (RANS models) for a 28 degree compression corner at Mach 5 (used with permission from Edwards et al. [11]).

2 Geometry and Numerical Modeling

2.1 Geometry and Mesh

The UM Glass Tunnel [12] is a suck down tunnel shown in Figs. 14 and 15 with the oblique shock generating wedge shown in Fig. 16. Although the upstream converging-diverging nozzle is interchangeable, only runs with the Mach 2.75 nozzle are explored in this thesis. The wedge is centered about the center-span of the tunnel and the tunnel sits in a room controlled to a temperature of 295.7 K $\pm$1 K [46]. At the freestream velocity of the tunnel, the static temperature is about 118 K. The top and bottom walls are made of aluminum while the side walls and bottom window are composed of glass. The test section was designed to be 2.25" x 2.75" with a throat cross-section of 2.25" x 0.742". However, the current "as installed" dimensions deviated from this with a test section and throat cross-section of 2.25" x 2.72" and 2.25" x 0.725", respectively [46]. These measurements were taken well after the experimental data had been collected for the workshop and the tunnel has been taken apart and reassembled since then. As such, it only offers an approximation of what the dimensions might have been for those runs.

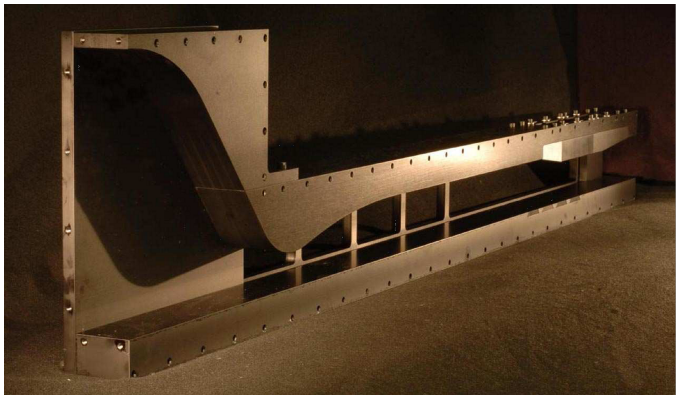

Figure 14: Cut-away view of the University of Michigan Glass Tunnel (from Lapsa [12]).

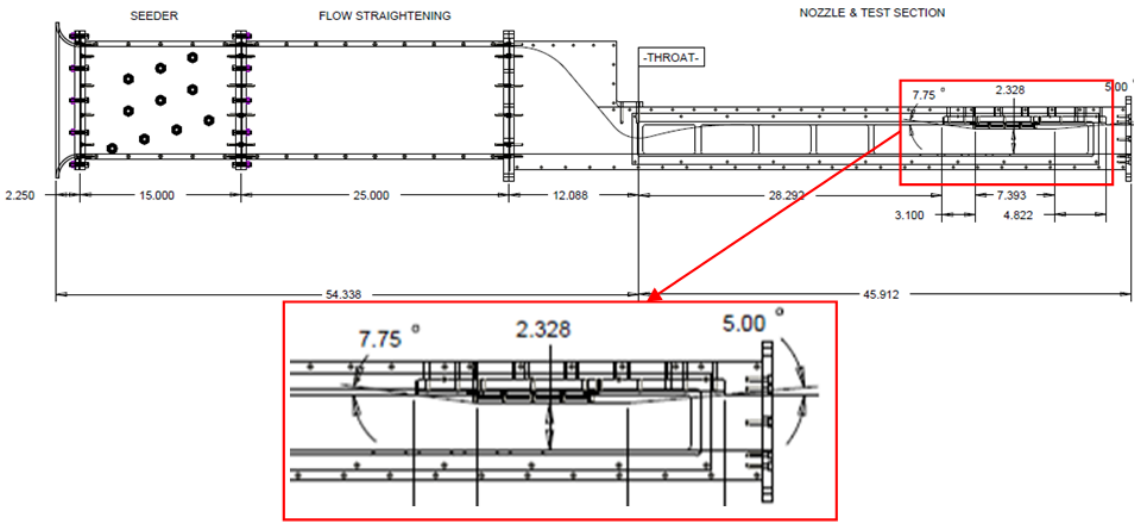

Figure 15: Schematic of the University of Michigan Glass Tunnel with upstream flow straightener and seeder (from Lapsa [12]). Note units are in inches.

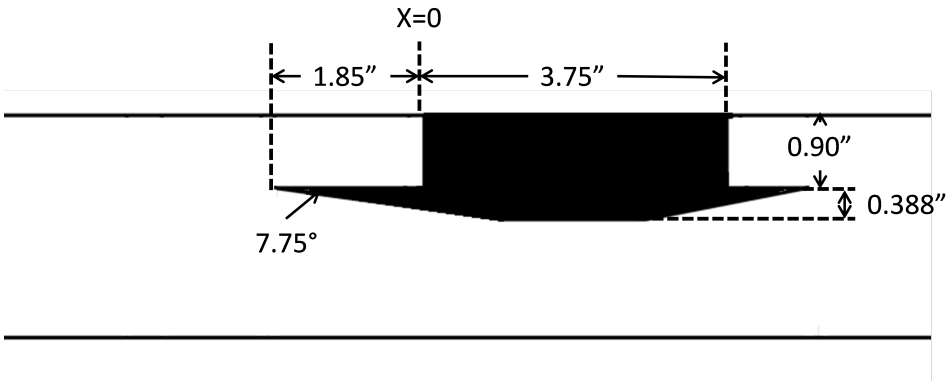

Figure 16: 7.75 degree wedge geometry. Dimensions courtesy of Lapsa [12].

The tunnel, along with the wedge, was modeled by a modified version of a 3D over-set grid by Marshall Galbraith. The original grid, containing 53 million grid points divided into 15 zones, paid particular attention to the packing along the walls and around the oblique shock location. However, it was felt that the throat region could benefit from a more dense axial clustering. Thus an additional 50 axial points were inserted to define the throat contour, shown in Fig. 17. The final grid of 56 million grid points is shown in Fig. 18. Like the original grid, the final grid was packed very tightly to the wall such that $y^+ = 0.25$ at the first point off the wall, based on fully expanded tunnel conditions at Mach 2.75.

The grid coordinate system uses a left-handed coordinate system non-dimensionalized by the tunnel height of 2.75 in. However, the coordinate system used for data comparison is consistent with the one used in the workshop, which was dimensionalized in mm with the origin at the strut leading edge, bottom wall,

and center-span. To convert from the grid coordinate system to the data comparison coordinate system:

$$x = 25.4\,(2.75x_{grid} - 38.265) \tag{1}$$

$$y = (25.4 \times 2.75)\,z_{grid} \tag{2}$$

$$z = 25.4\,(2.75y_{grid} - 1.125) \tag{3}$$

Note that the grid coordinate system has the z-coordinate and y-coordinate flipped relative to the data coordinate system. It should also be noted that the data coordinate system is slightly different than the one used by Lapsa [12], in which the axial origin was at the inviscid shock impingement location. Both are different than the coordinate system used by Eagle et al. [46] for the planned second SBLI Workshop, which is a left-handed coordinate system with the origin located at the wedge leading edge, bottom wall, right wall (looking downstream).

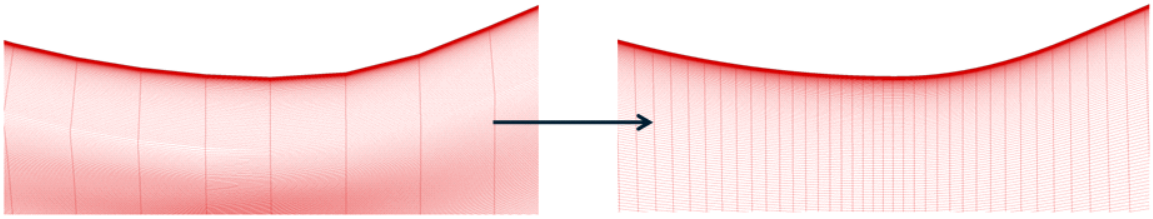

Figure 17: Grid throat region packing with original (left) and final (right).

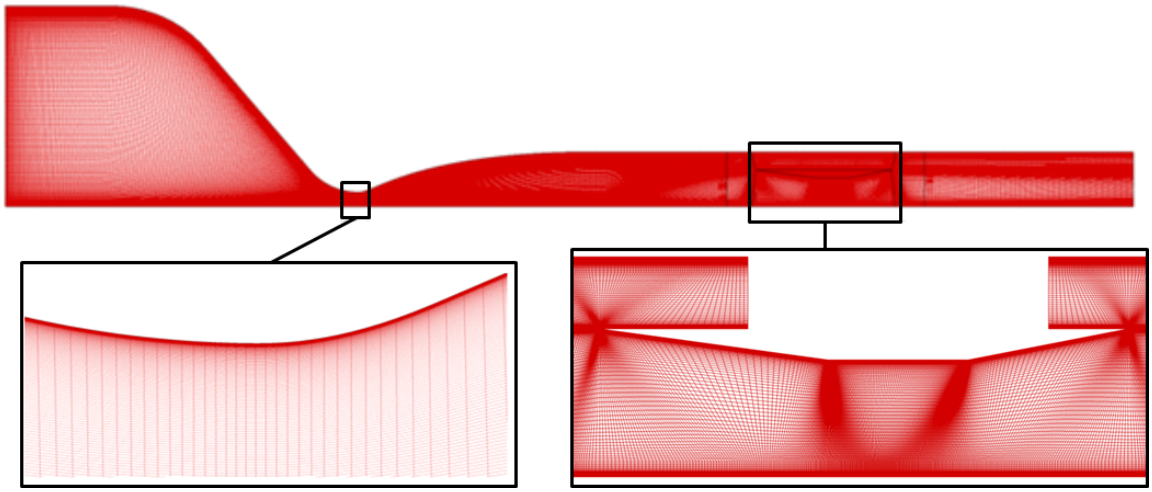

Figure 18: Side view of the grid representing the tunnel and 7.75 degree wedge with center-span wedge and throat inserts shown.

2.2 Solver

OVERFLOW [47, 48], a RANS flow solver for structured over-set grids, was chosen as the CFD solver for the SBLI analyses. Version 2.2e was used on a cluster of 20 Quad-Core Xeon X5570 processors (NASA Pleiades-Nehalem). Runtime for each analysis took approximately three days on the 80 processors. For solving the Navier-Stokes equations, spatial integration used the HLLC scheme [49] with the Koren limiter [50] to third-order accuracy while temporal integration used SSOR [51] to first-order accuracy. All analyses utilized the SST turbulence model with all zones considered turbulent, unless otherwise specified.

OVERFLOW requires a set of reference conditions to non-dimensionalize the input parameters and set the freestream conditions. Because OVERFLOW uses the freestream conditions to initialize the flow field when not given an initial solution, Mach 2.75 conditions were chosen for the reference state with total quantities equaling the room statics due to the vacuum driven nature of the tunnel. Using 1D perfect gas equations yields the following reference values:

$$T_t = 295.7\,\mathrm{K} \tag{4}$$

$$p_t = 98\,\mathrm{kPa} \tag{5}$$

$$M_{ref} = 2.75 \tag{6}$$

$$L_{ref} = 0.06985\,\mathrm{m}\,(2.75\,\mathrm{in}) \tag{7}$$

$$\gamma = 1.4 \tag{8}$$

$$R = 287\,\mathrm{J/\,(kg\,\centerdot\,K)} \tag{9}$$

$$T_\infty = T_t \left(1 + \frac{\gamma - 1}{2} M_{ref}^2\right)^{-1} = 117.69\,\mathrm{K} \tag{10}$$

$$p_\infty = p_t \left(1 + \frac{\gamma - 1}{2} M_{ref}^2\right)^{-\frac{\gamma}{\gamma - 1}} = 3.898\,\mathrm{kPa} \tag{11}$$

$$a_\infty = \sqrt{\gamma R T_\infty} = 217.46\,\mathrm{m/s} \tag{12}$$

$$V_\infty = M_{ref} a_\infty = 598.01\,\mathrm{m/s} \tag{13}$$

$$\rho_\infty = \frac{p_\infty}{R T_\infty} = 0.1154\,\mathrm{kg/m^3} \tag{14}$$

$$\mu_\infty = 1.716\mathrm{x}10^{-5} \left(\frac{T_\infty}{491.6}\right)^{1.5} \left(\frac{491.6 + 198.6}{T_\infty + 198.6}\right) = 8.163 \times 10^{-6}\,\mathrm{kg/(m \cdot s)} \tag{15}$$

$$Re_L = \frac{\rho_\infty V_\infty L_{ref}}{\mu_\infty} = 592,876 \tag{16}$$

Note the test section height was chosen as the reference length due to the grid being non-dimensionalized by this parameter and μ_∞ was calculated using Sutherland's Law. Specifics on the direct OVERFLOW input variables and redimensionlizing scheme are outlined in reference [3].

3 Case Overviews

3.1 CFD Cases with OVERFLOW

To explore the key physics mentioned earlier, seven cases were run as outlined in Table 1. A baseline case (denoted as Standard) was first run with various parameters set to reflect prior CFD analyzes. To explore heat transfer boundary conditions, a case was run such that the top and bottom walls (along with the wedge) were isothermal while all other surfaces (including the bottom window) remained adiabatic. The window was approximated from 45 mm to 140 mm axially and -16.575 mm to 14.425 mm spanwise [46]. The isothermal surfaces were set to the room temperature of 295.7 K. Although the actual temperature of the aluminum varies due to heat transfer, assuming it is isothermal at the room temperature is likely to be better than considering it to be adiabatic.

To explore geometry sensitivities, a case was run with the grid modified to reflect the as-installed geometry with greatest measured tolerances accounted for. The grid was modified by raising the bottom wall to achieve the desired test-section height and redefining the nozzle curve to obtain the desired throat height. The nozzle curve modification was achieved by dividing the contour into two sections and scaling accordingly. The upstream section was defined from the trailing edge of the inlet straight section to the geometric throat while the downstream section was defined from the geometric throat to the leading edge of the tunnel straight section. The new upstream contour section was then defined as:

$$y_{new} = (y_{throat,new} - y_{throat,old}) \left(\frac{x_1 - x}{x_1 - x_{throat}} \right)^m + y_{old} \tag{17}$$

where

$$m = 0.5 + 1.5 \left(\frac{x_{throat} - x}{x_{throat} - x_1} \right) \tag{18}$$

Note the subscript 1 denotes the inlet trailing edge match point. Likewise, the downstream contour section was defined as:

$$y_{new} = (y_{throat,new} - y_{throat,old}) \left(\frac{x_2 - x}{x_2 - x_{throat}} \right)^m + y_{old} \tag{19}$$

where

$$m = 1 + 2 \left(\frac{x_{throat} - x}{x_{throat} - x_2} \right) \tag{20}$$

Note the subscript 2 denotes the tunnel straight section leading edge match point. A sample modified nozzle

contour with an exaggerated throat area based on this scheme is shown in Fig. 19.

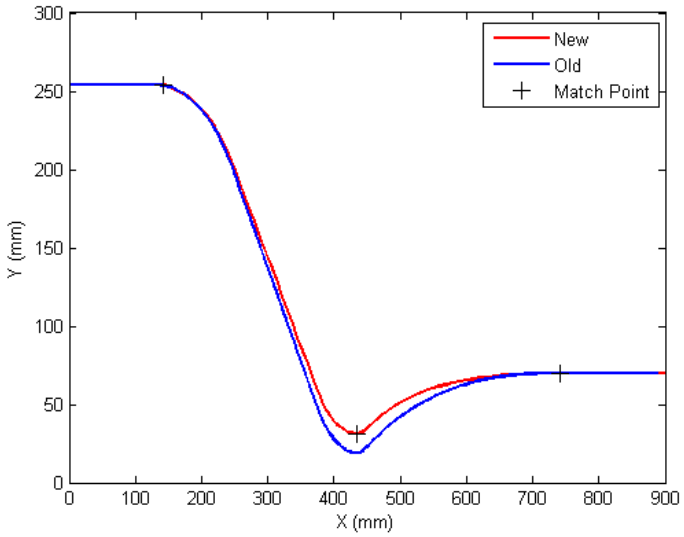

Figure 19: Sample modified nozzle contour. Note the difference between the old and new throat heights is exaggerated compared to what was actually used.

To explore laminar verses turbulent flow, two cases were run. A base case was run with laminar flow from the nozzle plenum inlet to the leading edge of the wedge in order to establish a "trip" location for the second case. In OVERFLOW, the effect of a boundary-layer trip was simulated by forcing upstream zones to be laminar. OVERFLOW handles laminar zones by zeroing out the production terms of the turbulence model in use [47]. At the desired trip location, or transition point, the production terms within the turbulence model are activated for all zones downstream of this point. As a result, eddy viscosity is calculated, and added to the laminar viscosity in the transport equations. Figure 20 shows the momentum thickness Reynolds number contour for the bottom wall (half-span) while Fig. 21 shows the corresponding values at the bottom wall center-span. The trip location was defined where the momentum thickness Reynolds number approximately equaled 400. This value is suggested by Abu-Ghannam and Shaw (AGS) [52] as the start of transition for turbulence intensities of 1.5%; however several values of momentum thickness Reynolds number could have been chosen to define the trip location. Using a momentum thickness Reynolds number of 400 yields a trip location at an axial location of -470 mm. Thus the second case (denoted as Trip) had laminar flow defined from the nozzle inlet up to that trip point. OVERFLOW uses a grid line to set transition, so the gridline located at the trip point on the bottom wall was used as the trip location for all four walls. From Fig. 21, it can be seen that the momentum thickness Reynolds number is approximately 260 at the nozzle throat. The turbulence intensity must be greater than 2.3 for this flow transition to occur upstream of the throat based on the flat zero pressure gradient AGS [52]. Considering this and the favorable pressure gradient situation

of the accelerating nozzle flow, which in turn tends to delay transition, it is likely that the flow transitions downstream of the throat.

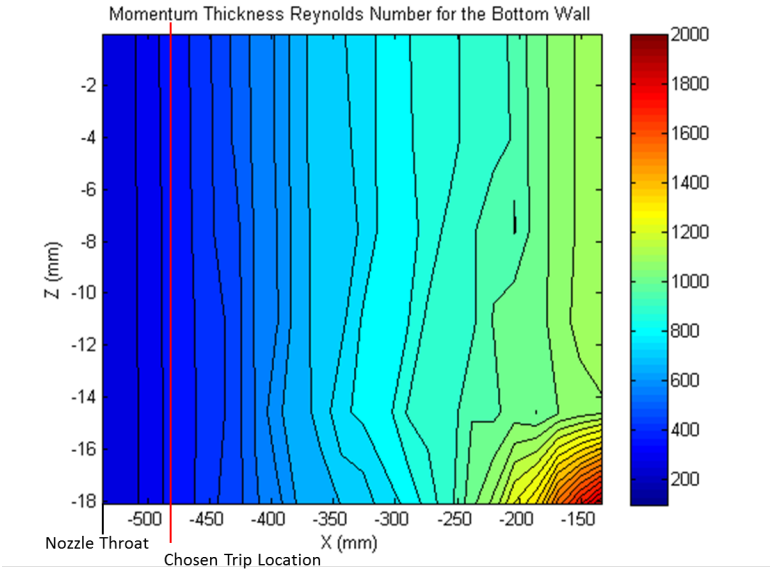

Figure 20: Momentum thickness Reynolds number at the bottom wall (half-span) for the laminar case.

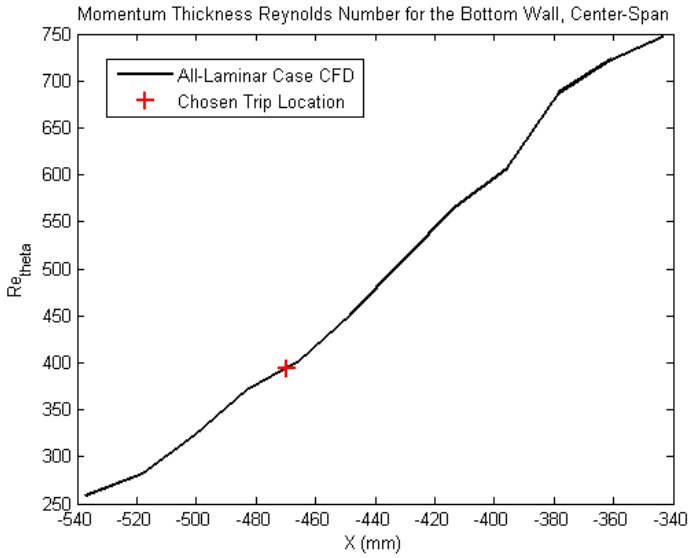

Figure 21: Momentum thickness Reynolds number at the bottom wall, center-span.

A case was also run that combined the attributes of the isothermal, as-installed geometry, and trip cases to demonstrate the combined effects each parameter has on the flow field. In addition, a sweep of cases was run to explore sensitivities to turbulence quantities and turbulence modeling. Two of these cases explored sensitivities to the freestream turbulent kinetic energy and freestream turbulent viscosity by running the

Standard case with higher values of each. The Standard and Combined cases were also run with an array of varying turbulence models, of which a turbulence model case study was performed prior to running the SBLI configuration and discussed later in this thesis. It should be noted that one sensitivity already accounted for in the above cases is the sensitivity to total temperature. The total temperature used for the workshop CFD cases was 293 K, a value that was not experimentally measured at the time. Using 1D perfect gas equations yields a velocity increase of 2.8 m/s (or 0.47% of a 600 m/s freestream velocity) for the 2.7 K increase in total temperature. Further, the ±1 K in the total temperature measurement would yield an additional fluctuation of ±1 m/s (or 0.17% of a 600 m/s freestream velocity). These are all relatively small numbers, however, additively they may have an important combined effect.

Table 1: Summary of CFD Cases.

Case	A/A*	Turbulence Model	Heat Transfer Boundary Conditions	Freestream Turbulent Kinetic Energy (m^2/s^2)	Normalized Freestream Turbulent Viscosity
Standard	3.7062	SST	All surfaces adiabatic	$3.576x10^{-1}$	0.3
Isothermal	3.7062	SST	Top/bottom walls and wedge isothermal at T=295.7 K. All other surfaces (including bottom window) adiabatic.	$3.576x10^{-1}$	0.3
Modified Geometry	3.7847	SST	All surfaces adiabatic	$3.576x10^{-1}$	0.3
Trip	3.7062	Laminar from nozzle inlet up till trip, SST downstream of trip. Trip location at x=-470 mm	All surfaces adiabatic	$3.576x10^{-1}$	0.3
Combined	3.7847	Laminar from nozzle inlet up till trip, SST downstream of trip. Trip location at x=-470 mm	Top/bottom walls and wedge isothermal at T=295.7 K. All other surfaces (including bottom window) adiabatic.	$3.576x10^{-1}$	0.3
TKE	3.7062	SST	All surfaces adiabatic	$3.576x10^{3}$	0.3
MUT	3.7062	SST	All surfaces adiabatic	$3.576x10^{3}$	3.0

3.2 PIV Exploration

To better compare the CFD with the experimental data, the CFD solutions from the Standard and Combined cases were re-post-processed to explore particle lag that is associated with the PIV techniques used to acquire the experimental data. To account for the particle lag, a crude model adjusted the coordinates of each CFD data point using the following equations:

$$\tilde{x} = x + u_x \tau \tag{21}$$

$$\tilde{y} = y + v_y \tau \tag{22}$$

Three time constants, τ, were chosen to represent a 50%, 75%, and 100% total velocity reduction shown in Fig. 22. This yields time constants of 1.8 (short), 3.7 (medium), and 5.5 (long) µs, respectively. Because the model was only applied to the center-span and the spanwise velocity is nearly zero, only the axial and transverse directions were accounted for in the particle lag calculation. Note that this model only attempts to mimic the effect of particle lag and that it is not based on the actual physics under consideration. To complement the particle lag model, a window averaging scheme was initially explored using a similar method used by Garman, Visbal, and Orkwis [53, 54] to average out the values within the center spanwise plane. However, the PIV grids proved to be nearly as fine as the CFD grids for the method to be effective with the prescribed window of 0.24 x 0.24 mm [46]. Window averaging was also attempted by averaging three spanwise planes, which included the centerspan and ±0.75 mm to cover the 1.5 mm spanwise differance [12]. This was shown to have little effect; the results of which are not shown in this thesis.

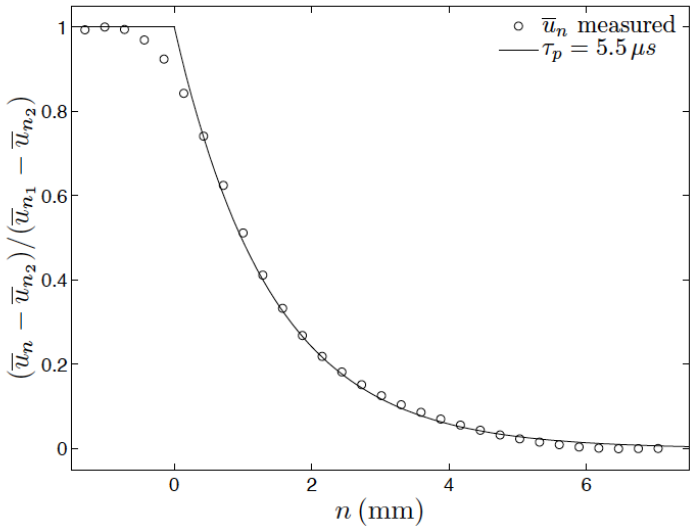

Figure 22: Measured particle response through an oblique shock (from Lapsa [12]). The velocity component normal to the shock, u_n, is normalized by the pre-shock (u_{n1}) and post-shock (u_{n2}) velocities and shown as a function of the shock-normal direction, n. An exponential fit to the data reveals the particle relaxation time, $\tau p = 5.5$ µs.

4 Flat Plate

4.1 Overview

Before exploring turbulence model sensitivities with the complex SBLI cases, a fundamental study was performed to gauge the effectiveness of various turbulence models available. The 2D Zero Pressure Gradient Flat Plate Verification Case provided by the Turbulence Model Benchmarking Working Group [13] was chosen for this study. Boundary conditions along with the finest grid are shown in Fig. 23. The flow across the plate is at Mach 0.2 with a Reynolds number of 5 million per foot and a reference temperature of 540 °R. The plate itself is modeled as an adiabatic solid wall. Because OVERFLOW can only handle 3D grids, the 210,000 point 2D grid was converted into a 3D grid by duplicating the grid in three depthwise planes, for a total of 630,000 grid points. The 2D boundary condition was then applied within OVERFLOW to handle the extra dimension. Four turbulence models were explored: SST, Menter's baseline model (BSL) [41], Wilcox's 1988 k-omega model [55], and a modified version of the SST model by Georgiadis and Yoder (SST-GY) [42]. All of these models are variations of the k-omega model with one of the biggest differences being the limitation on the turbulent shear stress. The limit is defined as a percentage of the turbulent kinetic energy, with 31% for SST, 35.5% for SST-GY, and no limit for BSL and k-omega. For this study, BSL and SST-GY models were coded manually by modifying the existing SST model within OVERFLOW.

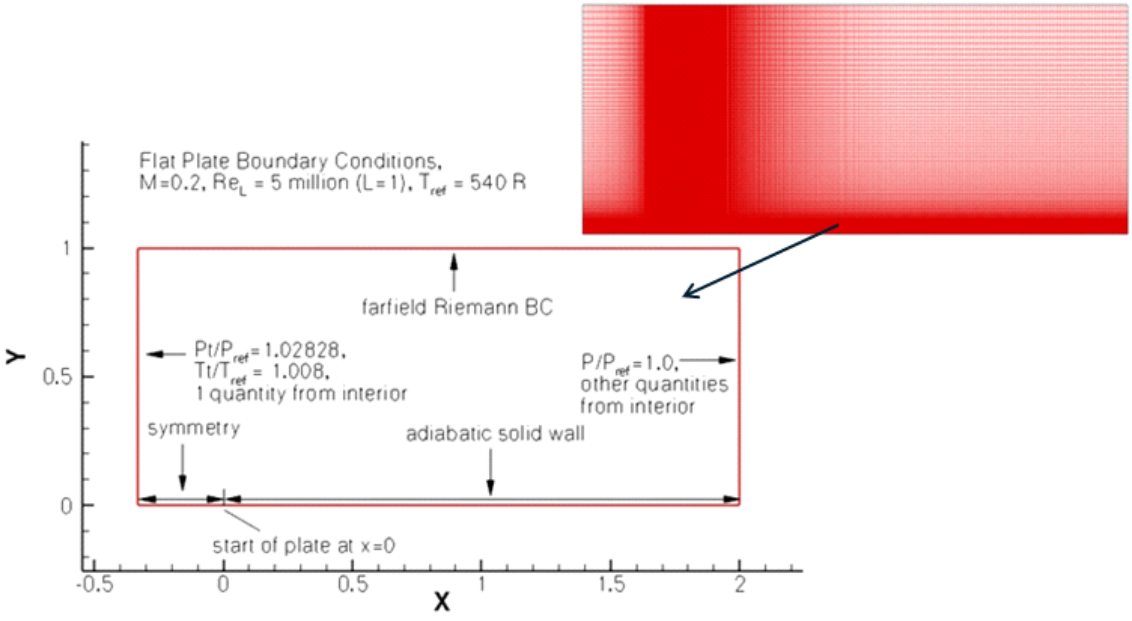

Figure 23: Flat plate 2D grid and boundary conditions [13].

4.2 Results

A benchmark test with the SST turbulence model was first performed and compared to outputs from CFL3D and FUN3D, courtesy of reference [13]. The skin friction coefficient profile for the SST turbulence model for all three flow solvers is shown in Fig. 24. It can be seen that the OVERFLOW solution agrees well with the other codes. With this confidence, the other turbulence models were run and compared to the SST solution, shown in Fig. 24. Experimental data was from Wieghardt and Tillman [56]. It can be seen that the BSL and SST-GY models predict a slightly higher skin friction coefficient compared to SST (within 2%) while the k-omega model predicts a larger skin friction coefficient compared to SST (within 6%). All models, with the exception of k-omega, agree well with the experimental data.

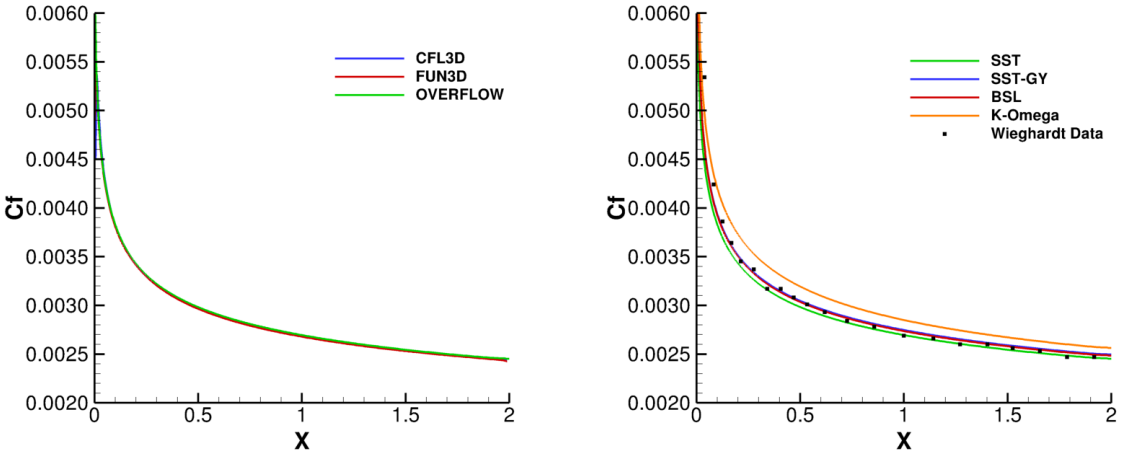

(a) SST turbulence model.

(b) OVERFLOW results.

Figure 24: Skin friction coefficient profiles.

To further examine the differences, Fig. 25 shows u^+ verses y^+ at a Reynolds number of 4.2 million ($x = 0.84$ ft). It can be seen that all the models agree well with the experimental data and Spalding's formula [57], although the k-omega model under-predicts u^+ in the outer boundary layer. This is consistent with the over-prediction of the skin fiction coefficient because the upper bound on u^+ is inversely proportional to the square root of the skin friction coefficient. Note, the following form of Spalding's formula was used [58]:

$$y^+ = u^+ + e^{-5.033\kappa}\left(e^{\kappa u^+} - 1 - \kappa u^+ - \frac{1}{2}\left(\kappa u^+\right)^2 - \frac{1}{6}\left(\kappa u^+\right)^3\right) \tag{23}$$

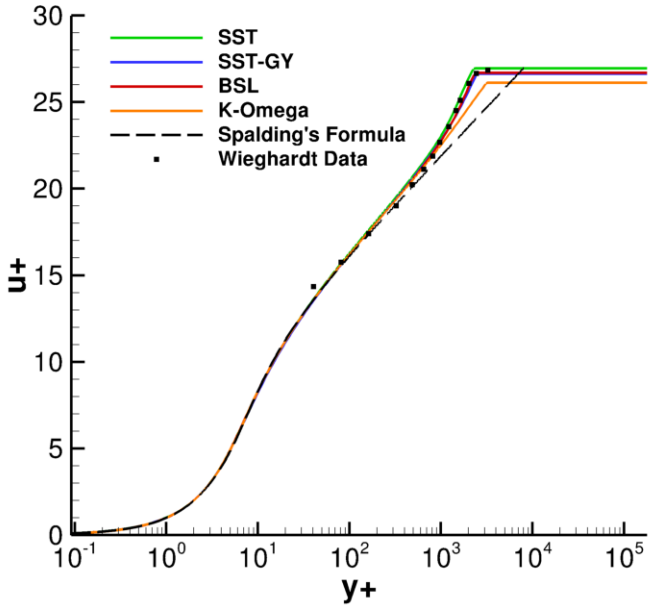

Figure 25: u^+ verses y^+ for the various turbulence models at $Re_x = 4.2E6$.

The stark prediction differences between the k-omega model compared to SST, SST-GY, and BSL are more clearly shown in Fig. 26, which includes profiles of the normalized turbulent shear stress and turbulent viscosity at the same Reynolds number of 4.2 million. Experimental data in this case was from Klebanoff [59]. With the exception of the k-omega model, the CFD solutions agree reasonably well with the experimental data. Because of the non-conformity of the k-omega model to the other models tested, an additional study varying the freestream turbulent viscosity was performed. The freestream turbulent viscosity was singled out because it has been widely known that the 1988 version of the k-omega model is extremely dependent on it for a given turbulent kinetic energy state [60]. In fact, one of the motivations behind Mentor's BSL and SST models was to eliminate the freestream turbulent viscosity dependence [41]. The normalized shear stress and turbulent viscosity profiles are shown in Fig. 27 from this additional study. Note that the value of $(\mu_T/\mu)_{Inf}$ used for all prior analyses was 0.3. It can be seen that the k-omega solutions approach the SST solution with decreasing freestream turbulent viscosity. However, it most likely would take an unrealisticly low freestream turbulent viscosity value for the k-omega model to be within the ballpark of the SST solution at a more realistic value. Thus it is not recommended that the 1988 k-omega model be used for the SBLI analyses.

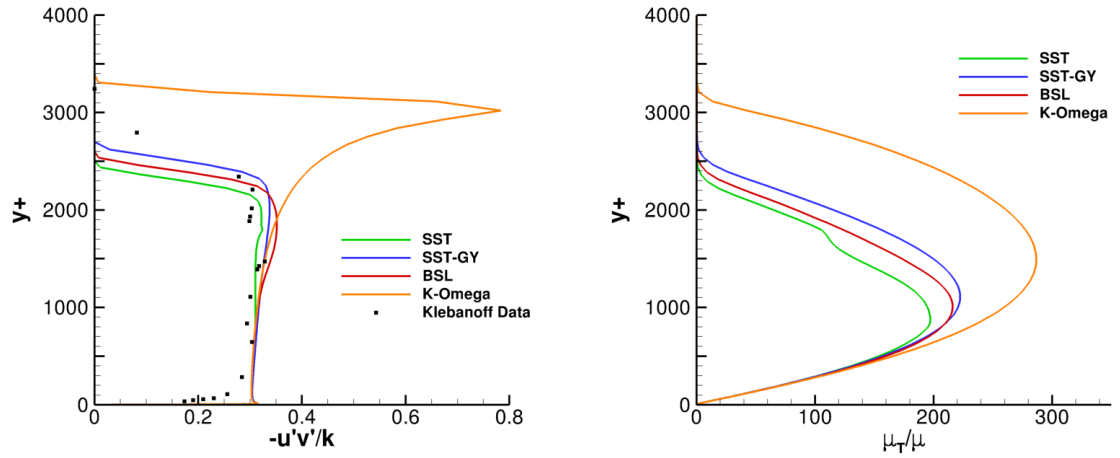

(a) Normalized turbulent shear stress.

(b) Normalized turbulent viscosity.

Figure 26: Normalized turbulent parameters for various turbulence models at $Re_x = 4.2E6$

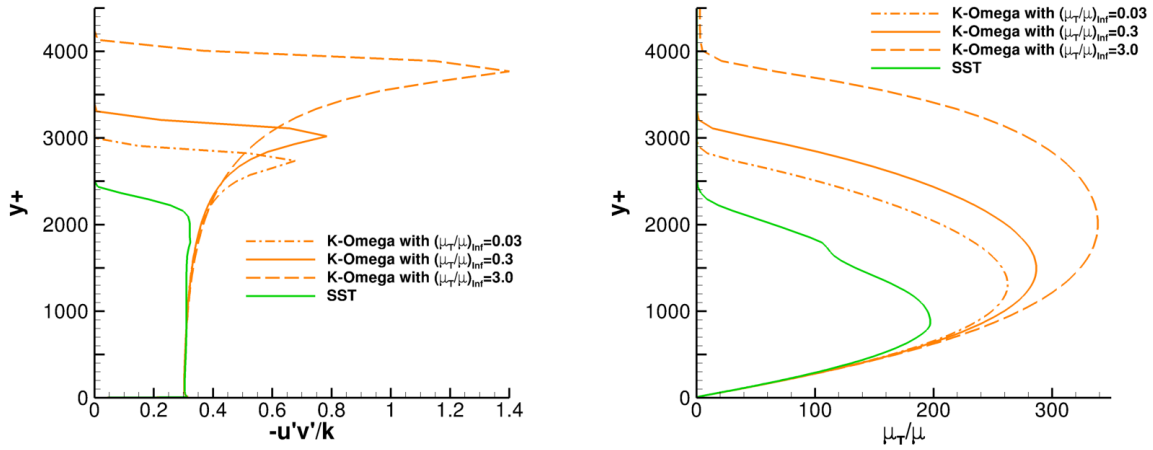

(a) Normalized turbulent shear stress.

(b) Normalized turbulent viscosity.

Figure 27: Normalized turbulent parameters at various freestream turbulent viscosities at $Re_x = 4.2E6$

5 Quasi-1D Code

5.1 Overview

For the cases presented, the static temperature of the air in the test section is quite cold at nearly 118 K due in part to the high Mach number. Such cold temperatures put the perfect gas assumption in question. In particular, the assumption that the specific heat at constant pressure is constant and that the ideal gas law holds true. This sensitivity could not be explored by using the production version of OVERFLOW as the code cannot handle varying specific heats. Thus, a quasi-1D MATLAB [61] code was developed to compute various thermodynamic and flow parameters for calorically perfect and non-ideal air. The latter half required the use of the National Institute of Standards and Technology (NIST) Reference Fluid Thermodynamic and Transport Properties Database (REFPROP) code [62]. The MATLAB code has the capability to calculate the properties at a single station and over an oblique shock for either a given u velocity or $A/A*$ ratio. Total conditions must also be provided for the code to run. Station nomenclature in the code uses 1 for upstream of the oblique shock and 2 for downstream of the oblique shock. The code is currently set up for air and utilizes a predefined mixture [63, 64] containing, by mass fraction, 75.57% nitrogen, 23.16% oxygen, and 1.2691% argon when interfacing with REFPROP. The code, however, can be modified for a variety of gases, such as carbon dioxide. Regardless if the gas is perfect or non-ideal, the code assumes the total enthalpy is conserved and that the normal v velocity is constant across the oblique shock, as shown in Figs. 28 and 29. The code also assumes single phase states.

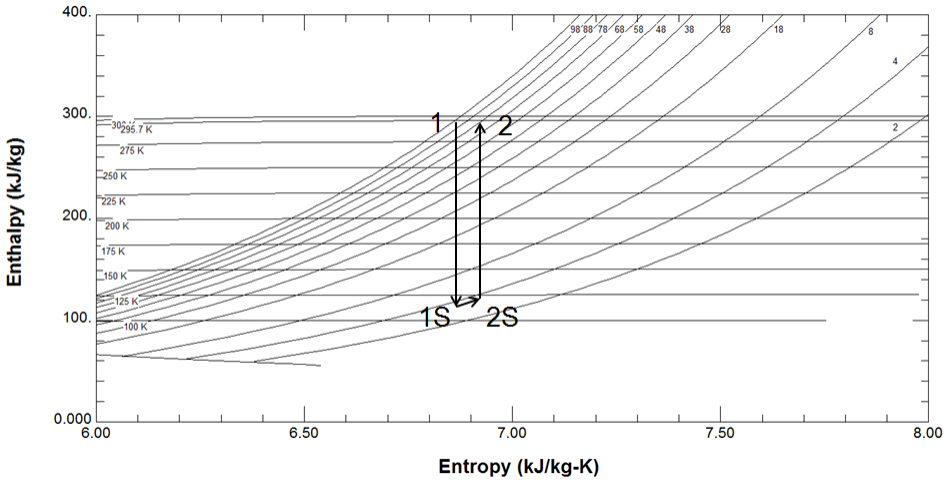

Figure 28: Sample enthalpy verses entropy diagram for calculating across an oblique shock for a non-ideal gas. 1: total conditions at Station 1, 1S: static conditions at Station 1, 2S: static conditions at Station 2, 2: total conditions at Station 2.

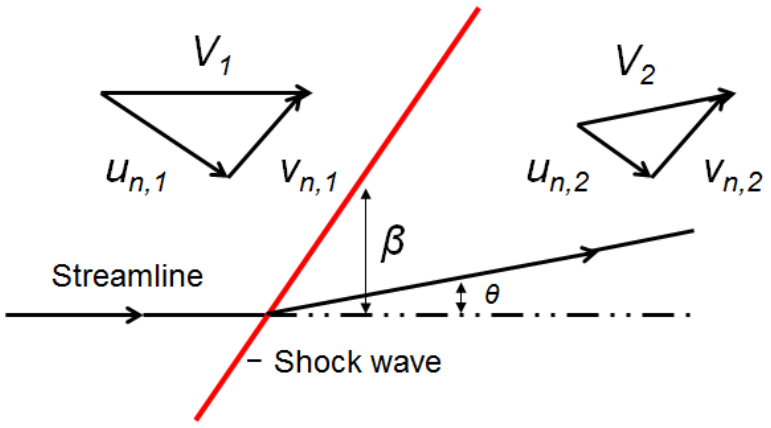

Figure 29: Oblique shock notation.

5.2 Calorically Perfect Code

The calorically perfect side of the code (runType options 0 and 10) utilizes the perfect gas equations along with the ideal gas law [65]. Station 1 conditions are calculated as follows:

$$\gamma = 1.4 \tag{24}$$

$$c_{p,1} = \frac{\gamma R}{\gamma - 1} \tag{25}$$

$$h_{t,1} = c_{p,1} T_{t,1} \tag{26}$$

$$h_1 = h_{t,1} - \frac{u_1^2}{2} \tag{27}$$

$$T_1 = \frac{h_1}{c_{p,1}} \tag{28}$$

$$M_1 = \frac{u_1}{\sqrt{\gamma R T_1}} \tag{29}$$

$$p_1 = p_{t,1} \left(1 + \frac{\gamma - 1}{2} M_1^2 \right)^{-\frac{\gamma}{\gamma - 1}} \tag{30}$$

$$\rho_1 = \frac{p_1}{RT_1} \tag{31}$$

To calculate the shock angle and respective Mach number and velocity components ahead of the oblique shock [66]:

$$0 = \tan^3\beta + C_1 \tan\beta + C_2 \tan\beta + C_3 \tag{32}$$

where

$$C_1 = C_3\left(1 - M_1^2\right) \tag{33}$$

$$C_2 = \frac{\frac{\gamma+1}{\gamma-1}M_1^2 + \frac{2}{\gamma-1}}{M_1^2 + \frac{2}{\gamma-1}} \tag{34}$$

$$C_3 = \frac{\frac{2}{\gamma-1}}{\tan\theta\left(M_1^2 + \frac{2}{\gamma-1}\right)} \tag{35}$$

and

$$u_{n,1} = u_1 \sin\beta \tag{36}$$

$$M_{n,1} = M_1 \sin\beta \tag{37}$$

To calculate Station 2 conditions, mass, momentum, and energy equations were balanced across the oblique shock.

$$\rho_1 u_{n,1} = \rho_2 u_{n,2} \tag{38}$$

$$p_1 + \rho_1 u_{n,1}^2 = p_2 + \rho_2 u_{n,2}^2 \tag{39}$$

$$\frac{1}{2}u_{n,1}^2 + h_1 = \frac{1}{2}u_{n,2}^2 + h_2 \tag{40}$$

$$p_2 = \rho_2 R T_2 \tag{41}$$

$$c_{p,2} = c_{p,1} \tag{42}$$

$$h_2 = c_{p,2} T_2 \tag{43}$$

Equations (38) through (43) were solved numerically using a bisection scheme. Once converged, the remaining Station 2 conditions could be calculated.

$$u_2 = \frac{u_{n,2}}{\sin(\beta - \theta)} \tag{44}$$

$$M_2 = \frac{u_2}{\sqrt{\gamma R T_2}} \tag{45}$$

$$M_{n,2} = \frac{u_{n,2}}{\sqrt{\gamma R T_2}} \tag{46}$$

$$T_{t,2} = T_{t,1} \tag{47}$$

$$h_{t,2} = h_{t,1} \tag{48}$$

$$p_{t,2} = p_2 \left(1 + \frac{\gamma - 1}{2} M_2^2\right)^{\frac{\gamma}{\gamma - 1}} \tag{49}$$

Once station conditions were found, sonic properties could be calculated for either station.

$$\frac{A}{A*} = \left(\frac{2}{\gamma + 1}\right)^{\frac{\gamma+1}{2(\gamma-1)}} M^{-1} \left(1 + \frac{\gamma - 1}{2} M^2\right)^{\frac{\gamma+1}{2(\gamma-1)}} \tag{50}$$

$$T* = T_t \left(1 + \frac{\gamma - 1}{2}\right)^{-1} \tag{51}$$

$$h* = c_p T* \tag{52}$$

$$p* = p_t \left(1 + \frac{\gamma - 1}{2}\right)^{-\frac{\gamma}{\gamma - 1}} \tag{53}$$

$$u* = \sqrt{\gamma R T*} \tag{54}$$

$$M* = \frac{u}{u*} \tag{55}$$

5.3 Non-Ideal Code

The non-ideal side of the code (runType options 2 and 12) utilizes REFPROP for most of the calculations and does not take into consideration the ideal gas law. Station 1 conditions are found as follows:

$$h_{t,1} = f\left(T_{t,1}, p_{t,1}\right) \tag{56}$$

$$s_{t,1} = f\left(T_{t,1}, p_{t,1}\right) \tag{57}$$

$$h_1 = h_t - \frac{u_1^2}{2} \tag{58}$$

$$T_1 = f\left(h_1, s_{t,1}\right) \tag{59}$$

$$p_1 = f\left(h_1, s_{t,1}\right) \tag{60}$$

$$\rho_1 = f\left(h_1, s_{t,1}\right) \tag{61}$$

$$a_1 = f\left(h_1, s_{t,1}\right) \tag{62}$$

$$M_1 = \frac{u_1}{a_1} \tag{63}$$

$$\gamma_1 = f\left(h_1, s_{t,1}\right) \tag{64}$$

$$c_{p,1} = f\left(h_1, s_{t,1}\right) \tag{65}$$

To calculate the shock angle and respective Mach number and velocity components ahead of the oblique shock:

$$\frac{\tan\left(\beta - \theta\right)}{\tan\beta} = \frac{u_{n,2}}{u_{n,1}} \tag{66}$$

$$u_{n,1} = u_1 \sin\beta \tag{67}$$

$$M_{n,1} = M_1 \sin\beta \tag{68}$$

Equations (66) through (68) were solved numerically using a bisection scheme as an outer-loop to Equations (69) through (72), which numerically balance the mass, momentum, and energy equations across the oblique shock.

$$\rho_1 u_{n,1} = \rho_2 u_{n,2} \tag{69}$$

$$p_1 + \rho_1 u_{n,1}^2 = p_2 + \rho_2 u_{n,2}^2 \tag{70}$$

$$\frac{1}{2}u_{n,1}^2 + h_1 = \frac{1}{2}u_{n,2}^2 + h_2 \tag{71}$$

$$\rho_2 = f\left(h_2, p_2\right) \tag{72}$$

Once Equations (66) through (72) were converged, the remaining Station 2 conditions could be calculated.

$$s_2 = f\left(h_2, p_2\right) \tag{73}$$

$$T_2 = f\left(p_2, s_2\right) \tag{74}$$

$$a_2 = f\left(p_2, s_2\right) \tag{75}$$

$$\gamma_2 = f\left(p_2, s_2\right) \tag{76}$$

$$c_{p,2} = f\left(p_2, s_2\right) \tag{77}$$

$$u_2 = \frac{u_{n,2}}{\sin\left(\beta - \theta\right)} \tag{78}$$

$$M_2 = \frac{u_2}{a_2} \tag{79}$$

$$M_{n,2} = \frac{u_{n,2}}{a_2} \tag{80}$$

$$h_{t,2} = h_{t,1} \tag{81}$$

$$T_{t,2} = f\left(h_{t,2}, s_2\right) \tag{82}$$

$$p_{t,2} = f\left(h_{t,2}, s_2\right) \tag{83}$$

Once station conditions were found, sonic properties could be calculated for either station. Sonic conditions were found by first numerically solving for the sonic enthalpy and velocity.

$$h* = h_t - \frac{u*^2}{2} \tag{84}$$

$$u* = f\left(h*, s\right) \tag{85}$$

Once converged, rest of the sonic properties could be calculated.

$$p* = f\left(h*, s\right) \tag{86}$$

$$T* = f\left(h*, s\right) \tag{87}$$

$$M* = \frac{u}{u*} \tag{88}$$

$$\gamma* = f\left(h*, s\right) \tag{89}$$

$$\frac{A}{A*} = \frac{p*}{p}\frac{T}{T*}\frac{1}{M*} \tag{90}$$

5.4 Quasi-1D Exploration

Several parameters of interest were calculated for a range of Mach numbers, spanning Mach 1.4 to 3.5. The percentage difference between these parameters for the calorically perfect and non-ideal air are shown in Fig. 30. The percentage difference is defined as:

$$\%Diff = 100\text{x}\frac{NonIdeal - Perfect}{Perfect} \tag{91}$$

Also, the perfect dynamic viscosity values were obtained using the following form of Sutherland's law [67]:

$$\mu = 1.458\text{x}10^{-6}\frac{T^{1.5}}{T + 110.4} \tag{92}$$

It can be seen that there is not a drastic difference between the solutions, with at most a 0.4% difference between non-ideal and perfect air at Mach 2.75. The only exception to this would be the Prandtl number, which is upwards of 9% difference. For this study the perfect air Prandtl number was assumed to be a constant value of 0.702, which is associated with air at standard atmospheric conditions. It is known that the Prandtl number varies with temperature and therefore most of the difference between the non-ideal and perfect Prandtl numbers is due to temperature variance and not from assuming perfect or non-ideal air. Also explored was the effect of the shock angle for varying wedge angles, shown in Fig. 31. It can be seen that there is not much of a difference between the non-ideal and perfect shock angles with a difference of about 0.2% at Mach 2.75, regardless of the wedge angle. The noise within Fig. 31 is most likely due to the convergence tolerance when solving Equations (66) through (72). Based on these 1D studies it can be concluded that although there is some effect from assuming the air is perfect, it is a good enough assumption, especially given the extra computational power needed to compute non-ideal air in 3D simulations.

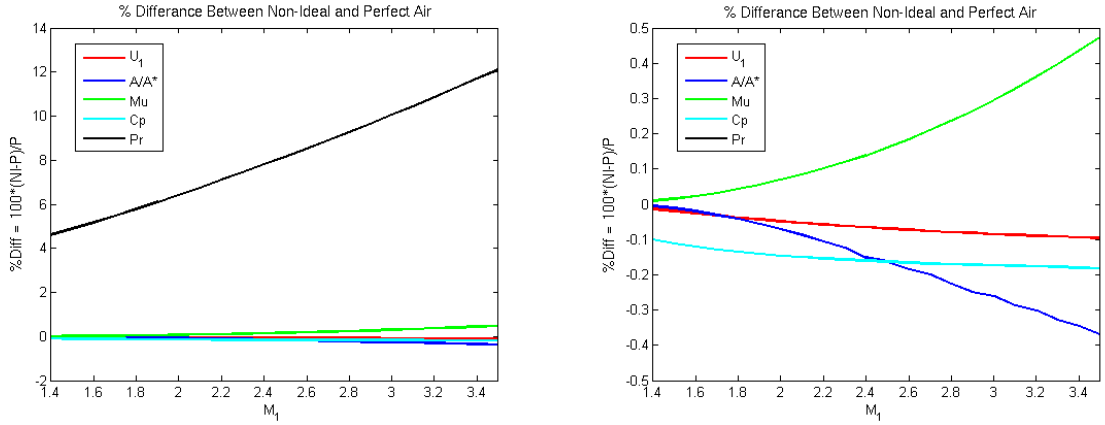

(a) Full range.

(b) Zoomed in to $\pm$ 0.5%.

Figure 30: Percentage differences between non-ideal and perfect air for various parameters.

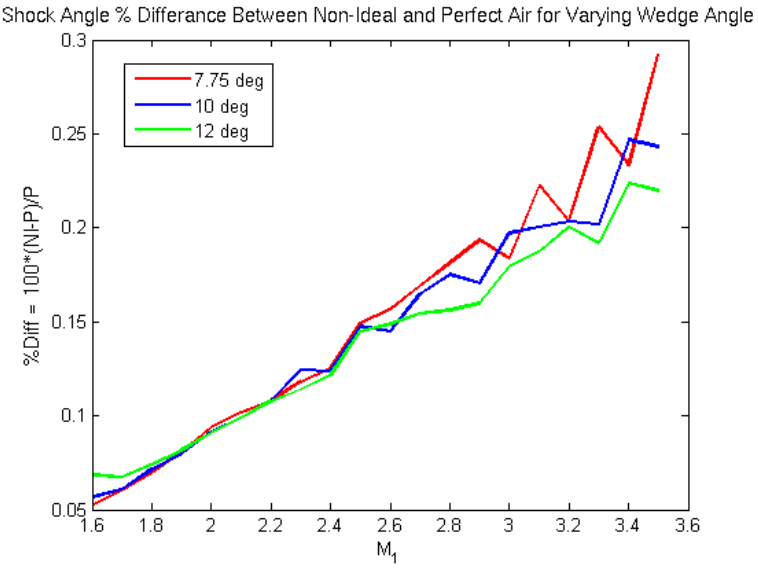

Figure 31: Percentage differences of the shock angle between non-ideal and perfect air for varying wedge angles.

6 Grid Resolution Study

A grid resolution study was performed on the standard SBLI grid with the Standard Case conditions. The study looked at solutions obtained on the coarse, medium, and fine grid levels in a similar manor as Galbraith [3], with streamwise cross-sections of the grids shown in Fig. 32. Due to OVERFLOW interpolating final solutions onto the finest mesh, regardless of grid level, solutions were read into Tecplot [67, 68] by reading every fourth point for the coarsest grid level and every other point for the medium grid level. Convergence of the solutions was based on the L2 residual, shown in Fig. 33. In addition, the fine grid level solution was run out an additional 1000 iterations and showed that the u and v velocity profiles of interest changed by no more than 0.1 m/s. Thus, all solutions presented are considered iteratively converged.

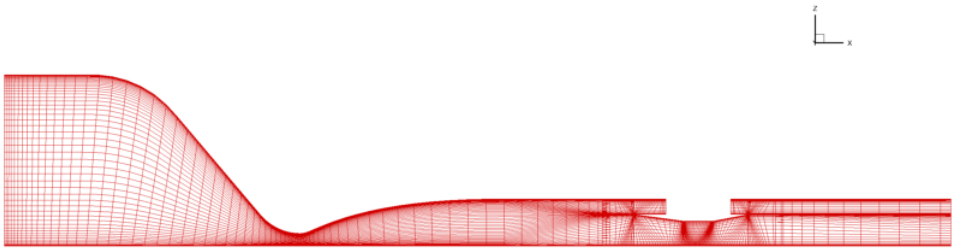

(a) Coarse grid.

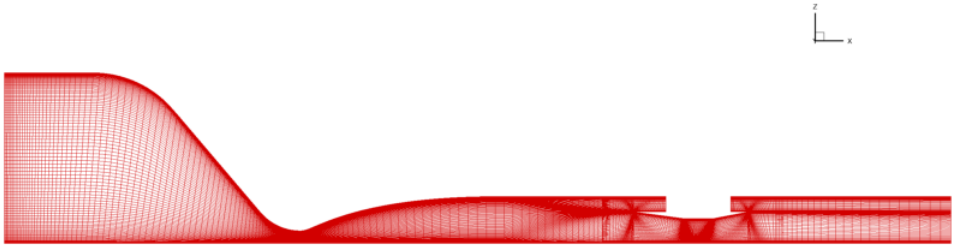

(b) Medium grid.

(c) Fine grid.

Figure 32: Streamwise cross-sections at center-span for the various grid levels.

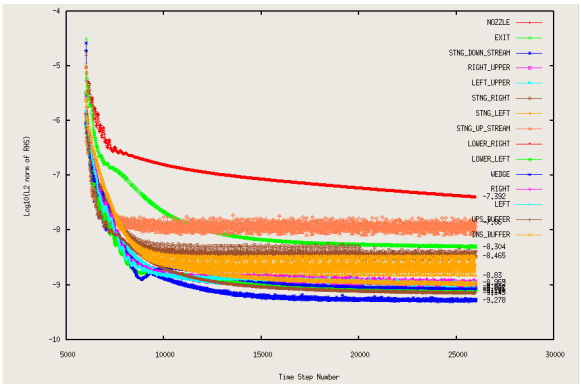

(a) Coarse grid level.

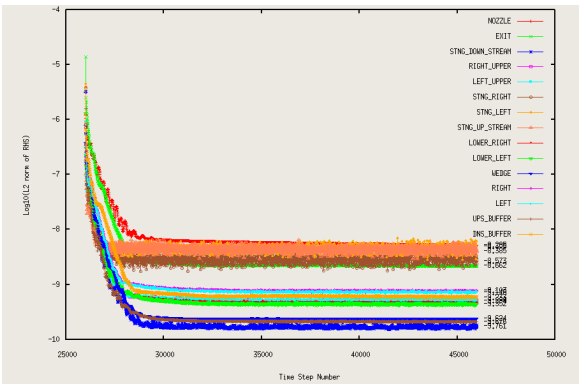

(b) Medium grid level.

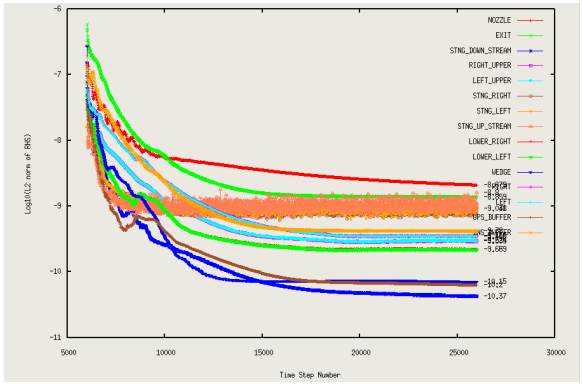

(c) Fine grid level.

Figure 33: L2 residuals for the Standard case.

Several parameters were looked at to determine grid convergence. First, total pressure, total temperature, and Mach number were computed at three different locations, shown in Table 2. Location coordinates can be found in Table 4. It can be seen that the totals ahead of the oblique shock are converging to the input totals of 98,000 Pa and 295.7 K and that the Mach numbers at the throat and upstream of the oblique shock are converging to their 1D expected values of 1.00 and 2.75, respectively. Also, it can be seen that the total pressure and Mach number downstream of the oblique shock are correctly converging to lower values than their upstream counterparts while the total temperature is mostly conserved.

Second, mass flow rates at the inlet, exit, and throat regions were computed and shown in Table 3. Mass flow rates were computed using the mass flow integration routine within Tecplot [67]. Like the total quantities and Mach number, the mass flow rates are converged well with less than 0.5% loss throughout the tunnel (with 86% of this total mass loss upstream of the throat) on the finest grid level. The mass loss is primarily due to round-off error within the discretization process. Finally, u velocity profiles of interest within the streamwise plane located underneath the wedge were examined, as shown in Fig. 34. It can be seen that while the u velocity profiles are very close for the medium and fine grid levels, they themselves are

not fully grid converged. Because the profiles are crucial for the results presented in this thesis, it is fair to say that this parameter is the dominating one out of the parameters presented. Thus while the results are shown to be still converging, the fine grid level is considered most suitable for the studies presented here.

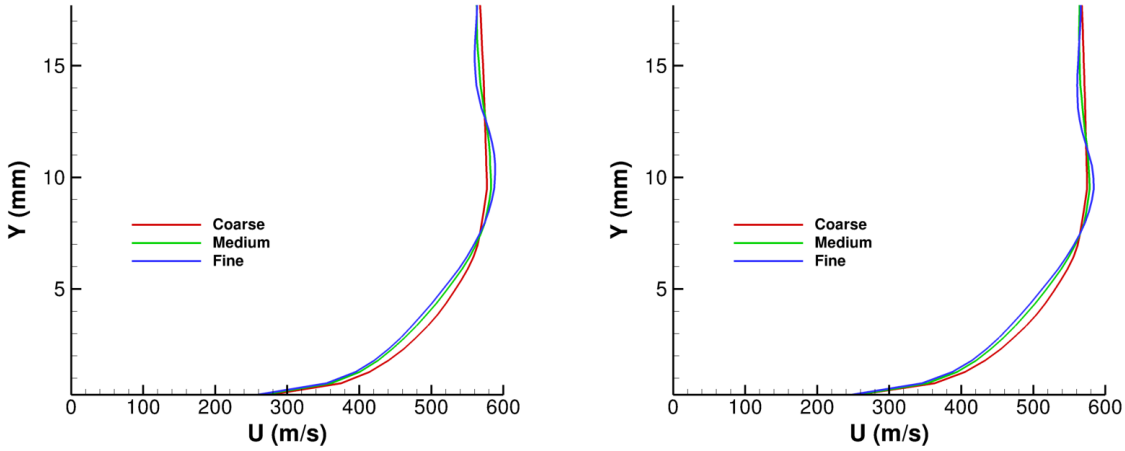

(a) At $x = 18.191$ mm. (b) At $x = 20.76$ mm.

Figure 34: u velocity profiles within the streamwise plane.

Table 2: Various flow parameters used to determine grid convergence.

		Coarse	Medium	Fine
Throat	$p_t\,(Pa)$	98761.8	98199.4	98009.4
	$T_t\,(K)$	296.530	295.909	295.701
	$Mach$	0.952165	0.947367	0.947031
Upstream	$p_t\,(Pa)$	98134.4	98103.0	97996.9
	$T_t\,(K)$	296.504	295.960	295.704
	$Mach$	2.73365	2.73637	2.74482
Downstream	$p_t\,(Pa)$	96083.7	96459.3	96247.1
	$T_t\,(K)$	296.173	296.073	295.742
	$Mach$	2.49111	2.48308	2.47317

Table 3: Mass flow rates (kg/s) used to determine grid convergence.

	Coarse	Medium	Fine
Inlet	0.250120	0.247012	0.245282
Throat	0.246334	0.245170	0.244326
Exit	0.247058	0.245823	0.244169

Table 4: Coordinates for grid resolution study.

	X (mm)	Y (mm)	Z (mm)
Throat	-538.6808	8.7612	-2.1299
Upstream	-188.1651	36.4712	-2.1299
Downstream	34.7961	21.8123	-0.6699
Inlet	-971.9310	All	All
Throat	-538.6808	All	All
Exit	403.6530	All	All

7 Results

7.1 Standard Case

The streamwise data plane from the SBLI experiment was used as the primary plane to compare experimental and CFD data as it is considered to be the most accurate of all the experimental data planes [19]. The location of the plane is shown in Fig. 35, which is located at center-span. Velocity contours for the Standard case along with the experimental data are shown in Fig. 36. For consistency with the prior workshop, velocities were normalized by $U_{Inf} = 603$ m/s. Although the contours appear similar, the CFD solution under predicts the velocities (particularly u). In addition, the reflected oblique shock in the CFD solution is upstream of the experimental data. To further inspect the flow field, Fig. 37 shows contours of negative u velocities just above the bottom wall underneath the wedge. These contours provide a convenient way to approximate the bottom wall separation region underneath the wedge. The resulting blockage, derived from the corner flows, is typical of prior CFD analysis and has been shown by Galbraith et. al. [23] to play a major role in the flow field for this tunnel due to the tunnel's small size. The blockage at the throat is also important and can be quantified by introducing a throat blockage parameter, $b*$, which is defined by the following equations [23]:

$$\dot{m}* = (1 - b*)\,\dot{m}*_{ideal} \tag{93}$$

where

$$\dot{m}*_{ideal} = A * \frac{p_t}{\sqrt{T_t}} \sqrt{\frac{\gamma}{R}\left(\frac{2}{\gamma+1}\right)^{\frac{\gamma+1}{\gamma-1}}} \tag{94}$$

The blockage parameter calculation assumes adiabatic, ideal perfect gas, and choked flow and is shown to be 1.53% for the Standard Case.

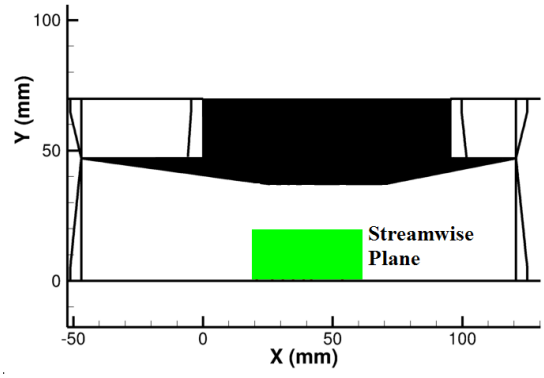

Figure 35: Data plane location in reference to the grid.

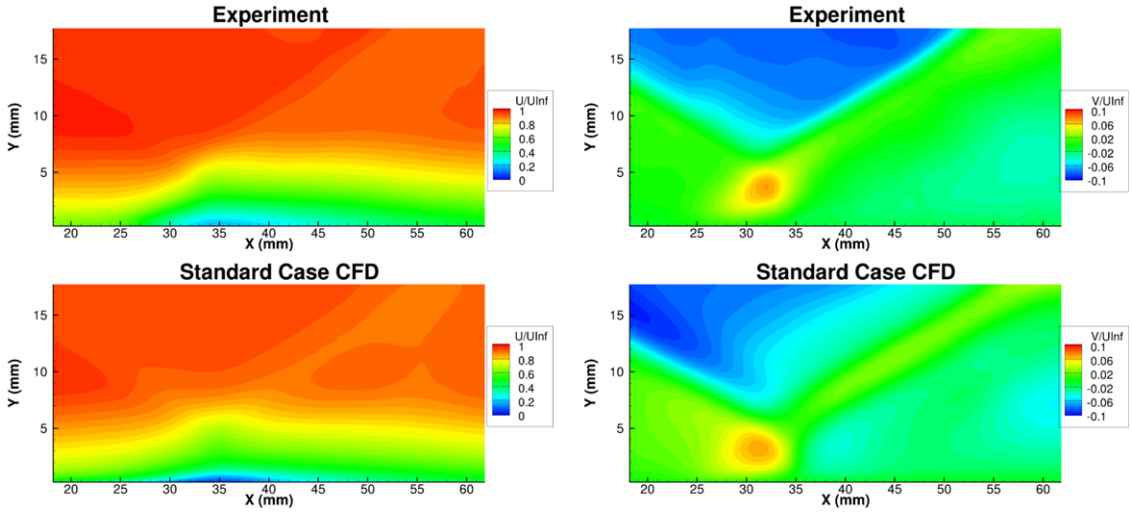

Figure 36: u velocity (left) and v velocity (right) streamwise contours for the experiment (top) and Standard case (bottom).

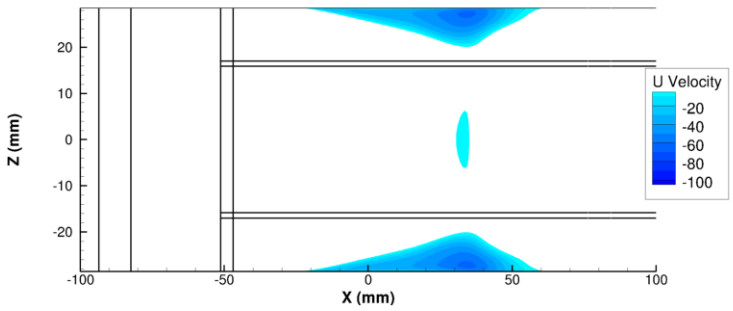

Figure 37: Bottom wall separation underneath the wedge for the Standard case.

7.2 Particle Lag Effects

Velocity contours with the particle lag incorporated are shown in Fig. 38, with the remaining velocity contour plots located in appendix A. Note only the Standard and Combined cases are shown as they are representative of the spectrum of presented cases. Figures 39 through 42 show u and v velocity profiles with and without particle lag at the most upstream axial location along with the first intersecting spanwise data plane. See appendix B for remaining axial stations within the streamwise plane. The lag is shown to bring both the Standard and Combined cases closer to the experimental data with increasing lag time constant. Because the lag has such an effect, it is not advisable to use the workshop metric for comparing CFD to this PIV obtained experimental data without accounting for the lag. Recall that it is a fraction of the entire experimentally derived time constant that is used for the lag model. Although it is a very short time, it creates an error in the velocity field that is higher than the desired match between the CFD and experiment.

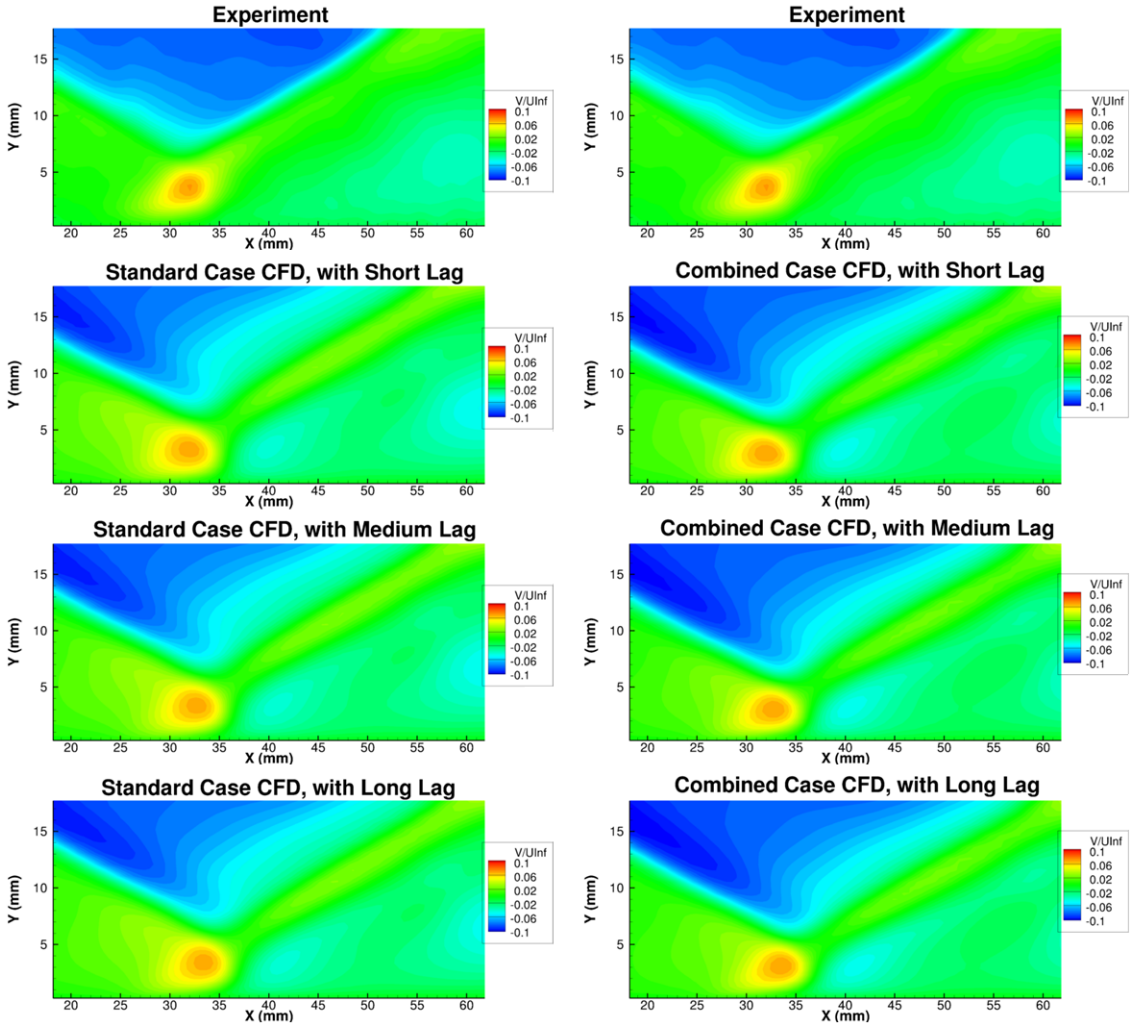

Figure 38: v velocity streamwise contours for the experiment (top), short lag (middle-top), medium lag (middle-bottom), and long lag (bottom).

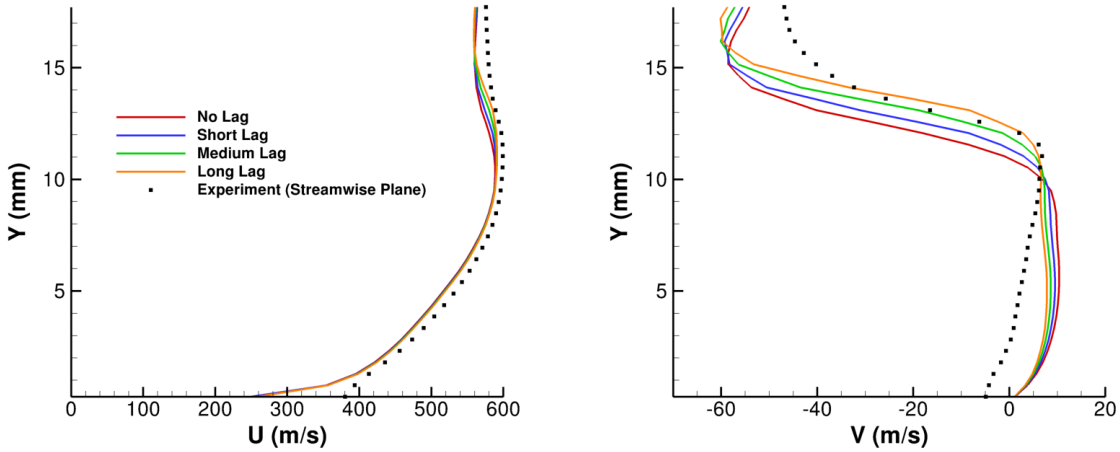

(a) u velocity profiles. (b) v velocity profiles.

Figure 39: Select velocity profiles at the most-upstream axial location ($x = 18.191$ mm) for the Standard case.

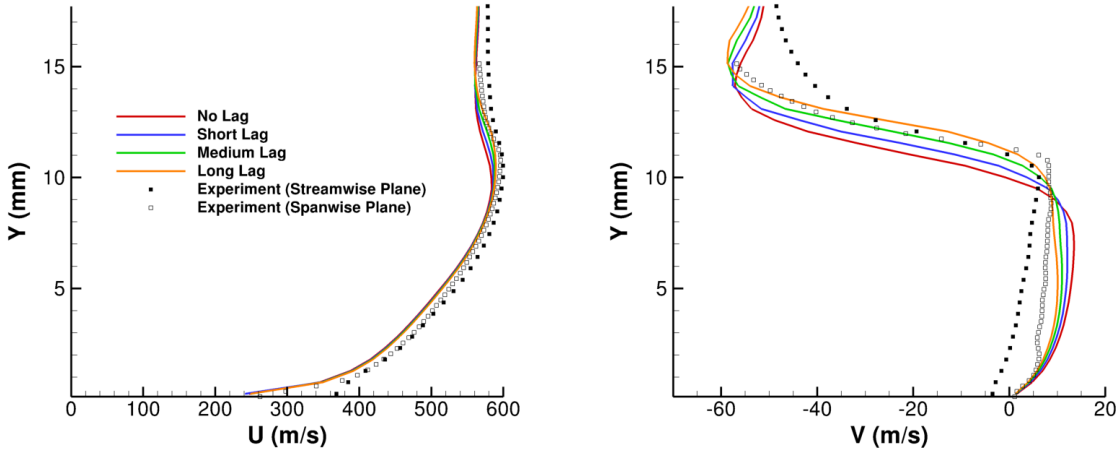

(a) u velocity profiles (b) v velocity profiles

Figure 40: Select velocity profiles at the first intersecting spanwise plane ($x = 20.76$ mm) for the Standard case.

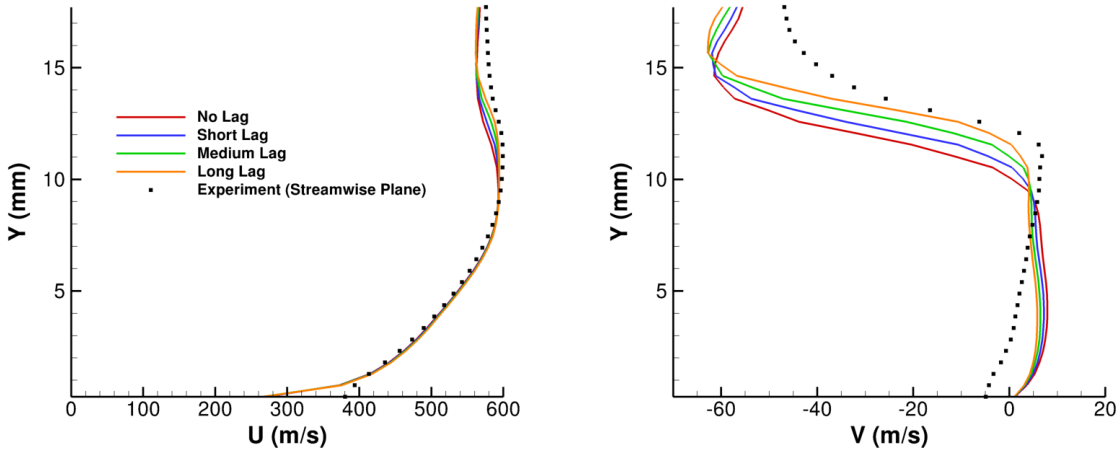

(a) u velocity profiles.

(b) v velocity profiles.

Figure 41: Select velocity profiles at the most-upstream axial location ($x = 18.191$ mm) for the Combined case.

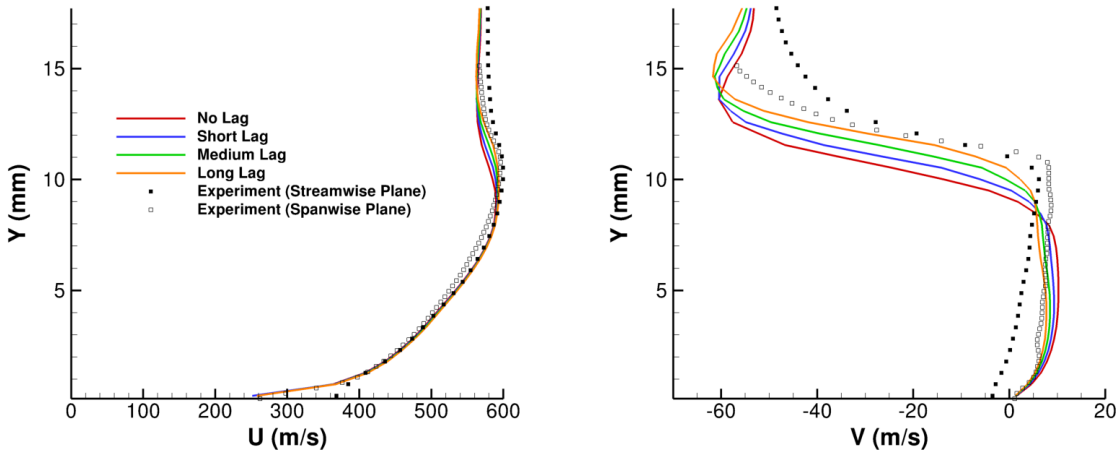

(a) u velocity profiles.

(b) v velocity profiles.

Figure 42: Select velocity profiles at the first intersecting spanwise plane ($x = 20.76$ mm) for the Combined case.

7.3 Isothermal Case

The effects of the Isothermal case can be seen in Figs. 43 and 44. Figure 43 and the static temperature profile in Fig. 44 show little difference in the thermal boundary layer between the Standard and Isothermal cases. However, assuming the aluminum is isothermal is more realistic as there is likely heat transfer between the aluminum and the tunnel's surroundings. The temperature difference is evident in the total temperature

center-span profile at the bottom wall, shown in Fig. 45. For reference, several notable stations have been marked to orient the profile. Figure 45 also confirms that the isothermal boundary conditions were implemented correctly and that the deviation from the constant total temperature for the Isothermal and Combined cases is due to the presence of the adiabatically modeled bottom window. Further, the isothermal boundary conditions were shown to have an effect on the total temperature profile, as shown in Fig. 44. The thermal recovery factor, r_c, is determined to be 92.3% from the following equation:

$$\frac{T_{aw}}{T_\infty} = 1 + \frac{r_c}{2}(\gamma - 1) M_\infty^2 \tag{95}$$

where T_{aw} is the adiabatic wall temperature, or the total temperature evaluated from an adiabatic calculation. This value of r_c is reasonable for turbulent flows as the recovery factor is approximately equal to the cube root of the Prandtl number.

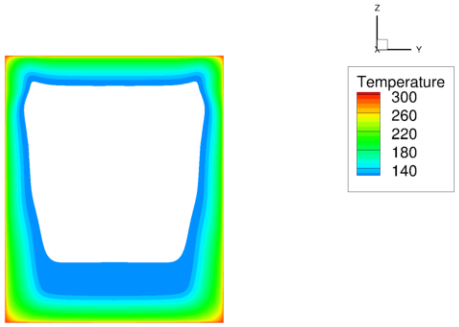

(a) Standard case CFD.

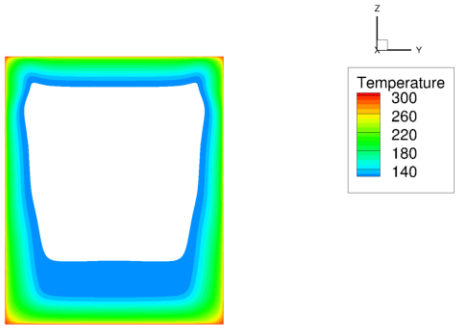

(b) Isothermal case CFD.

Figure 43: Freestream thermal boundary-layer at $x = -63.9$ mm. Temperature cut off is at 99% freestream (121.2 K).

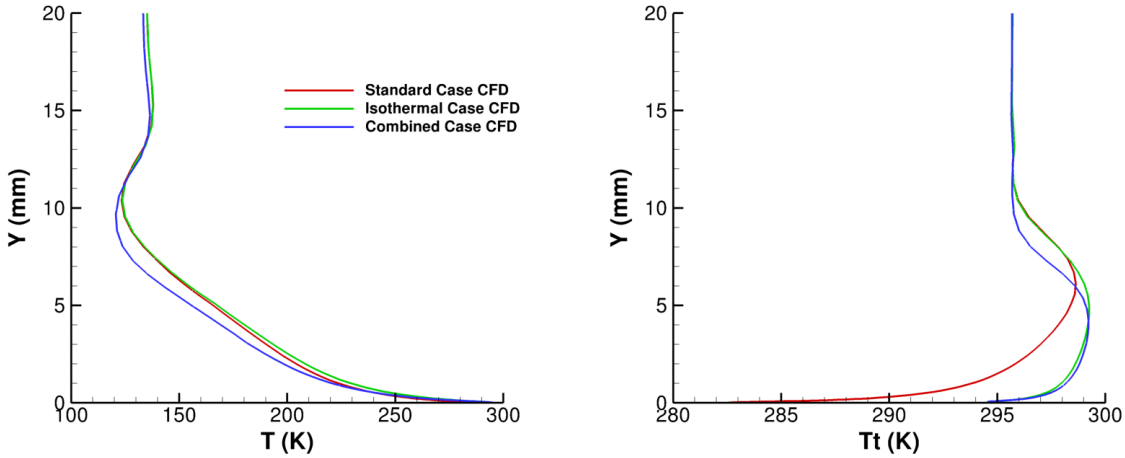

(a) Static temperature profiles.

(b) Total temperature profiles.

Figure 44: Temperature profiles at the most-upstream axial location ($x = 18.191$ mm).

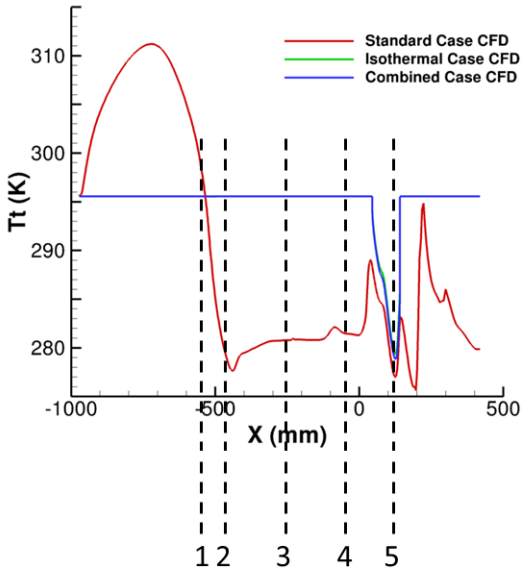

Figure 45: Total temperature centerspan profile at the bottom wall with the following stations marked: 1. Throat, 2. Trip location, 3. Start of the tunnel straight section, 4. Wedge leading edge, 5. Wedge trailing edge.

The differences in temperature do correspond to differences in velocity, as shown in Fig. 46. The Isothermal case is shown to be slightly worse than the Standard case as compared to the experimental data. The differences in the velocities can be seen more clearly in the difference contour plots shown in Figs. 47 and 48. The difference is defined as the Isothermal case minus the Standard case. It is shown that the

interaction region for the Isothermal case is further upstream compared to the Standard case, and therefore further away compared to the experimental data. The movement of the interaction region is also verified in the static temperature difference contour, shown in Fig. 49.

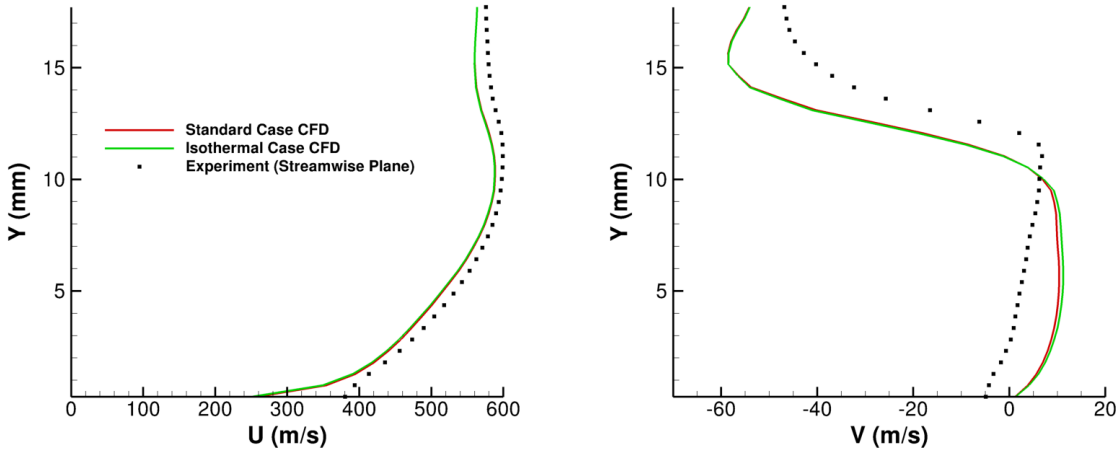

(a) u velocity profiles.

(b) v velocity profiles.

Figure 46: Select velocity profiles at the most-upstream axial location ($x = 18.191$ mm).

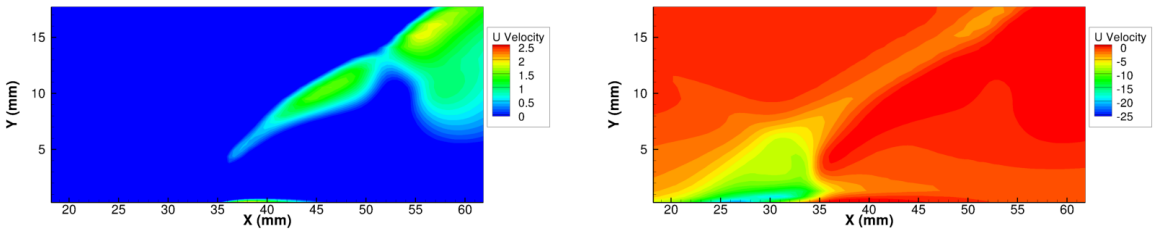

(a) Positive difference (m/s).

(b) Negative difference (m/s).

Figure 47: u velocity difference contours.

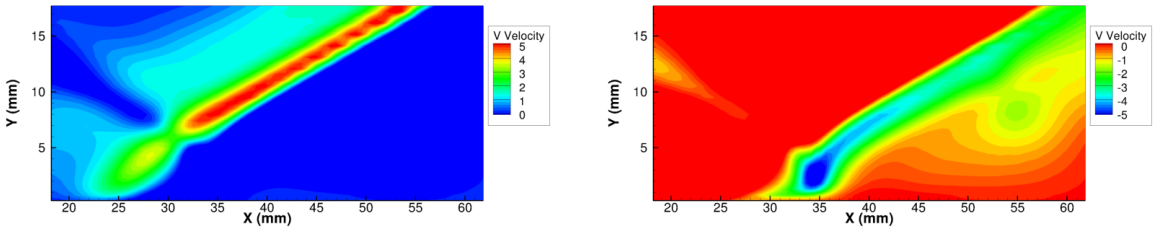

(a) Positive difference (m/s).

(b) Negative difference (m/s).

Figure 48: v velocity difference contours.

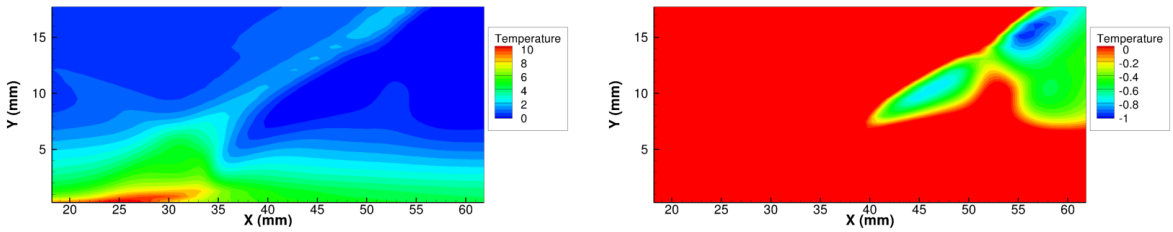

(a) Positive difference (K). (b) Negative difference (K).

Figure 49: Static temperature difference contours.

7.4 Trip Case

The effects of the Trip case are shown in Figs. 50 through 52. Figures 50 and 51 show that Trip and Combined cases agree well with the experimental data for the u velocity which suggests that assuming the flow is laminar at some portion upstream of the wedge is likely more correct than assuming it to be turbulent throughout. This further supports likely transition downstream of the throat based on the momentum thickness Reynolds number of the first laminar case. The closeness of the u velocity profiles in Figs. 50 and 51 for the Trip and Combined case indicates that the trip is a dominating factor that sets the Combined case apart from the Standard case. This is also evident in the turbulent kinetic energy profiles shown in Fig. 52. Having a laminar region upstream of the wedge allows for thinner boundary layers, and thus less blockage, upstream of the wedge. This is further quantified by the throat blockage parameter, with the Trip case having a throat blockage of 1.11%, which is less than the 1.53% that it was for the Standard case.

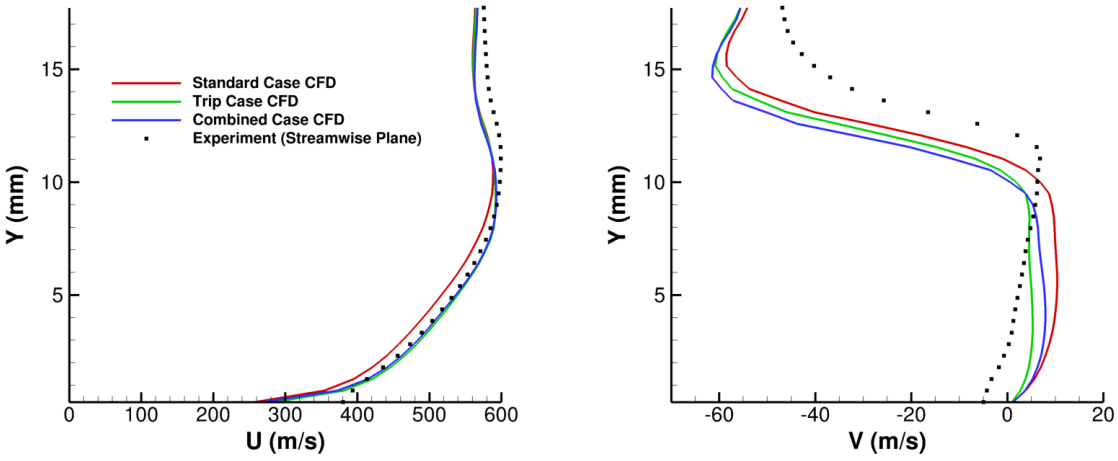

(a) u velocity profiles. (b) v velocity profiles.

Figure 50: Select velocity profiles at the most-upstream axial location ($x = 18.191$ mm).

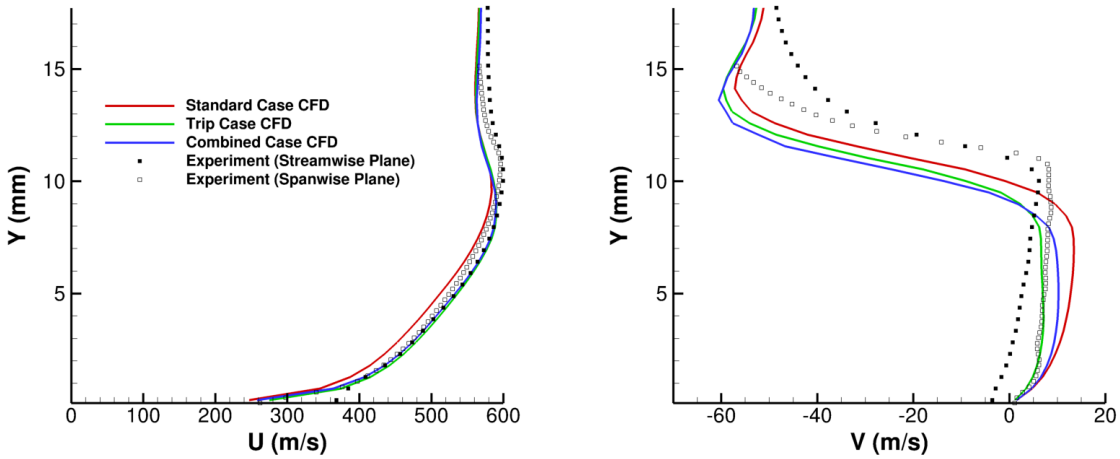

(a) u velocity profiles.

(b) v velocity profiles.

Figure 51: Select velocity profiles at the first intersecting spanwise plane ($x = 20.76$ mm).

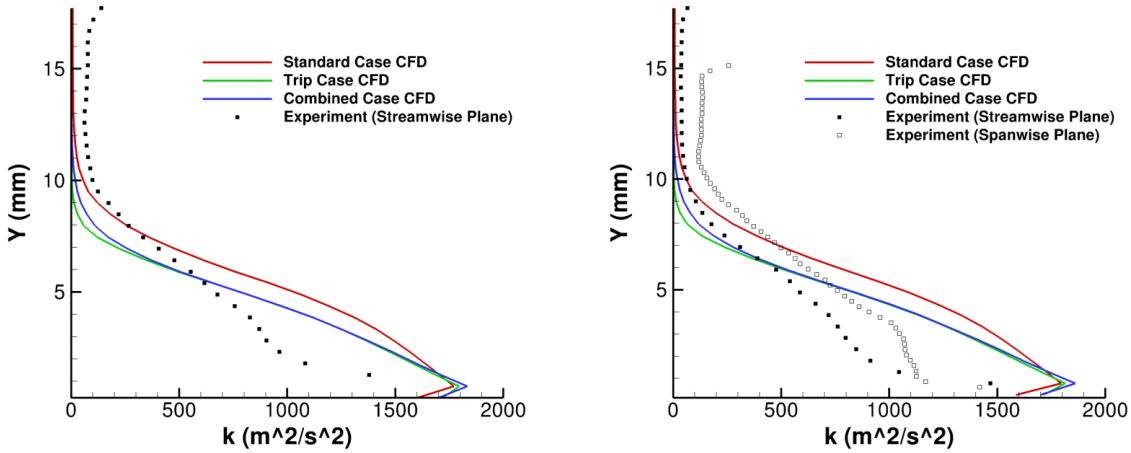

(a) At $x = 18.191$ mm.

(b) At $x = 20.76$ mm.

Figure 52: Turbulent kinetic energy profiles.

Examining the v velocity profiles in Fig. 51 shows that the experimental data from the spanwise and streamwise planes do not agree with each other. In fact, the CFD solutions are shown to match the experimental data from the spanwise plane better than compared to the streamwise plane. This is a key point when developing an error metric as the error metric used in the prior workshop focused solely on the experimental data in the streamwise plane and not the spanwise plane.

7.5 Turbulence Modeling Effects

Figures 53 and 54 show velocity profiles while Fig. 55 shows the turbulent kinetic energy profile for the TKE and MUT case. It can be seen that the velocity profiles for the TKE case compare better to the experimental data than the Standard case does, however, the TKE case still predicts lower freestream velocities. It can also be shown that the dominating factor is the increase in freestream turbulent kinetic energy and not the increase in freestream turbulent viscosity. However this domination is in part due to that the inlet freestream turbulent viscosity was increased by only 10x while the inlet freestream turbulent kinetic energy was increased by 10,000x. The same conclusions can also be made with the turbulent kinetic energy profiles of Fig. 55.

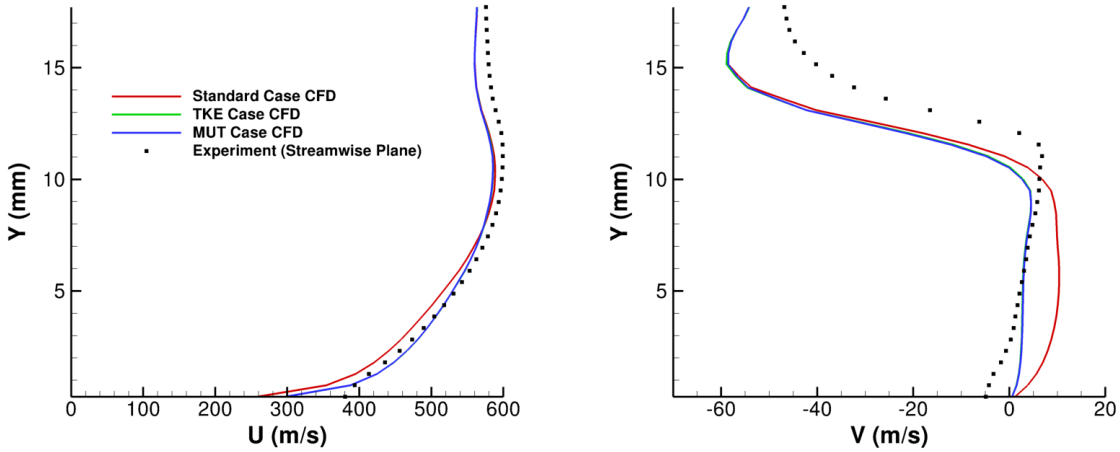

(a) u velocity profiles.

(b) v velocity profiles.

Figure 53: Select velocity profiles at the most-upstream axial location ($x = 18.191$ mm).

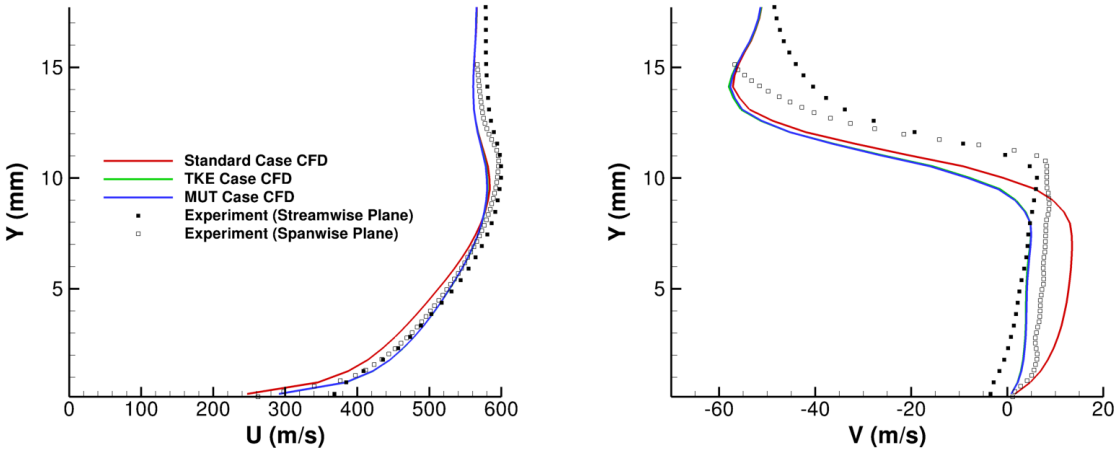

(a) u velocity profiles. (b) v velocity profiles.

Figure 54: Select velocity profiles at the first intersecting spanwise plane ($x = 20.76$ mm).

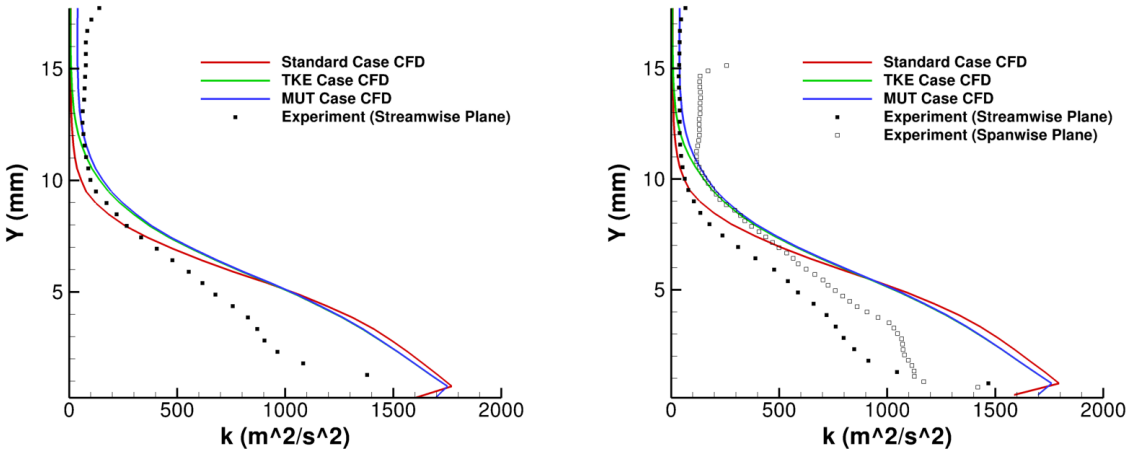

(a) At $x = 18.191$ mm. (b) At $x = 20.76$ mm.

Figure 55: Turbulent kinetic energy profiles.

Figures 56 and 57 show the velocity profiles for the various turbulence models tested for the Standard case conditions. Additional velocity profiles can be found in appendix B. It can be seen that both BSL and SST-GY predict higher u velocities in the boundary layer and thus tend to agree better with the experimental values compared to the SST case. This is also true for the v velocities within the boundary layer region. However, all three turbulence models are the same for the freestream velocities. The greatest impact of the turbulence models can be seen in the blockage effects. Figure 58 shows the bottom wall separation underneath the wedge. It can clearly be seen that the corner flow separation greatly decreases with turbulence models that

allow for greater shear stress transport. However, the center separation bubble is shown to increase slightly in the spanwise direction with decreasing corner flow separation. This is consistent with the experimentally shown coupling mentioned earlier. It is also shown that the corresponding throat blockage also decreases, from the 1.53% with SST to 1.51% with SST-GY to 1.49% with BSL. A similar turbulence model study was also performed for the Combined case conditions, which can be found in appendix C.

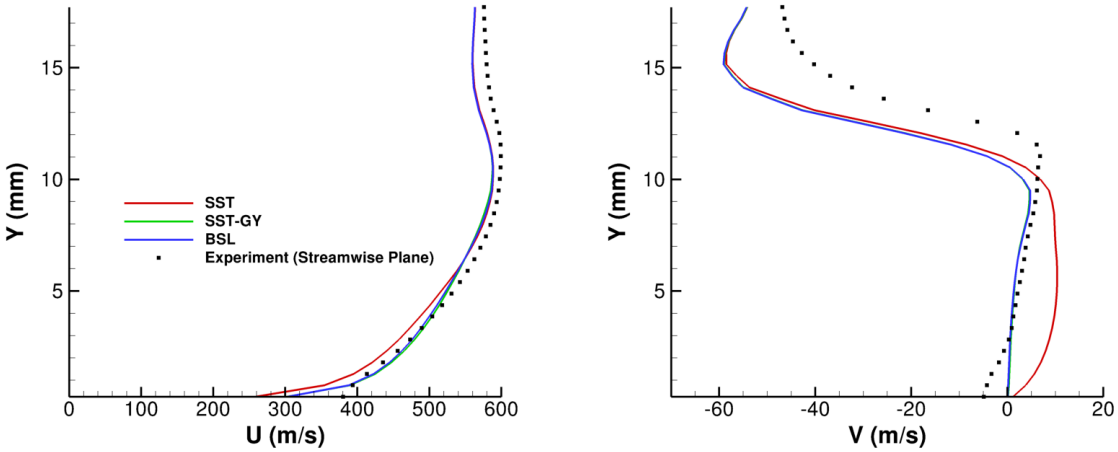

(a) u velocity profiles.

(b) v velocity profiles.

Figure 56: Velocity profiles at the most-upstream axial location (x = 18.191 mm) for various turbulence models, Standard Case.

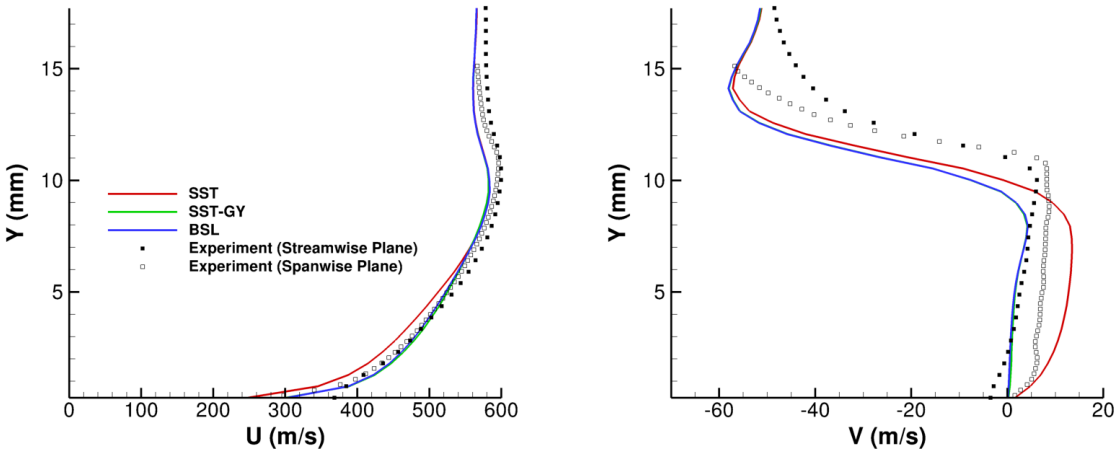

(a) u velocity profiles.

(b) v velocity profiles.

Figure 57: Velocity profiles at the first intersecting spanwise plane (x = 20.76 mm) for various turbulence models, Standard Case.

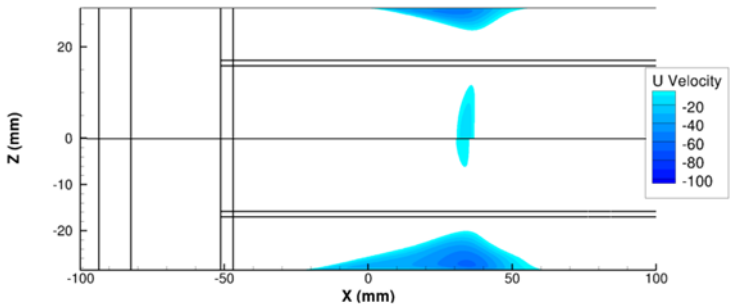

(a) SST-GY (positive span) and SST (negative span).

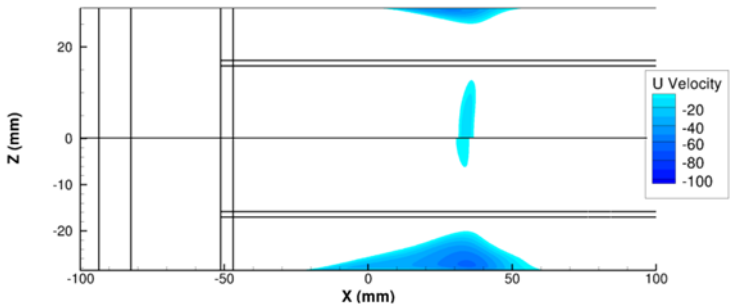

(b) BSL (positive span) and SST (negative span).

Figure 58: Bottom wall separation underneath the wedge for the Standard case with various turbulence models.

7.6 Metrics

To compare the CFD data with the prior CFD data from the workshop, the following error metric was used [19]:

$$e\left(f\right)_n = \left|\left(f_{cfd}\right)_n - \left(f_{exp}\right)_n\right| \tag{96}$$

$$E\left(f\right) = \frac{1}{N}\sum e\left(f\right)_n \tag{97}$$

The error metric was summed over the entire streamwise data plane with metric results shown in Table 5. Cases submitted to the workshop are designated by letters while the cases presented in this paper are in bold face. It can be seen that the Standard case ranks best out of the cases presented and the addition of the lag improves both the Standard and Combined cases. Although the metric is a useful quantity for comparison, it must be used in combination with all the data. All improvements to matching the data must be for the right reasons. Although the Standard case with the PIV lag corrections have a smaller v velocity error, the physics of the Combined case is likely more correct.

Table 5: Workshop error metric comparisons.

U Error		V Error	
0.02373	Q	0.008947	Experiment
0.02633	B	**0.01158**	**Standard (Medium Lag)**
0.02669	P	**0.01185**	**Standard (Long Lag)**
0.02676	**Standard (Long Lag)**	**0.01224**	**Standard (Short Lag)**
0.02747	**Standard (Medium Lag)**	**0.01308**	**MUT**
0.02759	G	**0.01331**	**TKE**
0.02840	F	**0.01348**	**Combined (Medium Lag)**
0.02853	**Standard (Short Lag)**	**0.01360**	**Combined (Short Lag)**
0.02899	M	**0.01375**	**Combined (Long Lag)**
0.02957	I	**0.01377**	**Standard**
0.02964	**Standard**	**0.01403**	**Combined**
0.02999	K	**0.01414**	**Trip**
0.03020	**Standard (SST-GY)**	0.01449	B
0.03025	**Combined (Short Lag)**	**0.01514**	**Isothermal**
0.03035	N	**0.01621**	**Modified Geometry**
0.03036	**Combined (Medium Lag)**	0.01682	P
0.03043	**TKE**	0.01716	G
0.03043	**MUT**	0.01729	F
0.03047	**Combined**	0.01771	M
0.03064	**Combined (Long Lag)**	0.01828	Q
0.03090	**Isothermal**	0.01867	K
0.03114	**Modified Geometry**	0.01917	N
0.03115	**Standard (BSL)**	**0.01950**	**Standard (SST-GY)**
0.03129	O	0.01961	O
0.03163	**Trip**	**0.02227**	**Standard (BSL)**
0.03473	Experiment	0.02344	J
0.03571	H	**0.02348**	**Combined (SST-GY)**
0.03739	**Combined (SST-GY)**	**0.02576**	**Combined (BSL)**
0.03856	**Combined (BSL)**	0.02721	H
0.03980	L	0.03883	L
0.03995	J	0.04002	I

One possible metric to be used in conjunction with the workshop metric is a comparison of the u velocities at points of interest. For this study, two points were chosen: points A and B in Fig. 59. Point A was chosen outside the data plane, upstream of the wedge and at center height and span to capture a freestream point. Point B was chosen within the data plane at u_{max} at the upstream most axial location. Velocity and velocity differences are shown in Table 6. The velocity difference is defined as the current case minus the Standard case. Interestingly, the Combined case difference at Point A is reflected as a buildup of the previous differences. This is not true at Point B, but as seen in Fig. 59, the flow at Point B is not truly at freestream conditions with an apparent decrease in Mach number (and thus decreases in u velocity). This in part explains why the workshop error metric predicts the Standard case as being better than the Combined case as the data used in workshop error metric is derived from at/downstream of Point B. Also, the highest u

velocity at Point B from all the simulations is still 11.6 m/s lower than the experimental value and should be just upstream of the shock.

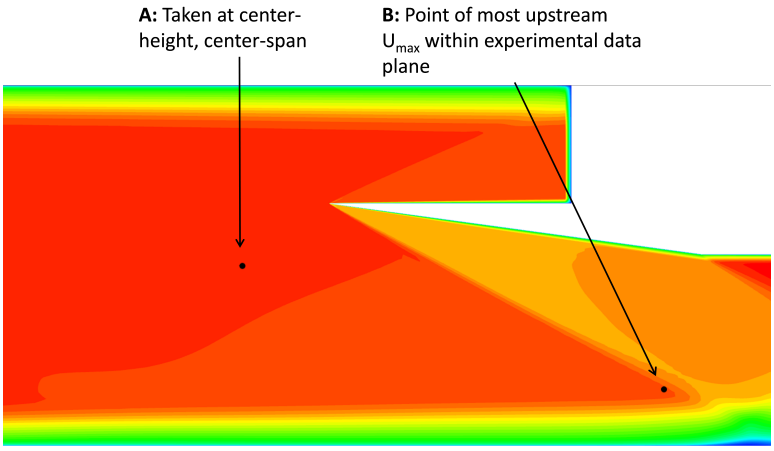

Figure 59: Point locations within the centerspan plane. Mach number contour of the Standard case CFD solution is shown.

Table 6: u velocity and velocity differences.

	Point A		Point B	
	U (m/s)	$\triangle$U (m/s)	U (m/s)	$\triangle$U (m/s)
Standard	594.600	0.000	587.042	0.000
Isothermal	594.454	-0.146	586.377	-0.665
Modified Geometry	596.567	1.967	586.413	-0.629
Trip	595.186	0.586	587.737	0.695
Combined	596.980	2.380	587.038	-0.004
Experiment	-	-	599.330	12.288

Another proposed complementary metric would be the use of the oblique shock angle off the leading edge of the wedge. The shock angle was calculated by finding the angle between the leading edge of the wedge and a point downstream with the max second derivative of a scaled arc length. For details on how the shock angle was calculated, see appendix D. The calculated shock angles for the various cases as well as for the experimental data are shown in Table 7. It can be seen that the shock angle does not change much between the cases, but the addition of the lag brings it to within the experimental value. A comparison to quasi-1D theory is shown in Fig. 60. It can be seen that the shock angle cannot be calculated based on the quasi-1D theory due to the 3D nature of the shocks present in the flow. The advantage of this metric is that separate experimental evaluations of the shock angle are possible: from detailed PIV to optical methods such as schlieren.

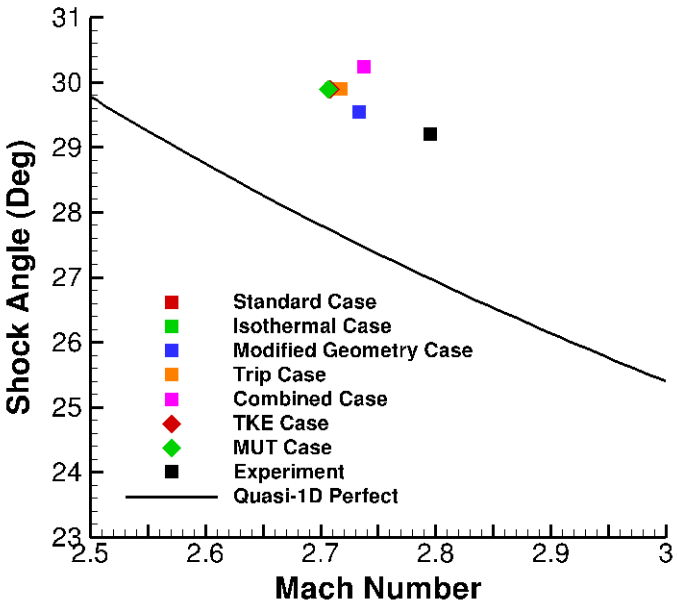

Figure 60: Shock angle verses Mach number.

Table 7: Shock angle comparisons.

	Shock Angle (deg)
Standard	29.888
Standard (BSL)	29.888
Standard (SST-GY)	29.888
Isothermal	29.888
Modified Geometry	29.543
Trip	29.888
Combined	30.231
Combined (BSL)	30.231
Combined (SST-GY)	30.231
TKE	29.888
MUT	29.888
Standard (Short Lag)	29.196
Standard (Medium Lag)	29.196
Standard (Long Lag)	28.494
Combined (Short Lag)	29.543
Combined (Medium Lag)	29.543
Combined (Long Lag)	28.846
Experiment	29.196

7.7 Blockage Revisited

Figures 61 and 62 show the bottom wall separations underneath the wedge for several of the cases presented. Separations are shown to be similar between cases, but there are noticeable differences. In particular, the Modified Geometry case was shown to have the most corner flow separation while the Trip case was shown to have the least corner separation out of all the cases run with SST. This is further quantified by the throat blockage parameter as the Modified Geometry case had 1.56% throat blockage compared to 1.11% of the Trip case. The separation regions can also help explain why velocities at Point B (located underneath the wedge) tended to decrease compared to the Standard Case while the velocities at Point A (upstream of the wedge) increased. The respective increase or decrease is most noticeable for cases with more separation. The extent of the separations was thought to be due mostly to details within the turbulence model, however, these results show that there are many sources that impact the separations and respective blockages.

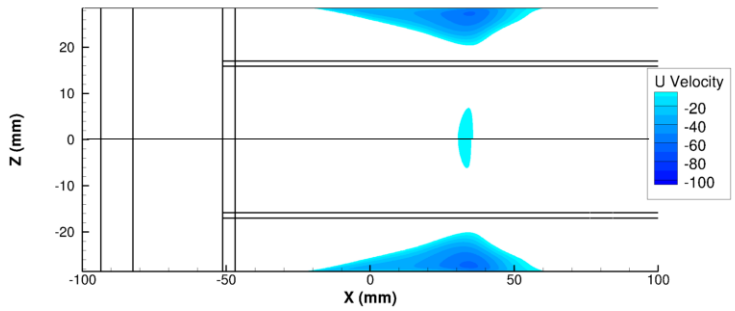

(a) Isothermal case (positive span) and Standard case (negative span).

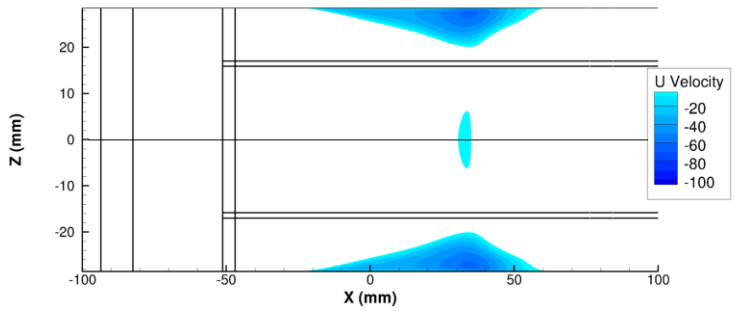

(b) Modified Geometry case (positive span) and Standard case (negative span).

Figure 61: Bottom wall separation underneath the wedge for the Isothermal and Modified Geometry cases.

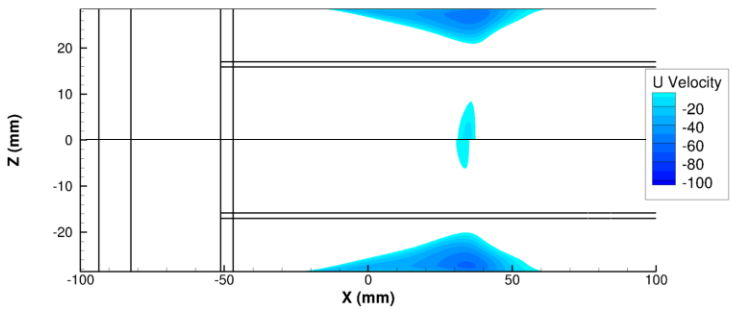

(a) Trip case (positive span) and Standard case (negative span).

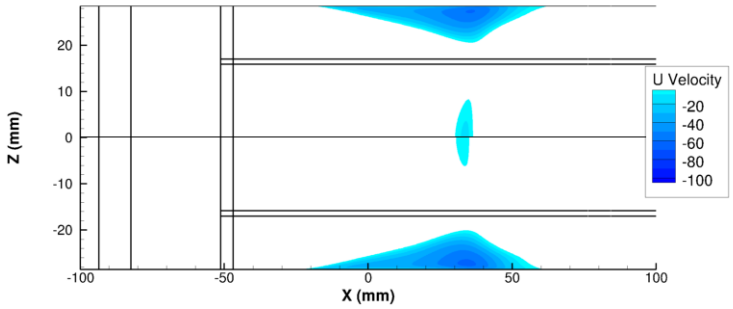

(b) Combined case (positive span) and Standard case (negative span).

Figure 62: Bottom wall separation underneath the wedge for the Trip and Combined cases.

8 Conclusions/Future Work

CFD analyses were performed on the UM Mach 2.75 Glass Tunnel with a 7.75 degree semi-span wedge (a test case used at a recent SBLI workshop) to explore key physics pertaining to SBLI's. It was shown that the CFD generally under predicted the freestream velocities, however the solutions showed improvement, particularly the v velocity component, with several sensitivity insights. These included the addition of a laminar region upstream of the wedge with a specified trip point as well as geometry that reflects the current state of the tunnel. The flow was shown to be most likely transitional downstream of the throat. This is based on the analysis of the momentum thickness Reynolds number for the laminar case as well as the improved velocity profiles in the boundary layer upstream of the shock for cases that accounted for the transition. Other sensitivities explored included using an isothermal boundary condition, throat geometry modifications, and several turbulence models and turbulence model parameter sensitivities. Also, a fraction of the measured PIV lag was used with a simple model to modify the CFD solutions and showed improvement to the comparison to the PIV results. It showed that the velocity of the PIV particle is not the velocity of the air behind the shock, and the difference is larger than one would like for a validation test case. Future comparisons should have the CFD results augmented in a post-processing step to calculate particle velocities.

A variety of metrics were used to capture the results presented in this thesis. One metric used was the primary metric from the workshop: a root mean square error norm of the difference between the measured u and v velocities. Almost all cases presented in this thesis show improvement in that metric for v velocities as compared to the cases run for the workshop. The u velocity errors were better than the experimental uncertainty except for two cases. Two new error metrics have been proposed that are felt to be complimentary and help establish confidence that the physics is correct. These include a velocity upstream of the interaction and the center-span shock angle.

Although several sensitivities were presented in this thesis, there are still several sensitivities that have not been addressed. Additional geometric parameters of interest include the wedge leading edge location and angle, wedge width and location within the tunnel, and noticeable wall indents from micro ramp accommodations. These parameters would shed more insight into the sensitivity of the geometry on the oblique shock. Sensitivities to the turbulence model and freestream turbulent kinetic energy should be explored further to address the impact of the corner flows, and therefore replicate the correct blockage on the freestream flow field. Further explorations of the heat transfer boundary conditions should be explored, such as conjugate heat transfer and the sensitivity to changes in wall temperature which is known to change throughout experimental test runs on a given day. Also, future studies should explore boundary-layer transition/trip location as the flow is most certainly transitional downstream of the throat. Aside from the geometric and flow sensi-

tivities, the simplified PIV models should be improved on in order to further understand the effects of PIV as related to post-processing CFD data for experimental data comparison. Improvements include calculating the particle lag based on the forces exerted on the individual particles by the air (including particle size distribution) and obtaining flow field snapshots at two instances in time. These snapshots would then be processed using the same PIV post-processing algorithm used with the experimental data.

References

[1] Pitt Ford, C. W. and Babinsky, H., "Micro-Ramp Control for Oblique Shock Wave/Boundary Layer Interactions," Tech. Rep. AIAA 2007-4115, University of Cambridge, June 2007.

[2] Touber, E. and Sandham, N. D., "Large Eddy Simulation of Low-Frequency Unsteadiness in a Turbulent Shock-Induced Separation Bubble," *Theoretical and Computational Fluid Dynamics*, Vol. 23, No. 2, 2009, pp. 79–107.

[3] Galbraith, D. S., *Computational Fluid Dynamics Investigation into Shock Boundary Layer Interactions in the Glass Inlet Wind Tunnel*, Master's thesis, University of Cincinnati, Cincinnati, OH, 2011.

[4] Holden, H. A. and Babinsky, H., "Shock / Boundary Layer Interaction Control using 3D Devices," Tech. Rep. AIAA 2003-447, Cambridge University, January 2003.

[5] Ghosh, S., Choi, J., and Edwards, J. R., "Numerical Simulation of the Effects of Mesoflaps in Controlling Shock/Boundary Layer Interactions," Tech. Rep. AIAA 2010-4465, North Carolina State University, June 2010.

[6] Morgan, B., Kawai, S., and Lele, S. K., "Large-Eddy Simulation of an Oblique Shock Impinging on a Turbulent Boundary Layer," Tech. Rep. AIAA 2010-4467, Stanford University, June 2010.

[7] Medic, G., Chen, L., Feng, J., and Sharma, O., "Towards Large-Eddy Simulation of Turbulent Flow in a Centrifugal Impeller," Tech. Rep. GT2011-45804, United Technologies Research Center, June 2011.

[8] Knight, D., H., Y., Panaras, A. G., and Zheltovodov, A., "Advances in CFD Prediction of Shock Wave Turbulent Boundary Layer Interactions," *Progress in Aerospace Sciences*, Vol. 39, No. 2, February 2003, pp. 121–184.

[9] Wu, M., Taylor, E. M., and Martin, M. P., "Assessment of STBLI DNS Data for Comparision against Experiments," Tech. Rep. AIAA 2005-4895, Princeton University, June 2005.

[10] Wu, M. and Martin, M. P., "The Assessment of Numerical Methods for Shockwave/Turbulent Boundary Layer Interaction," Tech. Rep. AIAA 2006-717, Princeton University, January 2006.

[11] Edwards, J. . R., Choi, J., and Boles, J. A., "Large-Eddy/Reynolds-Averaged Navier-Stokes Simulation of a Mach 5 Compression-Corner Interaction," *AIAA Journal*, Vol. 46, No. 4, 2008, pp. 977–991.

[12] Lapsa, A. P., *Experimental Study of Passive Ramps for Control of Shock-Boundary Layer Interactions*, Ph.D. thesis, University of Michigan, Ann Arbor, MI, 2009.

[13] Rumsey, C. L., Smith, B. R., and Huang, G. P., "Description of a Website Resource for Turbulence Model Verification and Validation," Tech. Rep. AIAA 2010-4742, NASA Langley Research Center, June 2010.

[14] Bhagwandin, V. A. and DeSpirito, J., "Numerical Prediction of Supersonic Shock-Boundary Layer Interaction," Tech. Rep. AIAA 2011-859, US Army Research Laboratory, January 2011.

[15] Rumsey, C. L., "CFL3D Contribution to the AIAA Supersonic Shock Boundary Layer Interaction Workshop," Tech. Rep. NASA/TM 2010-216858, Langley Research Center, October 2010.

[16] Georgiadis, N. J., Vyas, M. A., and Yoder, D. A., "Wind-US Code Contributions to the First AIAA Shock Boundary Layer Interaction Prediction Workshop," Tech. Rep. NASA/TM 2013-217837, Glenn Research Center, February 2013.

[17] Dupont, P., Piponniau, S., Sidorenko, A., and Debieve, J., "Investigation by Particle Image Velocimetry Measurements of Oblique Shock Reflection with Separation," *AIAA Journal*, Vol. 46, No. 6, 2008, pp. 1365–1370.

[18] Lapsa, A. P. and Dahm, W. J. A., "Stereo Particle Image Velocimetry of Nonequilibrium Turbulence Relaxation in a Supersonic Boundary Layer," *Experiments in Fluids*, Vol. 50, No. 1, 2010, pp. 89–108.

[19] DeBonis, J. R., Oberkampf, W. L., Wolf, R. T., Orkwis, P. D., Turner, M. G., Babinsky, H., and Benek, J. A., "Assessment of CFD Models for Shock Boundary-Layer Interaction," *AIAA Journal*, Vol. 50, No. 4, 2012, pp. 891–903.

[20] Benek, J. A., "Overview of the 2010 AIAA Shock Boundary Layer Interaction Prediction Workshop," Tech. Rep. AIAA 2010-4821, Air Force Research Laboratory, June 2010.

[21] Benek, J. A., "Lessons Learned from the 2010 AIAA Shock Boundary Layer Interaction Prediction Workshop," Tech. Rep. AIAA 2010-4825, Air Force Research Laboratory, June 2010.

[22] Hirsch, C., "SBLI Lessons Learned: CFD Simulations of Two Test Cases," Tech. Rep. AIAA 2010-4824, Numeca Int., July 2010.

[23] Galbraith, D. J., Turner, M. G., Orkwis, P. D., and Weil, S. P., "The Effect of Aspect Ratio on a Mach 2.75 Shock Boundary layer Interaction Configuration," Tech. Rep. AIAA 2013-861, US Air Force Research Laboratory, January 2013.

[24] Holden, H. A. and Babinsky, H., "Vortex Generators Near Shock / Boundary Layer Interactions," Tech. Rep. AIAA 2004-1242, Cambridge University, January 2004.

[25] Babinsky, H., Oorebeek, J., and Cottingham, T. G., "Corner Efefcts in Reflecting Oblique Shock-Wave/Boundary-Layer Interactions," Tech. Rep. AIAA 2013-859, Cambridge University, January 2013.

[26] Titchener, N., Bruce, P., and Babinsky, H., "An Experimental Investigation of Corner Bleed Applied to a Normal Shock-Wave/Boundary-Layer Interaction and Diffuser," Tech. Rep. AIAA 2011-69, University of Cambridge, January 2011.

[27] Hunt, D. and Nixon, D., "A Aery Large Eddy Simulation of an Unsteady Shock Wave / Turbulent Boundary Layer Interaction," Tech. Rep. AIAA 95-2122, Queen's University, June 1995.

[28] Dolling, D. S. and Murphy, M. T., "Unsteadiness of the Separation Shock-Wave Structure in Supersonic Compression Ramp Flowfield," *AIAA Journal*, Vol. 21, No. 12, 1983, pp. 1628–1634.

[29] Jammalamadaka, A., Li, Z., and Jaberi, F. A., "Large-Eddy Simulation of Turbulent Boundary Layer Interaction with an Oblique Shock Wave," Tech. Rep. AIAA 2010-110, Michigan State University, January 2010.

[30] Knight, D. and Degrez, G., "Shock Wave Boundary Layer Interactions in High Mach Number Flows - A Critical Survey of Current CFD Predictions Capabilities," *AGARD AR-319*, Vol. 2, 1998.

[31] Zheltovodov, A. A., "Some Advances in Research of Shock Wave Turbulent Boundary Layer Interactions," Tech. Rep. AIAA 2006-0496, Institute of Theoretical and Applied Mathematics, Siberian Branch of Russian Academy of Science, January 2006.

[32] Edwards, J., "Numerical Simulations of Shock/Boundary Layer Interactions using Time-Dependent Modeling Techniques - a Survey of Recent Results," Tech. Rep. AIAA 2013-525, North Carolina State University, January 2008.

[33] Zheltovodov, A. A., Zaulichnii, E. G., Trofimov, V. M., and Yakolev, V. N., "Heat Transfer and Turbulence Study in Compressible Separated Flows," Tech. Rep. Preprint 22-87, Institute Theoretical and Applied Mechanics, Russian Academy of Sciences, 1987.

[34] Zheltovodov, A., Maksimov, A., and Shevchenko, A., "Topology of Three-Dimensional Separation Under the Conditions of Symmetric Interaction of Crossing Shocks and Expansion Waves with Turbulent Boundary Layer," *Thermophysics and Aeromechanics*, Vol. 5, No. 3, 1998, pp. 293–312.

[35] Martin, M. P., Xu, S., and Wu, M., "Preliminary work on DNS and LES of STBLI," Tech. Rep. AIAA 2003-3464, Princeton University, June 2003.

[36] Wu, M. and Martin, M. P., "Direct Numerical Simulation of Shockwave/Turbulent Boundary Layer Interactions," Tech. Rep. AIAA 2004-2145, Princeton University, June 2004.

[37] Wu, M., Bookey, P., Martin, M. P., and Smits, A., "Analysis of Shockwave/Turbulent Boundary Layer Interaction using DNS and Experimental Data," Tech. Rep. AIAA 2005-310, Princeton University, January 2005.

[38] Martin, M. P., Smits, A. J., Wu, M., and Ringuette, M., "The Turbulence Structure of Shockwave and Boundary Layer Interaction in a Compression Corner," Tech. Rep. AIAA 2006-497, Princeton University, January 2006.

[39] Wu, M. and Martin, M. P., "Direct Numerical Simulation of Supersonic Turbulent Boundary Layer Over a Compression Ramp," *AIAA Journal*, Vol. 45, No. 4, 2007, pp. 879–889.

[40] Bookey, P. B., Wu, M., Smits, A. J., and Martin, M. P., "New Experimental Data of STBLI at DNS/LES Accessible Reynolds Numbers," Tech. Rep. AIAA 2005-309, Princeton University, January 2005.

[41] Menter, F. R., "Two-Equation Eddy Viscosity Turbulence Models for Engineering Applications," *AIAA Journal*, Vol. 32, No. 8, 1994, pp. 1598–1605.

[42] Georgiadis, N. J. and Yoder, D. A., "Recalibration of the Shear Stress Transport Model to Improve Calculation of Shock Separated Flows," Tech. Rep. AIAA 2013-0685, NASA Glenn Research Center, January 2013.

[43] Tan, J. and Jin, J., "Stress Limiter Consideration for k-ω Turbulence Models in Shock Wave/Turbulent Boundary-Layer Interactions in Supersonic and Hypersonic Flows," Tech. Rep. AIAA 2011-3980, Beijing University of Aeronautics and Astronautics, June 2011.

[44] Gieseking, D. A., Choi, J. I., Edwards, J. R., and A., H. H., "Compressible Flow Simulations Using a New LES/RANS Model," *AIAA Journal*, Vol. 49, No. 10, 2011, pp. 2194–2209.

[45] Gieseking, D. A. and Edwards, J. R., "Study of a Compression-Ramp Interaction Using Large-Eddy Simulation/Reynolds-Averaged Navier-Stokes Models," *AIAA Journal*, Vol. 50, No. 10, 2012, pp. 2057–2068.

[46] Eagle, W. E., Driscoll, J. F., and Benek, J. A., "3-D Inlet Shock-Boundary Layer Interactions - PIV Database for the Second SBLI Workshop," Tech. Rep. AIAA 2012-3214, University of Michigan, June 2012.

[47] Nichols, R. H., and Buning, P. G., *User's manual for OVERFLOW 2.1, Version 2.1t*, NASA Langley Research Center, Hampton, VA, 2008.

[48] NASA Langley Research Center, "OVERFLOW Flow Solver, Version 2.2e," 2012, Hampton, VA.

[49] Toro, E. F., Spruce, M., and Speares, W., "Restoration of the Contact Surface in the HLL Riemann Solver," *Shock Waves*, Vol. 4, 1994, pp. 25–34.

[50] Koren, B., "Upwind schemes, multigrid and defect correction for the steady Navier-Stokes equations," *11th International Conference on Numerical Methods in Fluid Dynamics*, edited by D. Dwoyer, M. Hussaini, and R. Voigt, Vol. 323 of *Lecture Notes in Physics*, Springer Berlin / Heidelberg, 1989, pp. 344–348.

[51] Tramel, R. W. and Nichols, "A Highly Efficient Numerical Method for Overset-Mesh Moving-Body Problems," Tech. Rep. AIAA-97-2040, June 1997.

[52] Abu-Grannam, B. J. and Shaw, R., "Natural Transition of Boundary Layers - The Effects of Turbulence, Pressure Gradient, and Flow History," *Journal of Mechanical Engineering Science*, Vol. 22, No. 5, 1980, pp. 213–228.

[53] Garmann, D. J., Visbal, M. R., and Orkwis, P. D., "Three-Dimensional Flow Structure and Aerodynamic Loading on a Low Aspect Ratio, Revolving Wing," Tech. Rep. AIAA 2012-3277, Air Force Research Laboratory, June 2012.

[54] Garmann, D. J., Visbal, M. R., and Orkwis, P. D., "Numerical Investigation of Three-Dimensional Flow Structure About a Revolving Wing," Tech. Rep. FEDSM 2012-72388, Air Force Research Laboratory, 2012.

[55] Wilcox, D. C., "Reassessment of the Scale-Determining Equations for Advanced Turbulence Models," *AIAA Journal*, Vol. 26, No. 11, 1988, pp. 1299–1310.

[56] Wieghardt, K. and Tillman, W., "On the Turbulent Friction Layer for Rising Pressure," Tech. Rep. NACA-TM-1314, 1951.

[57] Spalding, D. B., *Conferance on International Developments in Heat Transfer, ASME, Boulder, CO, Part II*, 1961, pp. 439–446.

[58] Berger, M. J., Aftosmis, M. J., and Allmaras, S. R., "Progress Towards a Cartesian Cut-Cell Method for Viscous Compressible Flow," Tech. Rep. AIAA 2012-1301, January 2012.

[59] Klebanoff, P., "Charicteristics of Turbulence ina Boundary Layer with Zero Pressure Gradient," Tech. Rep. NACA-TR-1247, 1955.

[60] Wilcox, D. C., "Formulation of the k-ω Model Revisited," *AIAA Journal*, Vol. 46, No. 11, 2008, pp. 2823–2838.

[61] The MathWorks, Inc., "MATLAB, R2011a," 2011, 3 Apple Hill Drive Natick, MA 01760-2098.

[62] Lemmon, E. W., and Huber, M. L., and McLinden, M. O., *NIST Standard Referance Database 23: Reference Fluid Thermodynamic and Transport Properties - REFPROP, Version 9.0*, National Institute of Standards and Technology, Standard Reference Data Program, Gaithersburg, 2010.

[63] Kunz, O. and Wagner, W., "The GERG-2008 Wide-Range Equation of State for Natural Gases and Other Mixtures: An Expansion of GERG-2004," *Journal of Chemical and Engineering Data*, Vol. 57, No. 11, 2012, pp. 3032–3091.

[64] Kunz, O., Klimeck, R., Wagner, W., and Jaescke, M., "The GERG-2004 Wide-Range Equation of State for Natural Gases and Other Mixtures," Tech. Rep. GERG Technical Monograph 15, 2007.

[65] "Equations, Tables, and Charts for Compressible Flow," Tech. Rep. NACA-TR-1135, Ames Aeronautical Laboratory, 1953.

[66] Emanuel, G., *Analytical Fluid Dynamics*, CRC Press, 2nd ed., 2000.

[67] Tecplot, Inc., Bellevue, WA, *Tecplot 360, 2010 User's Manual*, 2010.

[68] Tecplot, Inc., "Tecplot 360," 2010, Bellevue, WA.

A Velocity Contours

This appendix contains the u and v velocity contours for the CFD cases presented.

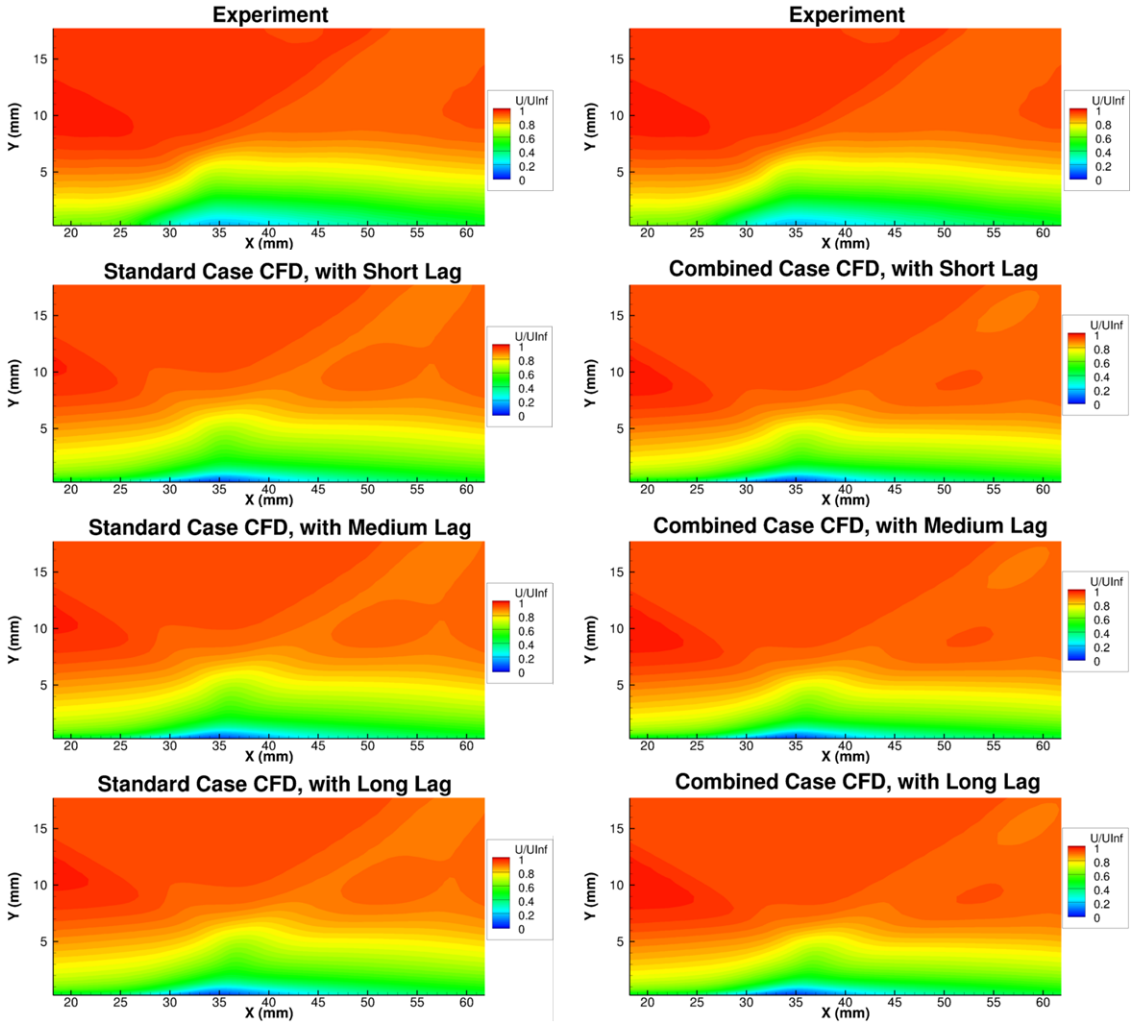

Figure A.1: u velocity contours for the Standard (left) and Combined (right) cases with lag.

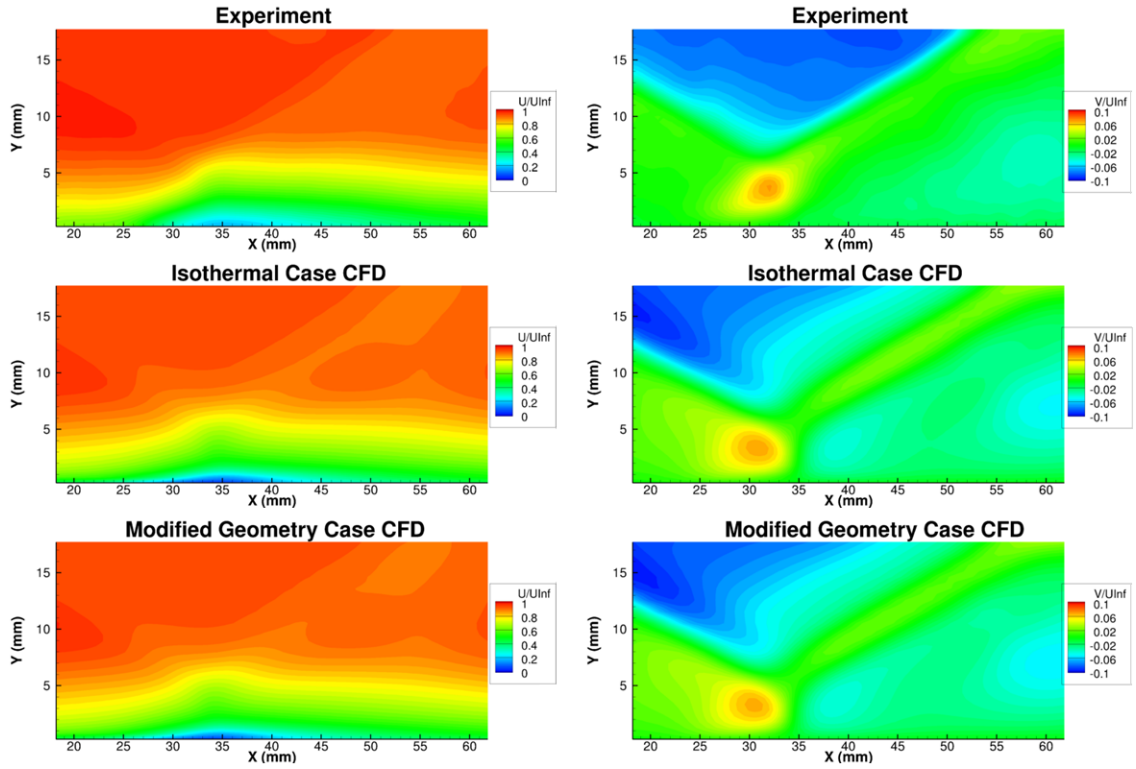

Figure A.2: u (left) and v (right) velocity contours for Isothermal and Modified Geometry cases.

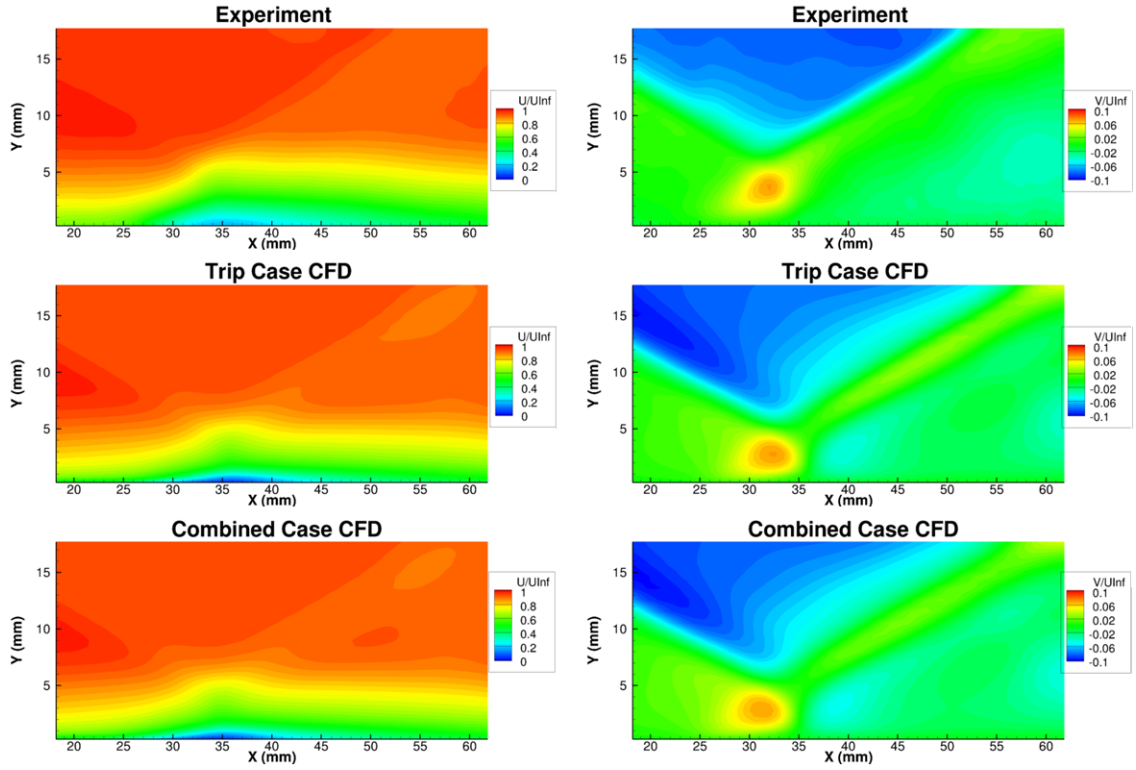

Figure A.3: u (left) and v (right) velocity contours for Trip and Combined cases.

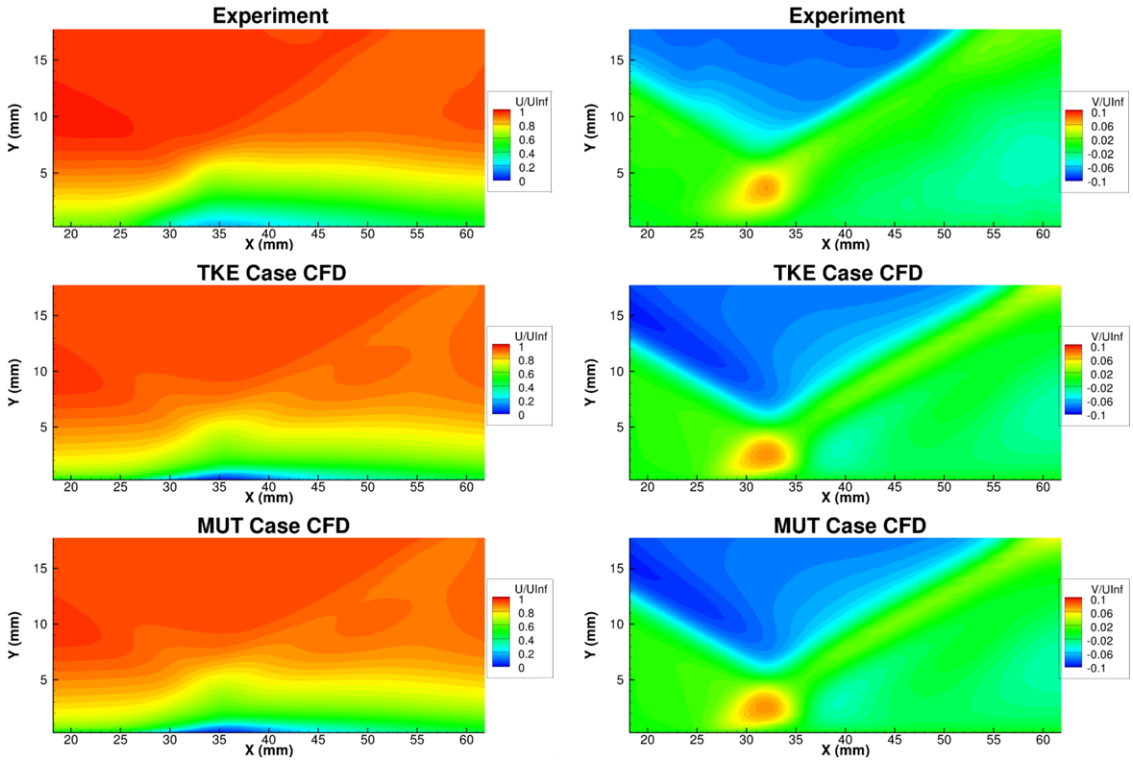

Figure A.4: u (left) and v (right) velocity contours for TKE and MUT cases.

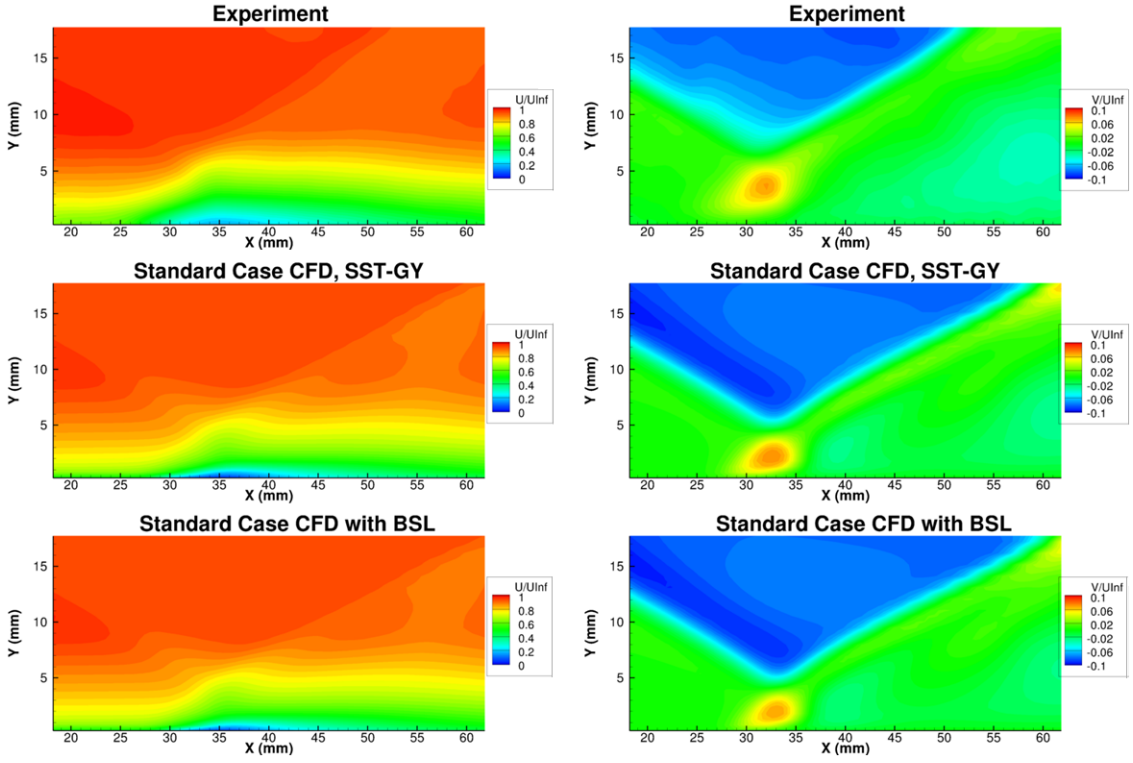

Figure A.5: u (left) and v (right) velocity contours for the Standard case with SST-GY and BSL.

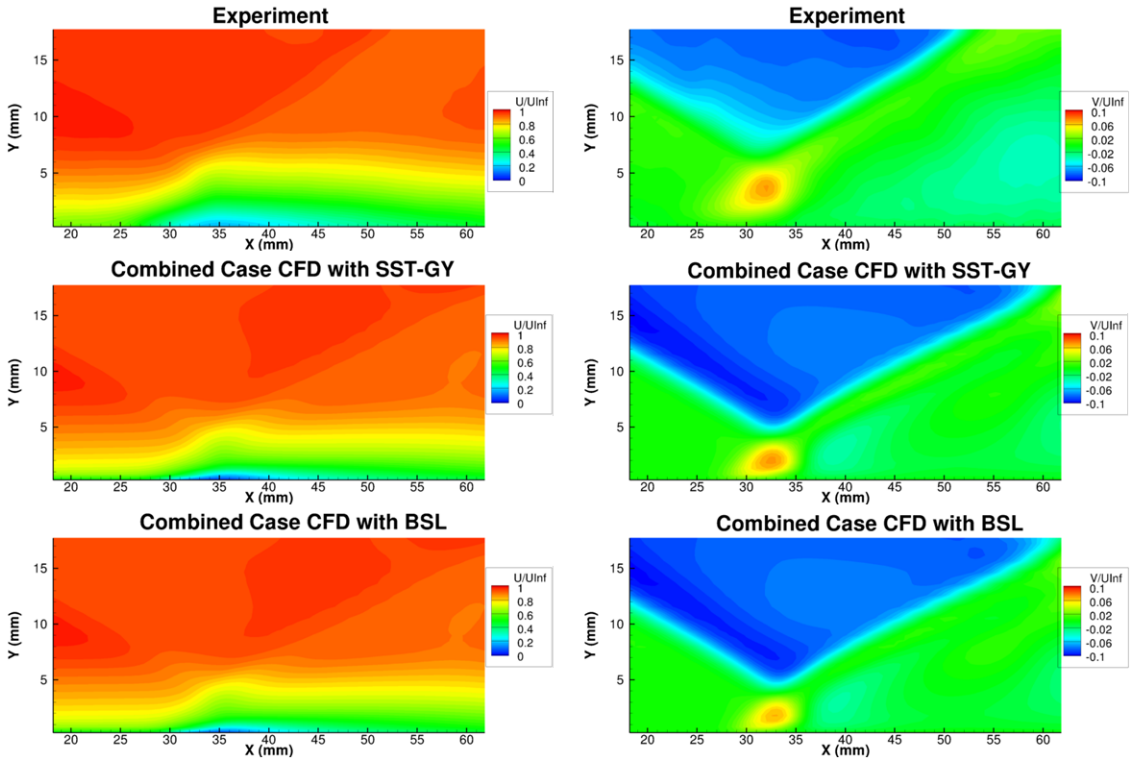

Figure A.6: u (left) and v (right) velocity contours for the Combined case with SST-GY and BSL.

B Velocity Profiles

This appendix contains velocity profiles for all remaining spanwise intersecting planes within the streamwise plane.

B.1 Standard Case

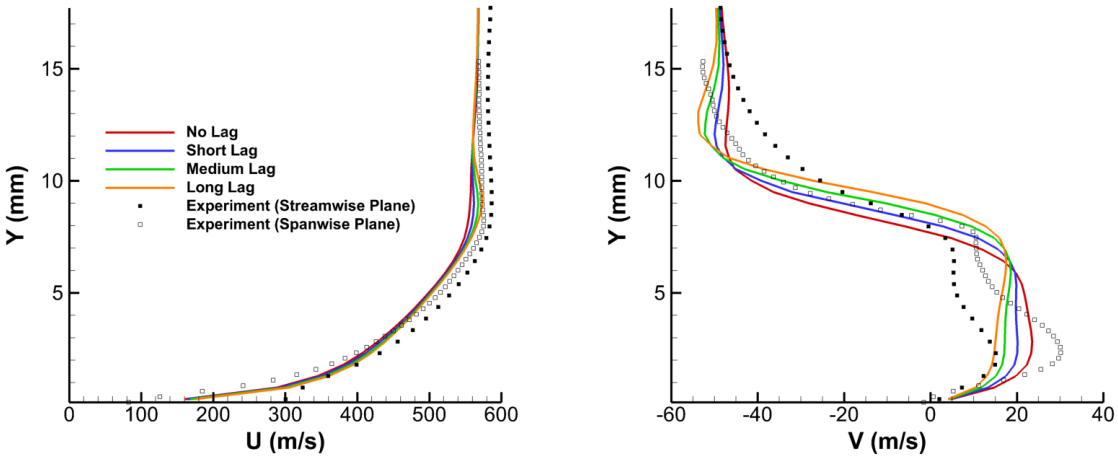

(a) u velocity profiles. (b) v velocity profiles.

Figure B.1: Velocity profiles at $x = 26.76$ mm, Standard case.

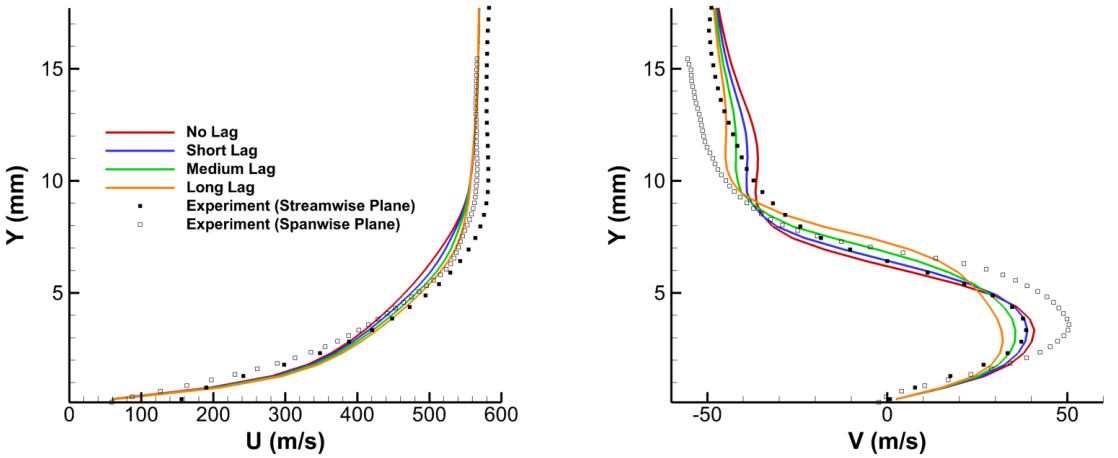

(a) u velocity profiles. (b) v velocity profiles.

Figure B.2: Velocity profiles at $x = 30.76$ mm, Standard case.

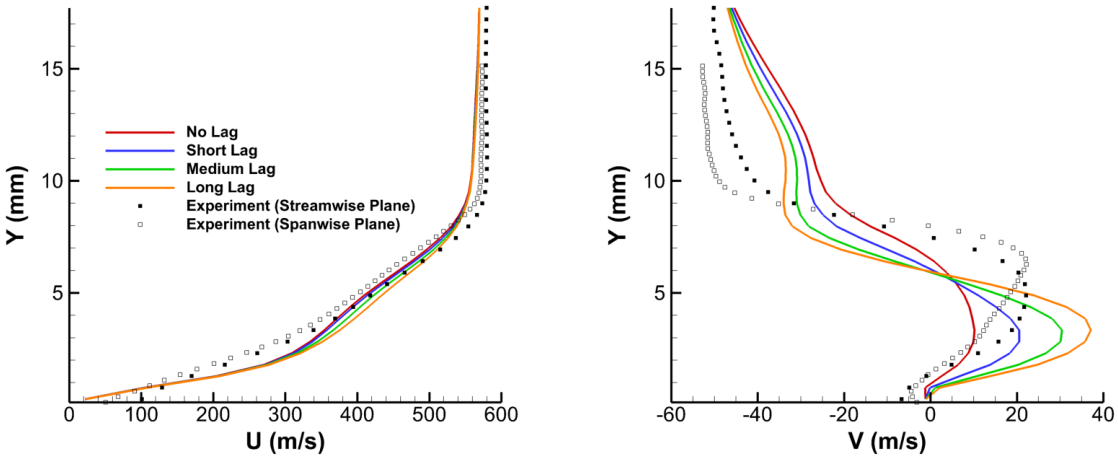

(a) u velocity profiles.

(b) v velocity profiles.

Figure B.3: Velocity profiles at $x = 34.76$ mm, Standard case.

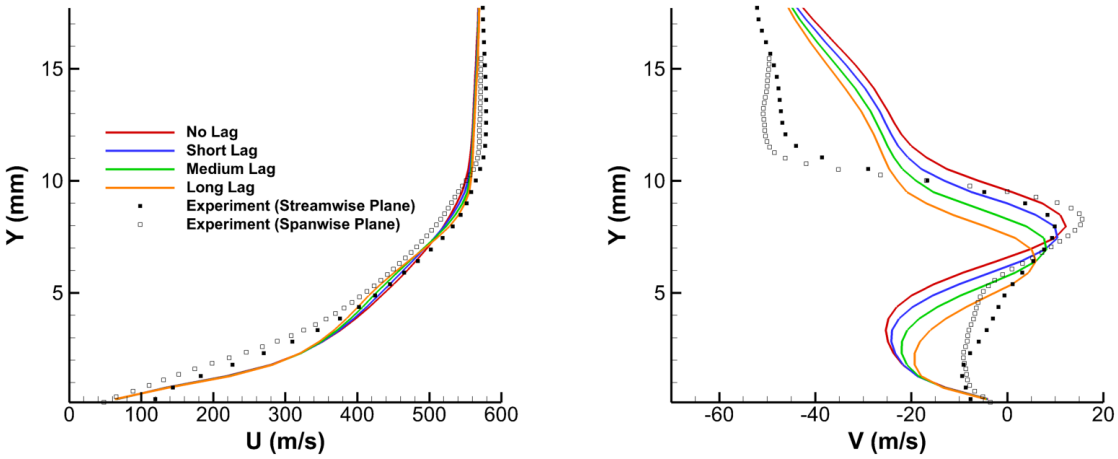

(a) u velocity profiles.

(b) v velocity profiles.

Figure B.4: Velocity profiles at $x = 38.76$ mm, Standard case.

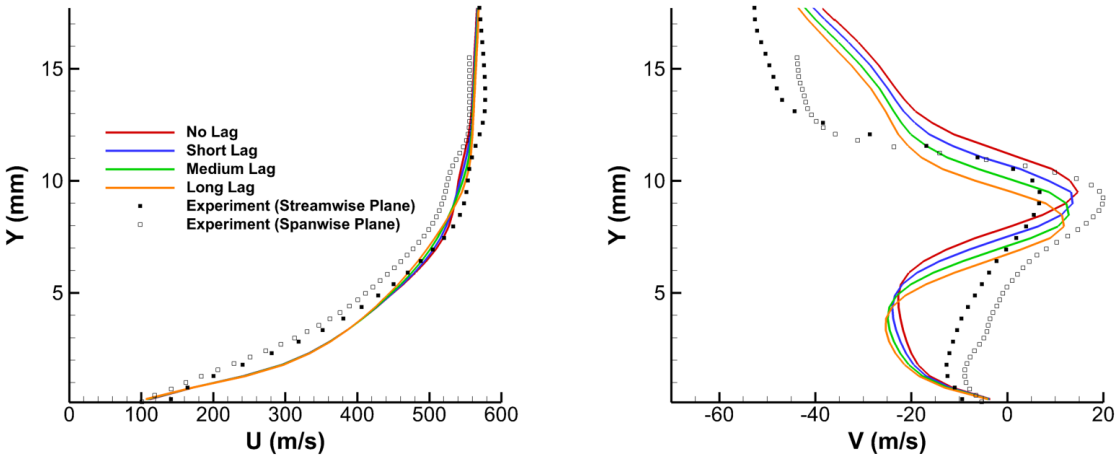

(a) u velocity profiles.

(b) v velocity profiles.

Figure B.5: Velocity profiles at $x = 41.76$ mm, Standard case.

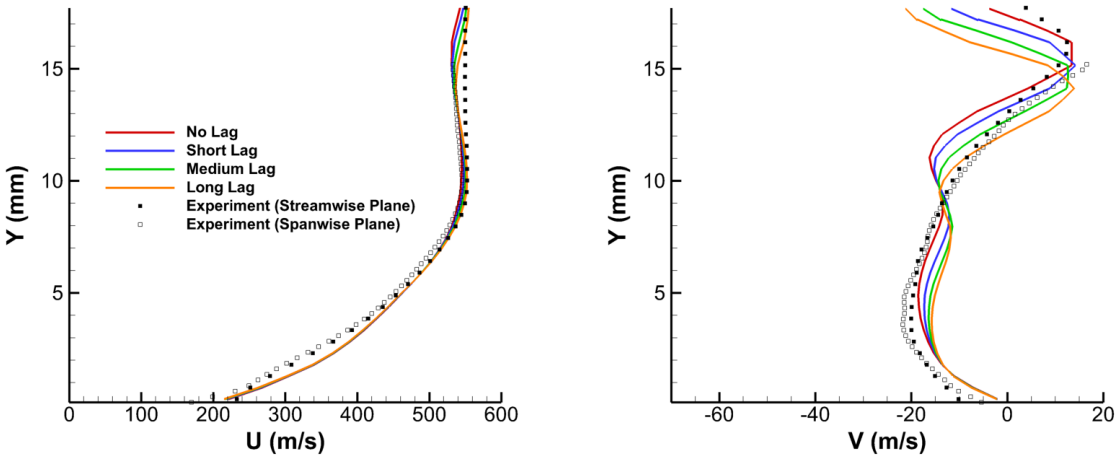

(a) u velocity profiles.

(b) v velocity profiles.

Figure B.6: Velocity profiles at $x = 53.76$ mm, Standard case.

B.2 Combined Case

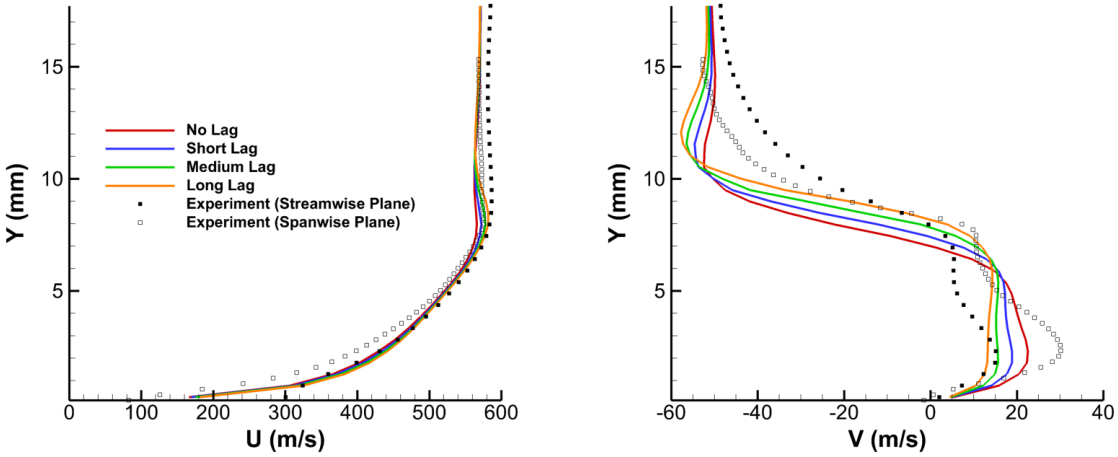

(a) u velocity profiles. (b) v velocity profiles.

Figure B.7: Velocity profiles at $x = 26.76$ mm, Combined case.

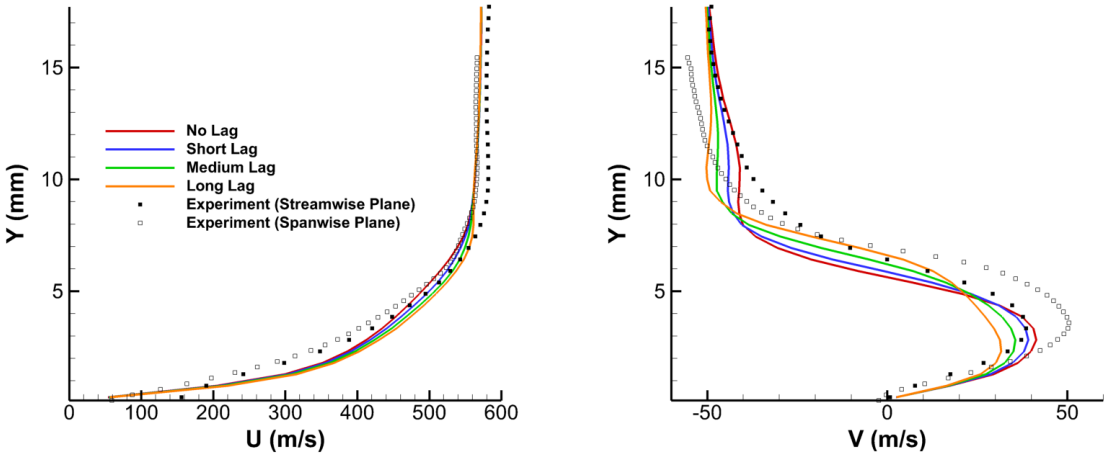

(a) u velocity profiles. (b) v velocity profiles.

Figure B.8: Velocity profiles at $x = 30.76$ mm, Combined case.

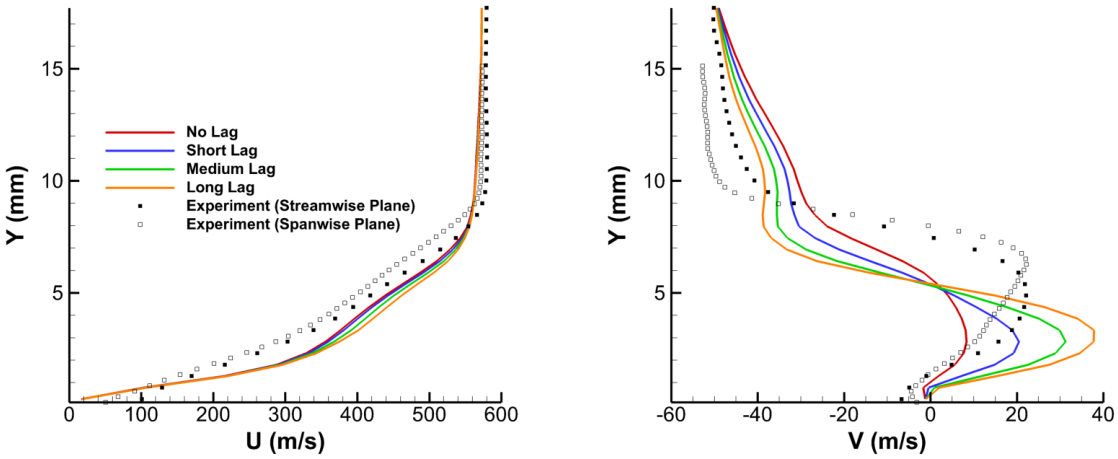

(a) u velocity profiles.

(b) v velocity profiles.

Figure B.9: Velocity profiles at $x = 34.76$ mm, Combined case.

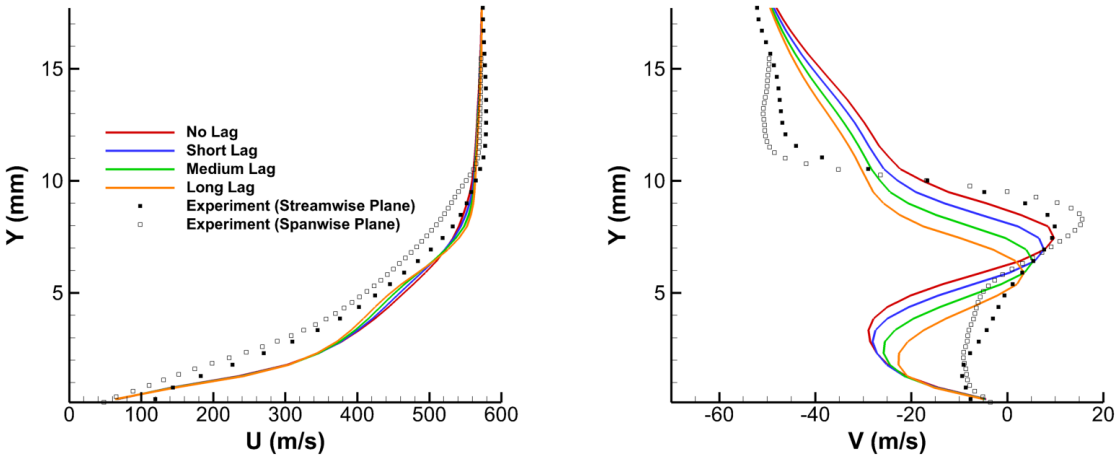

(a) u velocity profiles.

(b) v velocity profiles.

Figure B.10: Velocity profiles at $x = 38.76$ mm, Combined case.

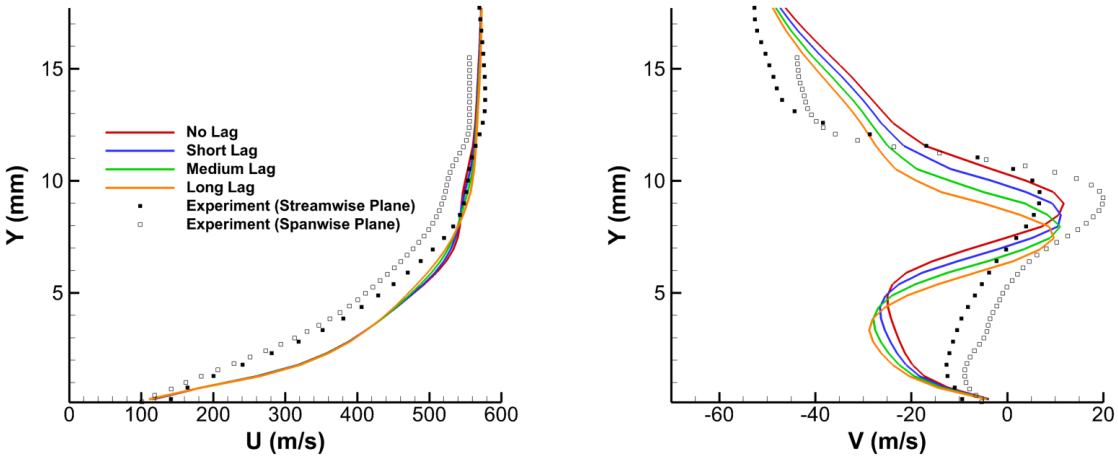

(a) u velocity profiles.

(b) v velocity profiles.

Figure B.11: Velocity profiles at $x = 41.76$ mm, Combined case.

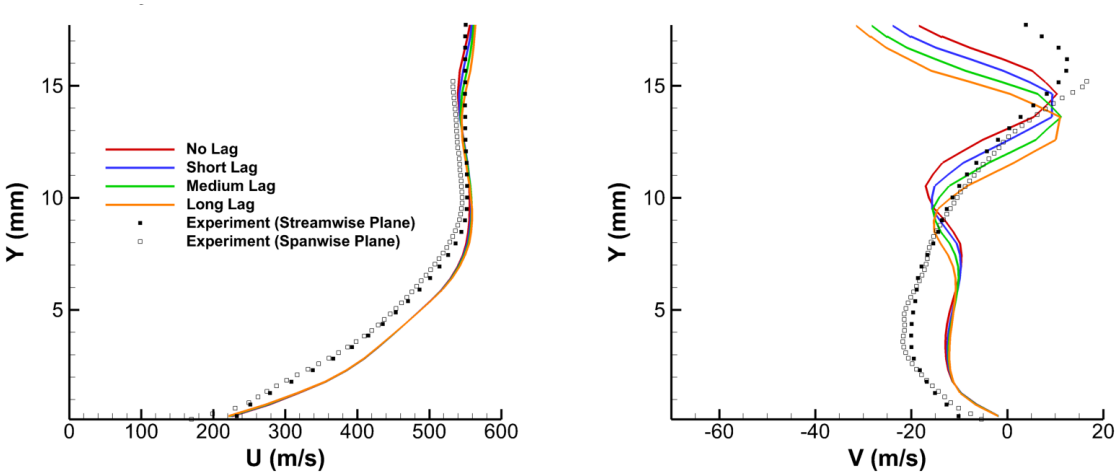

(a) u velocity profiles.

(b) v velocity profiles.

Figure B.12: Velocity profiles at $x = 53.76$ mm, Combined case.

B.3 Modified Geometry, Isothermal, and Trip Cases

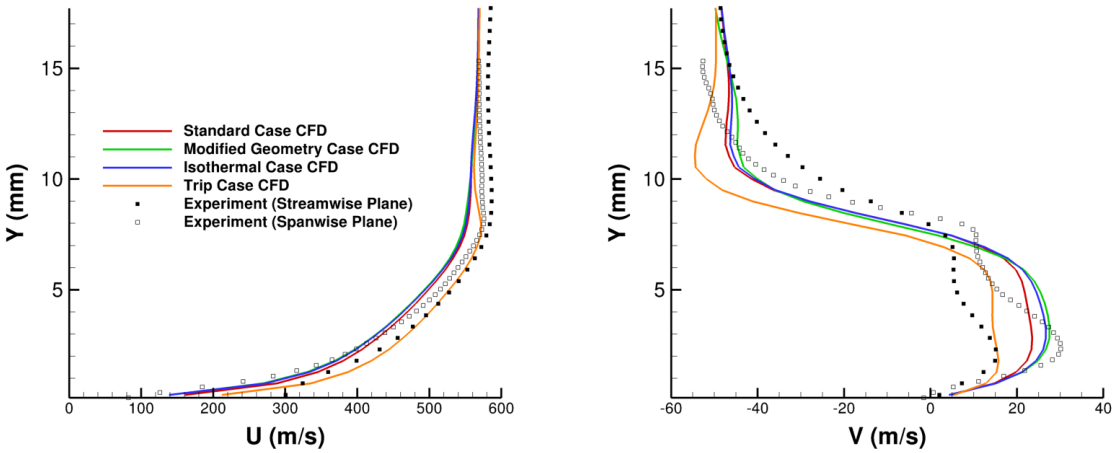

(a) u velocity profiles.

(b) v velocity profiles.

Figure B.13: Velocity profiles at $x = 26.76$ mm, various cases.

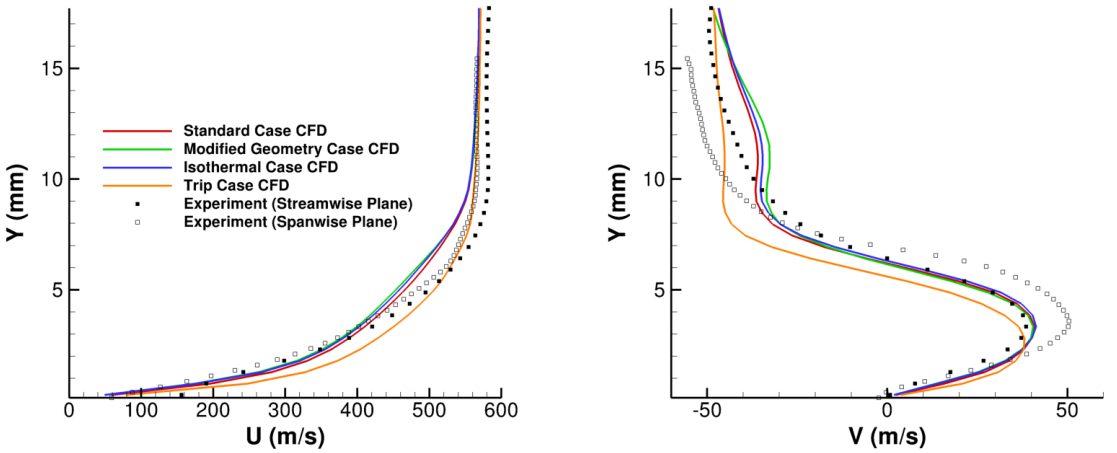

(a) u velocity profiles.

(b) v velocity profiles.

Figure B.14: Velocity profiles at $x = 30.76$ mm, various cases.

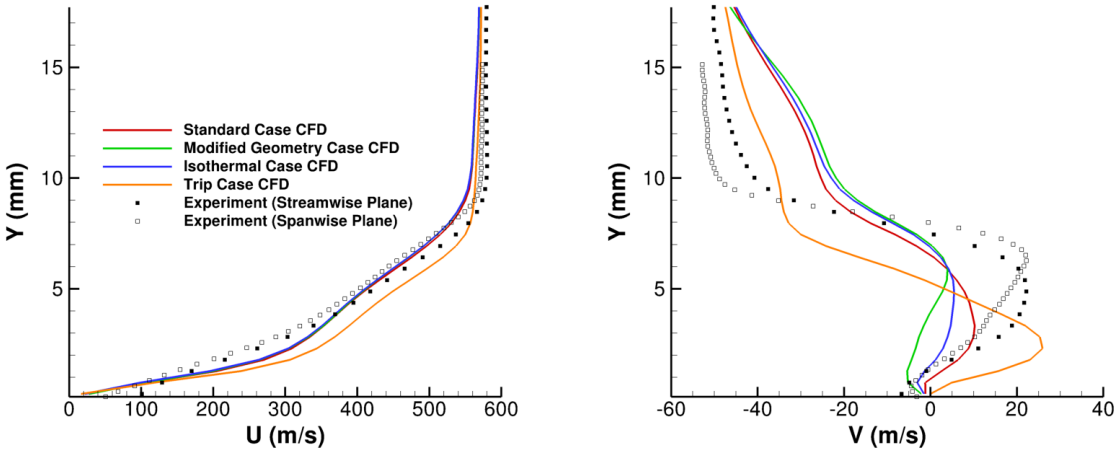

(a) u velocity profiles.

(b) v velocity profiles.

Figure B.15: Velocity profiles at $x = 34.76$ mm, various cases.

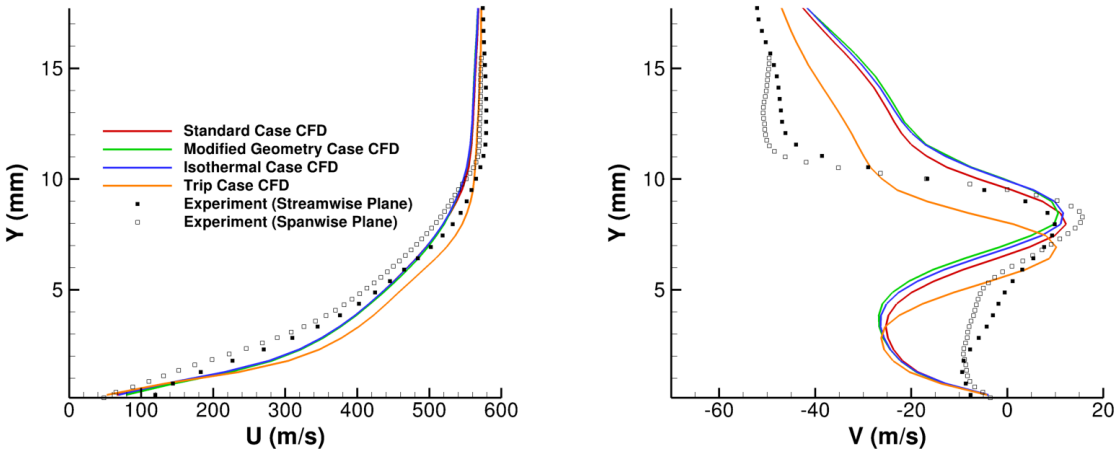

(a) u velocity profiles.

(b) v velocity profiles.

Figure B.16: Velocity profiles at $x = 38.76$ mm, various cases.

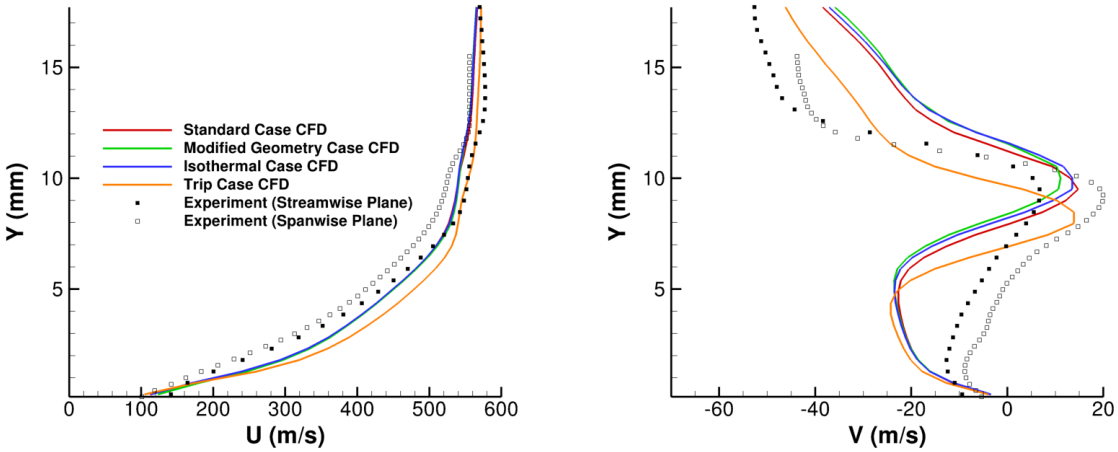

(a) u velocity profiles.

(b) v velocity profiles.

Figure B.17: Velocity profiles at $x = 41.76$ mm, various cases.

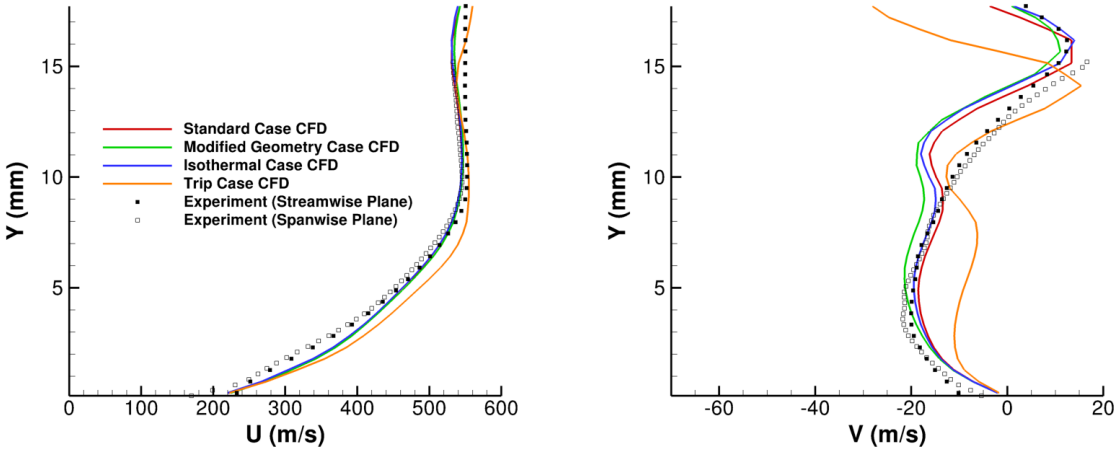

(a) u velocity profiles.

(b) v velocity profiles.

Figure B.18: Velocity profiles at $x = 53.76$ mm, various cases.

B.4 TKE and MUT Cases

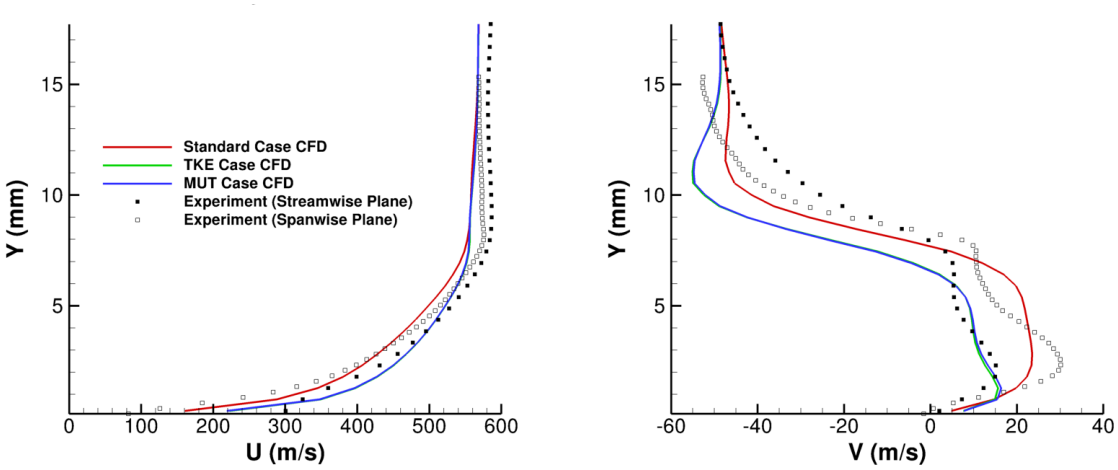

(a) u velocity profiles.

(b) v velocity profiles.

Figure B.19: Velocity profiles at $x = 26.76$ mm, TKE and MUT cases.

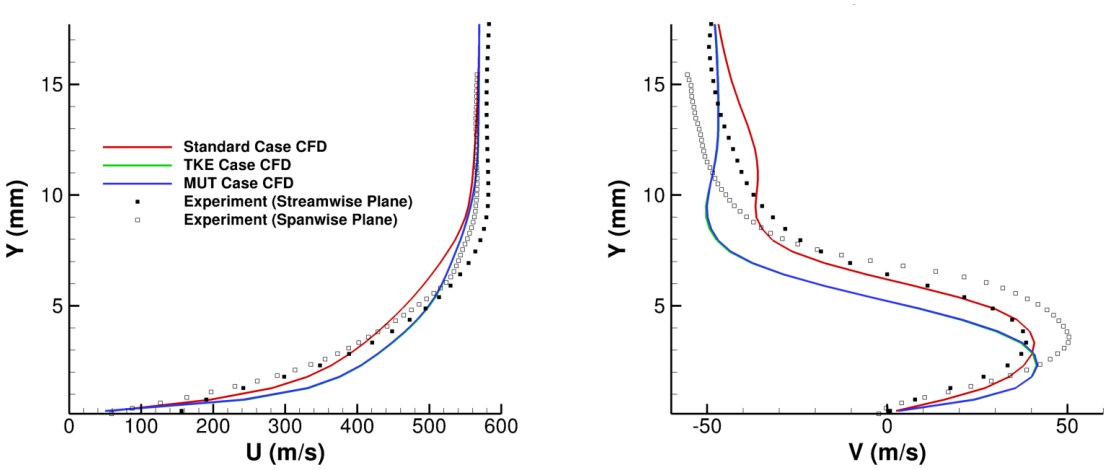

(a) u velocity profiles.

(b) v velocity profiles.

Figure B.20: Velocity profiles at $x = 30.76$ mm, TKE and MUT cases.

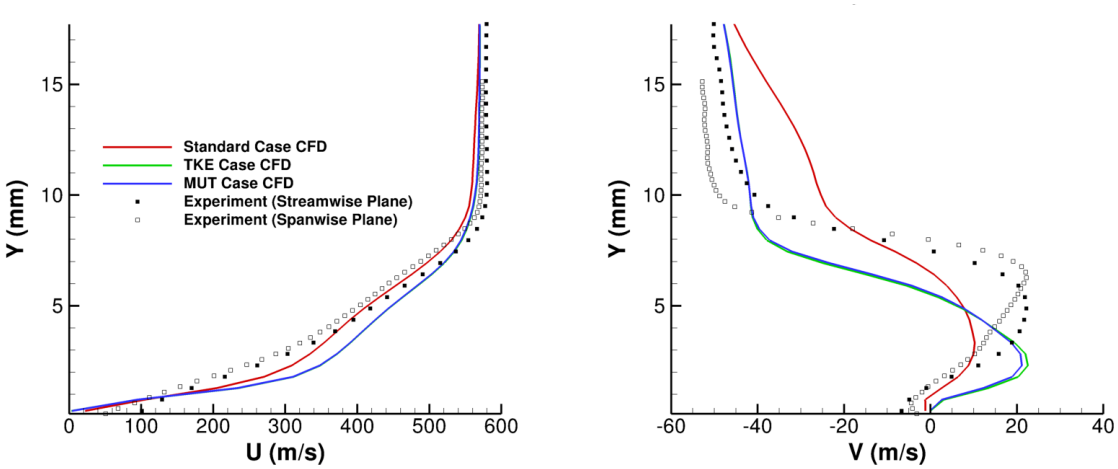

(a) u velocity profiles.

(b) v velocity profiles.

Figure B.21: Velocity profiles at $x = 34.76$ mm, TKE and MUT cases.

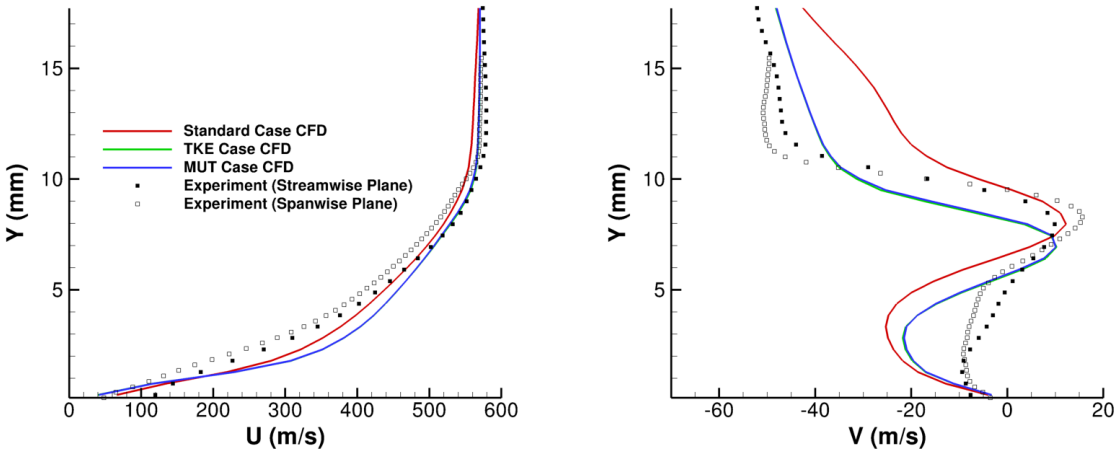

(a) u velocity profiles.

(b) v velocity profiles.

Figure B.22: Velocity profiles at $x = 38.76$ mm, TKE and MUT cases.

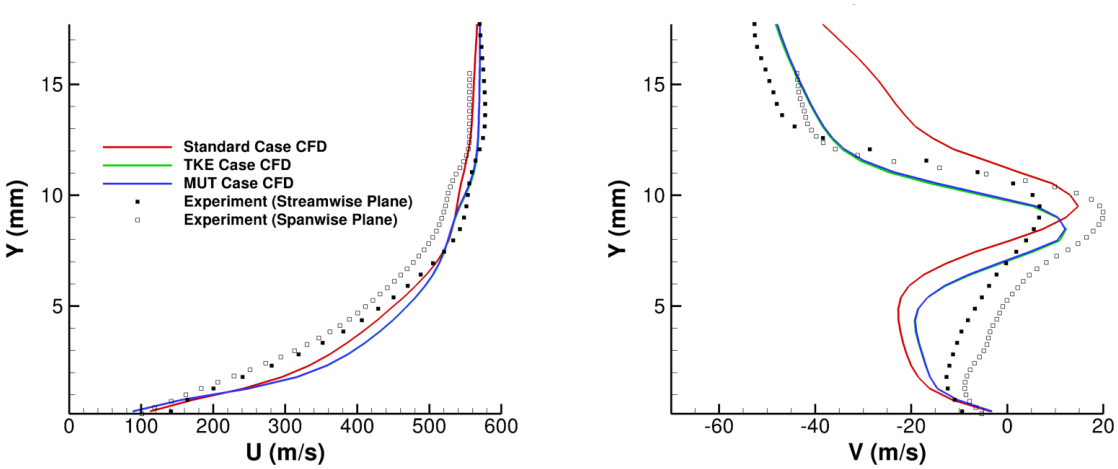

(a) u velocity profiles.

(b) v velocity profiles.

Figure B.23: Velocity profiles at $x = 41.76$ mm, TKE and MUT cases.

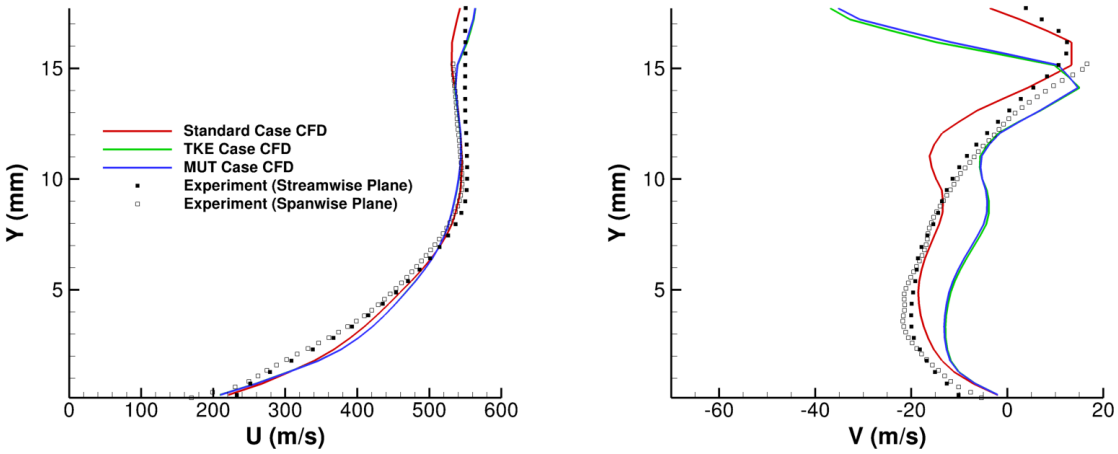

(a) u velocity profiles.

(b) v velocity profiles.

Figure B.24: Velocity profiles at $x = 53.76$ mm, TKE and MUT cases.

B.5 Standard Case with Various Turbulence Models

See appendix C for Combined case equivilant.

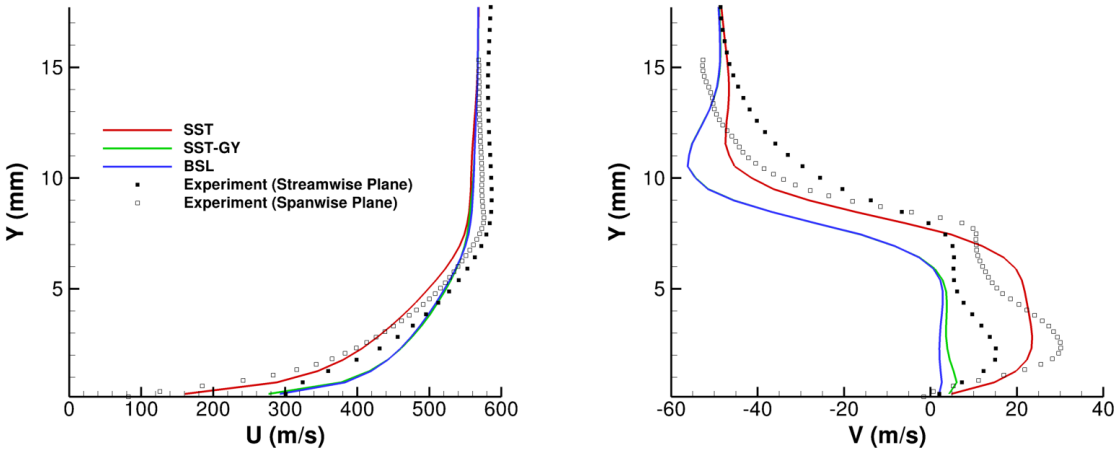

(a) u velocity profiles.

(b) v velocity profiles.

Figure B.25: Velocity profiles at $x = 26.76$ mm, Standard case with various turbulence models.

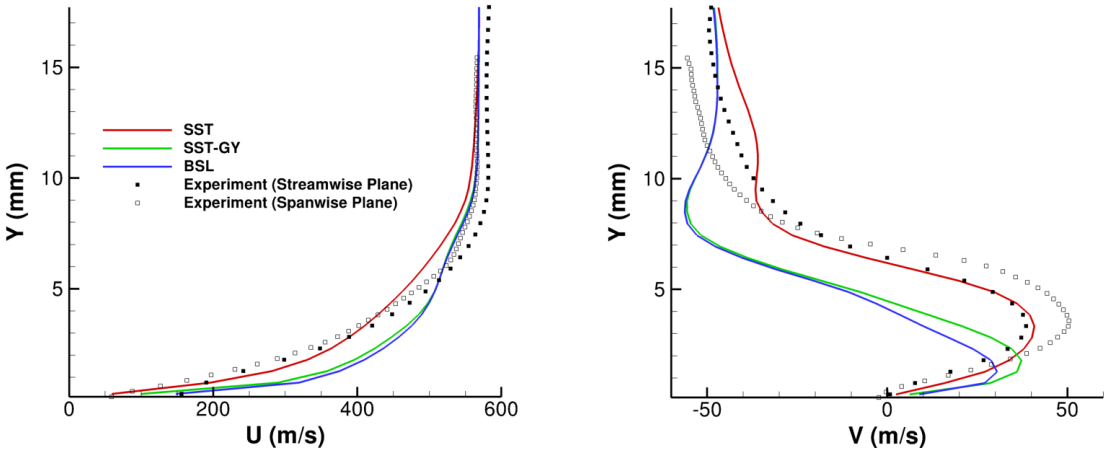

(a) u velocity profiles.

(b) v velocity profiles.

Figure B.26: Velocity profiles at $x = 30.76$ mm, Standard case with various turbulence models.

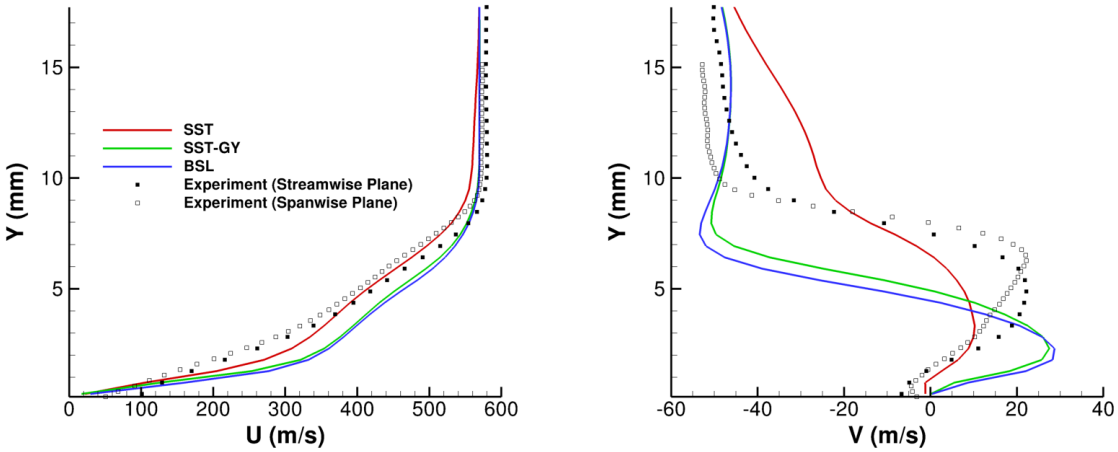

(a) u velocity profiles.

(b) v velocity profiles.

Figure B.27: Velocity profiles at $x = 34.76$ mm, Standard case with various turbulence models.

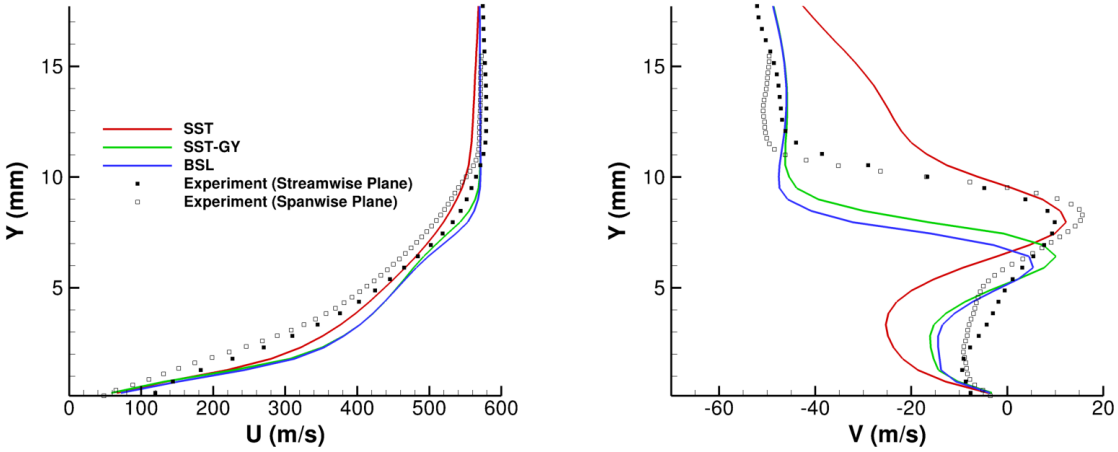

(a) u velocity profiles.

(b) v velocity profiles.

Figure B.28: Velocity profiles at $x = 38.76$ mm, Standard case with various turbulence models.

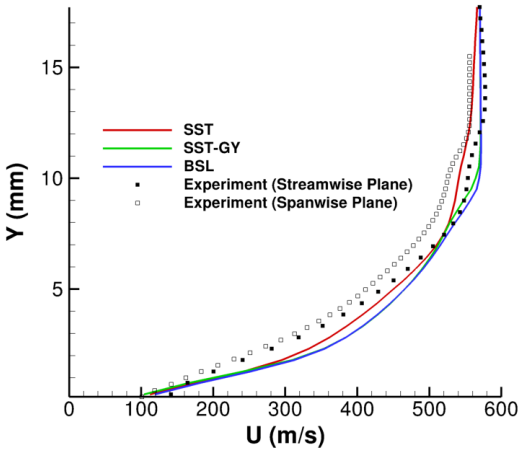

(a) u velocity profiles.

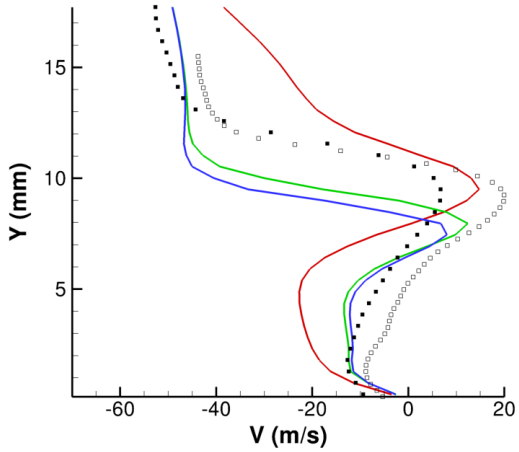

(b) v velocity profiles.

Figure B.29: Velocity profiles at $x = 41.76$ mm, Standard case with various turbulence models.

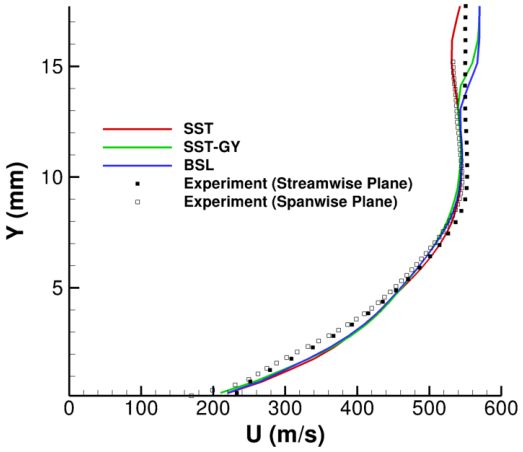

(a) u velocity profiles.

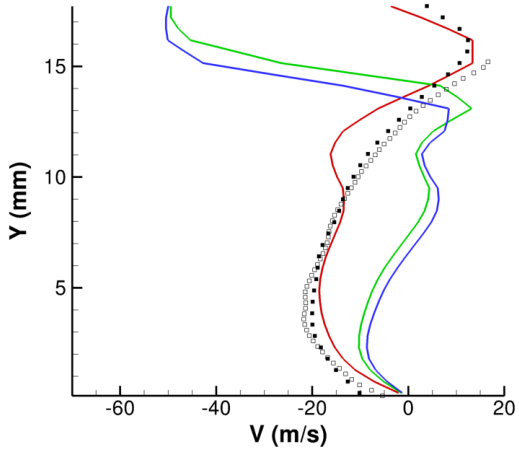

(b) v velocity profiles.

Figure B.30: Velocity profiles at $x = 53.76$ mm, Standard case with various turbulence models.

C Combined Case with Various Turbulence Models

This appendix contains velocity profiles and bottom wall separation plots for the Combined case with the SST-GY and BSL turbulence models. Similar trends were noticed compared to the turbulence model study with the Standard case conditions. However unlike the Standard conditions, the throat blockage was inconsistent with the turbulent shear stress limiter, with blockage values of 0.930% with SST, 0.997% with SST-GY, and 0.988% with BSL. This is most likely because unlike the Standard case conditions, the Combined case conditions modeled the throat region laminar and thus should be independent of turbulence quantities. The discrepancy between the turbulence models shown is therefore due to numerical error.

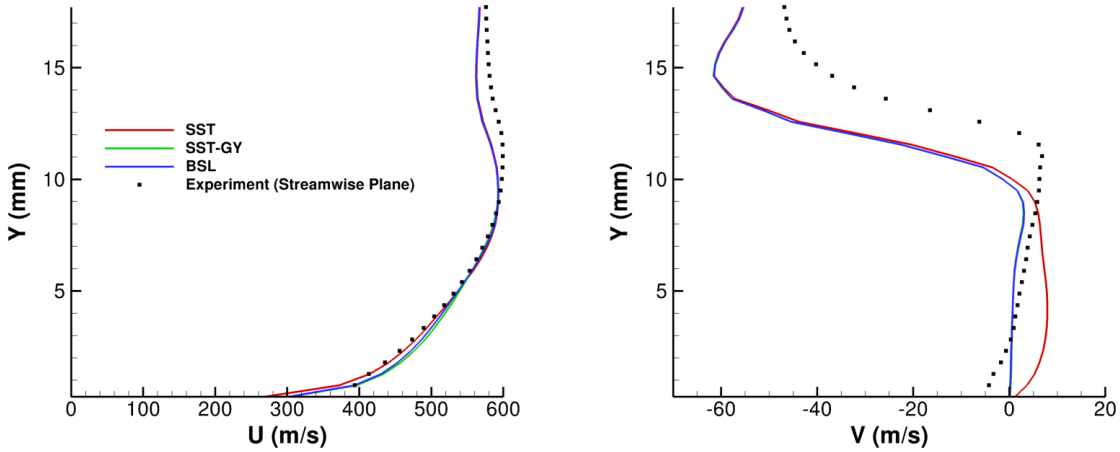

(a) u velocity profiles.

(b) v velocity profiles.

Figure C.1: Velocity profiles at $x = 18.191$ mm, Combined case with various turbulence models.

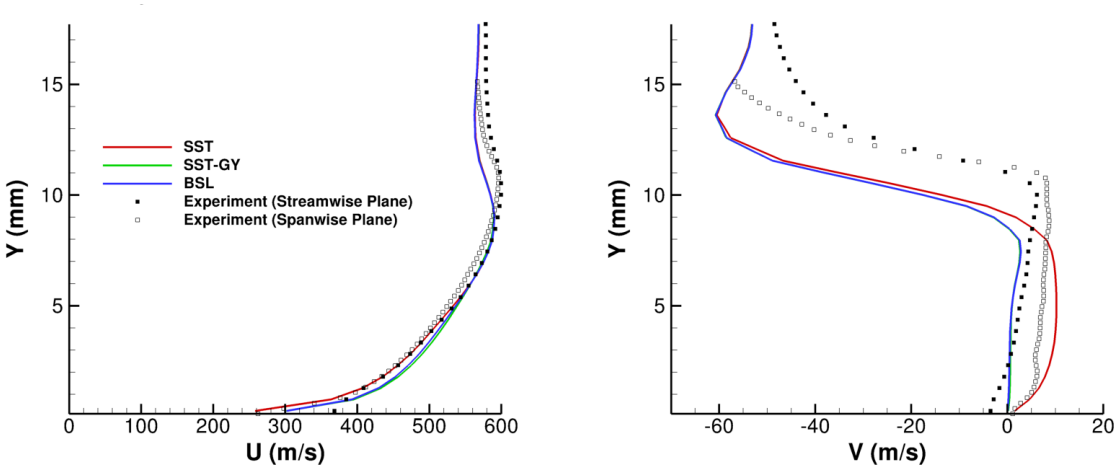

(a) u velocity profiles. (b) v veloicty profiles.

Figure C.2: Velocity profiles at $x = 20.76$ mm, Combined case with various turbulence models.

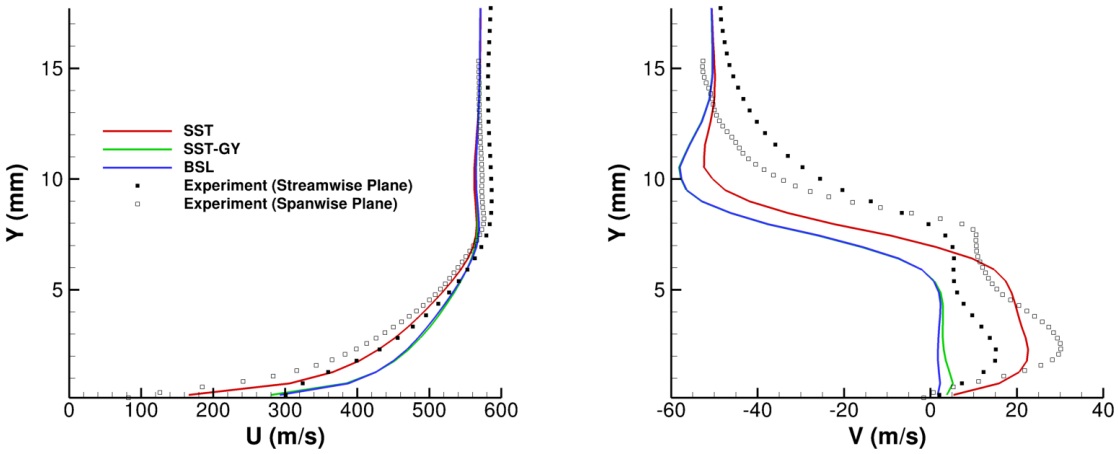

(a) u velocity profiles. (b) v velocity profiles.

Figure C.3: Velocity profiles at $x = 26.76$ mm, Combined case with various turbulence models.

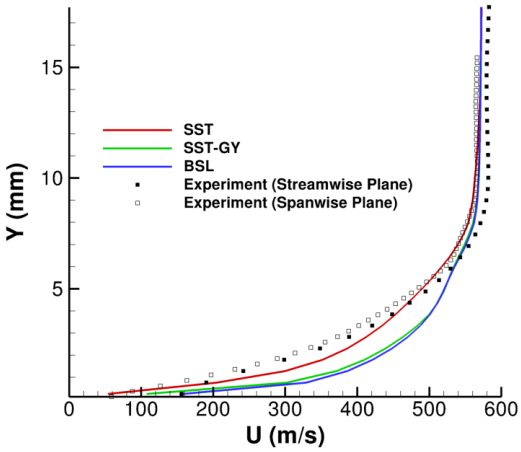

(a) u velocity profiles.

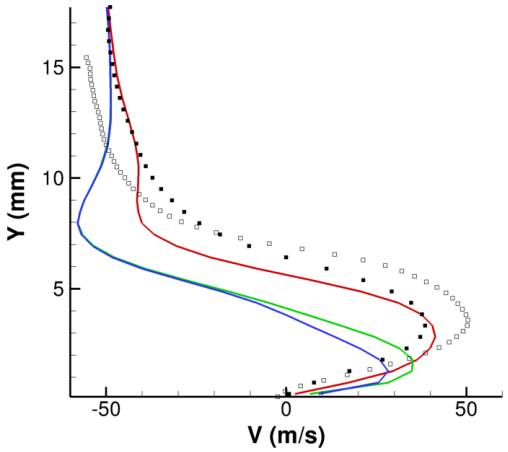

(b) v velocity profiles.

Figure C.4: Velocity profiles at $x = 30.76$ mm, Combined case with various turbulence models.

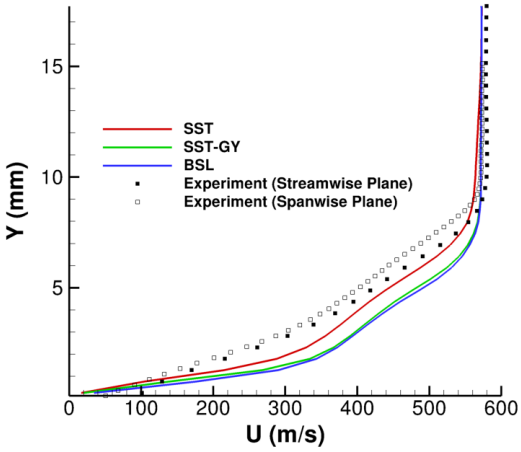

(a) u velocity profiles.

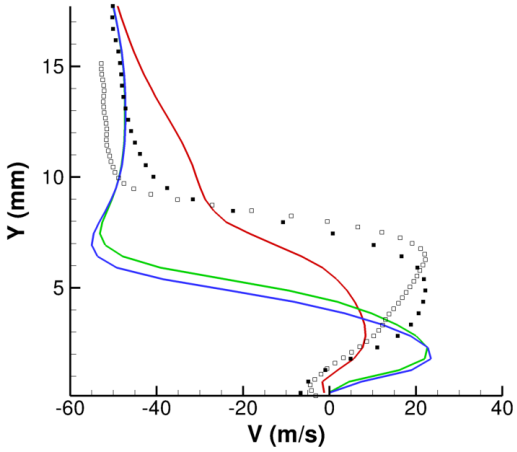

(b) v velocity profiles.

Figure C.5: Velocity profiles at $x = 34.76$ mm, Combined case with various turbulence models.

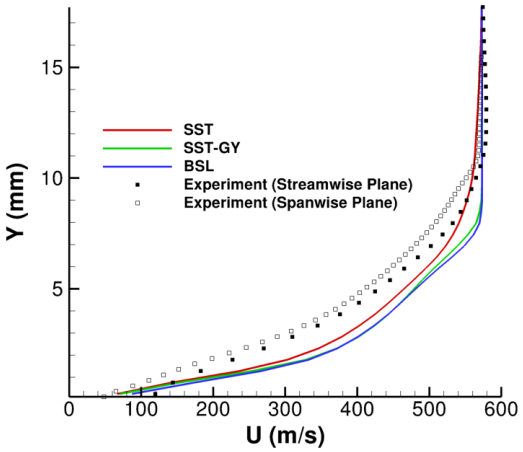

(a) u velocity profiles.

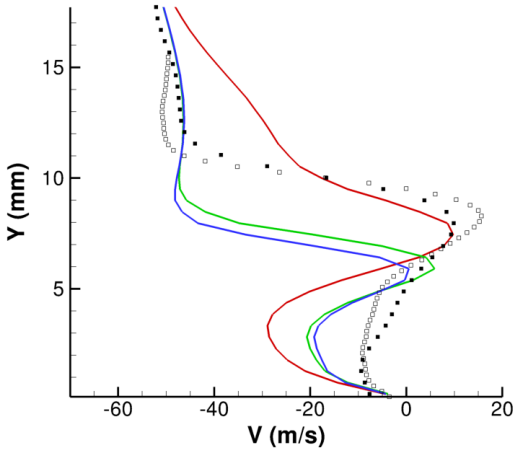

(b) v velocity profiles.

Figure C.6: Velocity profiles at $x = 38.76$ mm, Combined case with various turbulence models.

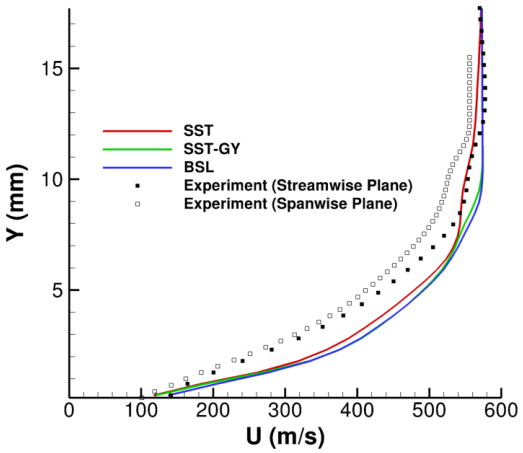

(a) u velocity profiles.

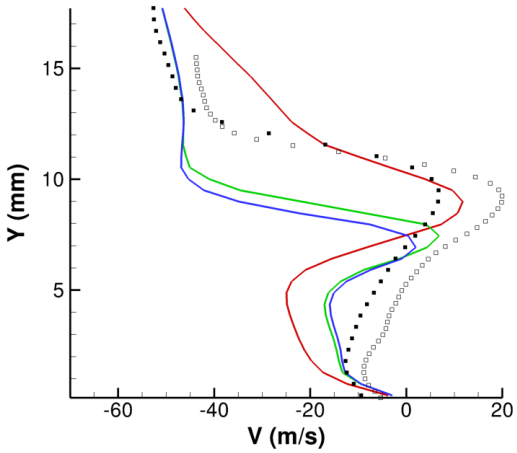

(b) v velocity profiles.

Figure C.7: Velocity profiles at $x = 41.76$ mm, Combined case with various turbulence models.

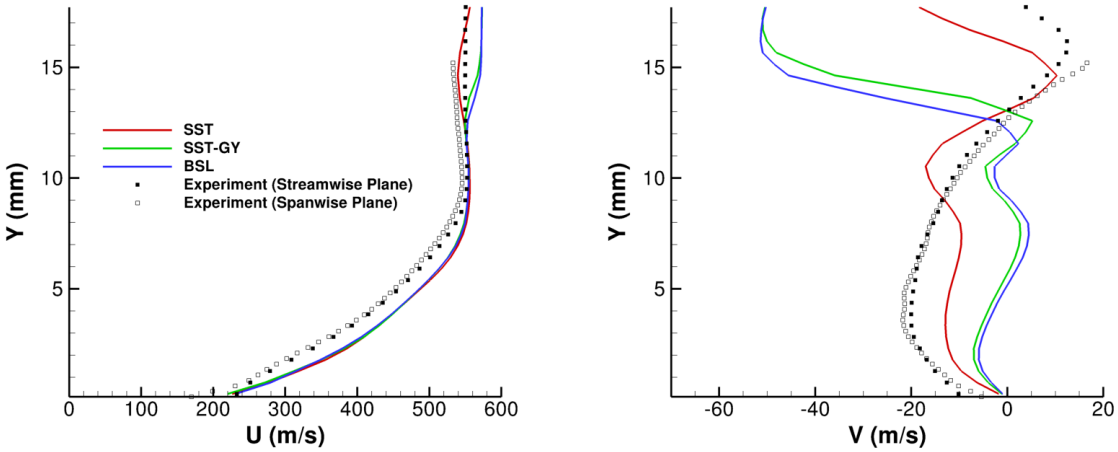

(a) u velocity profiles.

(b) v velocity profiles.

Figure C.8: Velocity profiles at $x = 53.76$ mm, Combined case with various turbulence models.

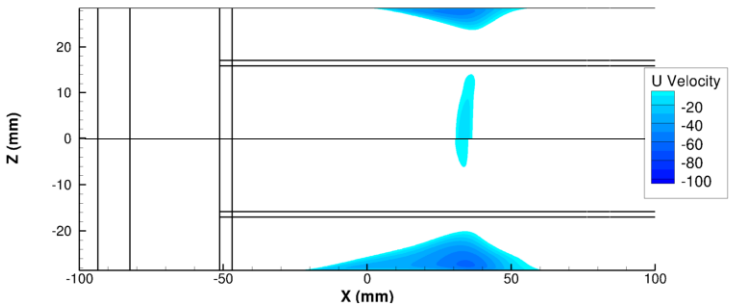

(a) SST-GY (positive span) and SST (negative span).

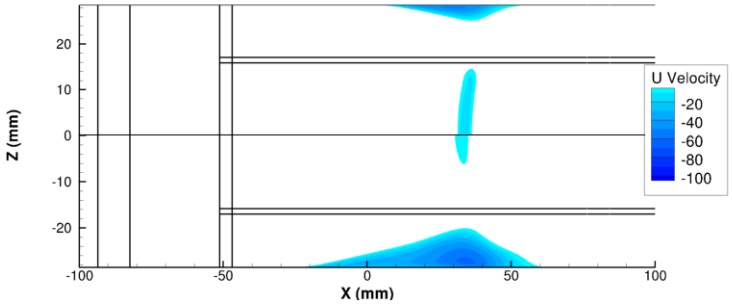

(b) BSL (positive span) and SST (negative span).

Figure C.9: Bottom wall separation underneath the wedge for the Combined case with various turbulence models.

D Shock Angle Calculation

This appendix outlines how the shock angle was computed for the various cases. One would think computing a shock angle would be a trivial exercise, but that is not the case. The method outlined below utilizes v velocity profiles since they vary dramatically after being turned through a wedge angle. The method adopted is then consistent for the experimental as well as the CFD results. The shock angle was defined as the angle of the line formed by two points, denoted as the shock line, and shown in Fig. D.1. The start point of the shock line was chosen to be the wedge leading edge in the streamwise plane as this point is fixed for all cases examined. To find the end point of the shock line, a v velocity profile was first obtained at an axial station of interest. In this case, the axial location was chosen to be the most upstream location within the streamwise data plane ($x = 18.191$ mm). For consistency with the experimental data, the v velocity profile was obtained by interpolating the CFD data onto the PIV grid. Second, the v velocity profile was scaled by the profile aspect ratio to obtain the profile quantity, x':

$$x' = v\frac{y_{max} - y_{min}}{v_{max} - v_{min}} \tag{D.1}$$

Third, the arc length profile was computed, with the arc length defined as:

$$l_i = \sqrt{\left(x'_{i+1} - x'_i\right)^2 + \left(y_{i+1} - y_i\right)^2} + l_{i-1} \tag{D.2}$$

Forth, the first and second derivatives of the arc length with respect to y were computed using a forward differentiating scheme.

$$\left(\frac{dl}{dy}\right)_i = \frac{l_{i+1} - l_i}{y_{i+1} - y_i} \tag{D.3}$$

$$\left(\frac{d^2l}{dy^2}\right)_i = \frac{\left(\frac{dl}{dy}\right)_{i+1} - \left(\frac{dl}{dy}\right)_i}{y_{i+1} - y_i} \tag{D.4}$$

The point with the maximum $\frac{d^2l}{dy^2}$ became the end point for the shock line. The shock angle was then computed as:

$$\beta = \tan^{-1}\left(\frac{\Delta y}{\Delta x}\right) \tag{D.5}$$

For a visual example, see Fig. D.2 through Fig. D.4, which show the above mentioned profiles for the Standard case.

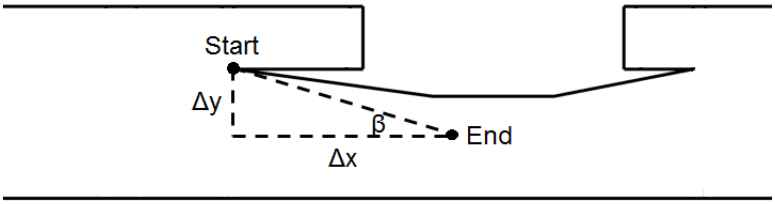

Figure D.1: Shock angle diagram/nomenclature.

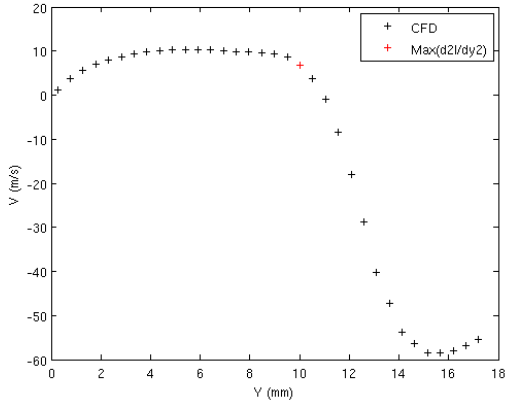

(a) v velocity profile at $x = 18.191$ mm.

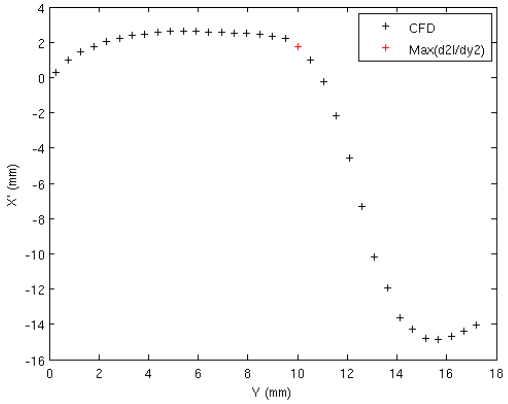

(b) x' profile at $x = 18.191$ mm.

Figure D.2: Velocity profiles for determining shock line end location (Standard case shown).

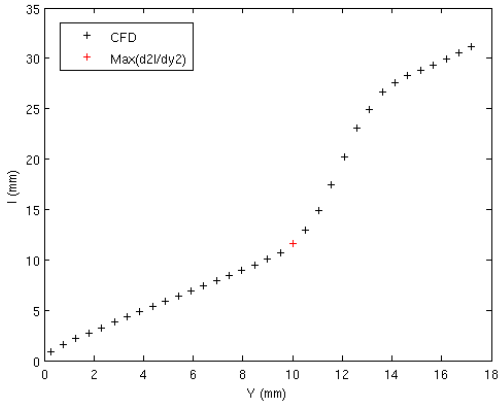

Figure D.3: Arc length profile for determining shock line end location (Standard case shown).

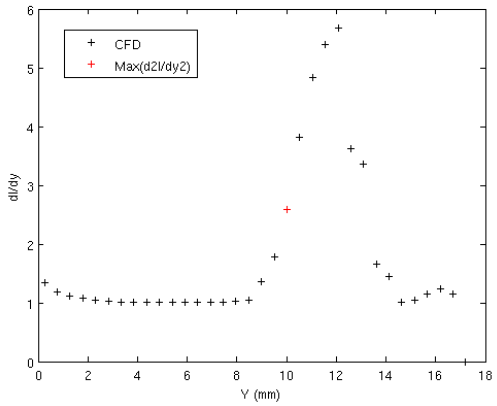

(a) $\frac{dl}{dy}$ profile at $x = 18.191$ mm.

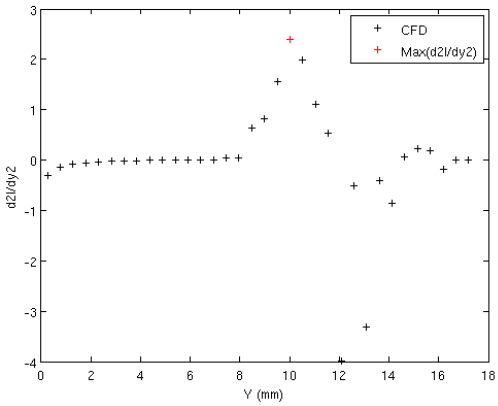

(b) $\frac{d^2l}{dy^2}$ profile at $x = 18.191$ mm.

Figure D.4: Derivative profiles for determining shock line end location (Standard case shown).

E Simulation Checklists

Checklists for the simulations were used to document each run in a consistent manner as outlined by Galbraith [3].

E.1 Initial

Pre-Processing	
Orient meshes	✓
No negative volumes	✓
Check boundary conditions for gaps	✓
Initial Solution	None
Check reference conditions	✓
RefMach	2.75
XKInf	1E-2
RetInf	0.3
RefL (m)	0.06985
Ttot (K)	292.778
Ptot (Pa)	101125
Check the initial solution	✓
Remove orphan nodes	✓
Use most resent INTOUT file	✓

Input File	
Spatial order (FSO)	1
Time order (TFOSO)	1
Time-step scaling flag (ITIME)	4
CFL	0.5-2
Turbulence CFL (CFLT)	1
Turbulence order (FSOT)	1
Turbulence model	SST
Turbulent Input Quantities	
K	1E-2
Epsilon	0.1
Reference Quantities	
Mach	2.75
Tref (R)	205.771
Re	636160

Post Processing	
Iterations (Coarse, Medium, Fine)	2000, 2000, 2000
Dimensionalize the solution	✓
Comments	Unconverged

E.2 Standard Case

Pre-Processing	
Orient meshes	✓
No negative volumes	✓
Check boundary conditions for gaps	✓
Initial Solution	Initial
Check reference conditions	✓
RefMach	2.75
XKInf	1E-6
RetInf	0.3
RefL (m)	0.06985
Ttot (K)	295.7
Ptot (Pa)	98000
Check the initial solution	✓
Remove orphan nodes	✓
Use most resent INTOUT file	✓

Input File	
Spatial order (FSO)	3
Time order (TFOSO)	1
Time-step scaling flag (ITIME)	1
CFL	5-20
Turbulence CFL (CFLT)	1
Turbulence order (FSOT)	1
Turbulence model	SST
Turbulent Input Quantities	
K	1E-6
Epsilon	0.3
Reference Quantities	
Mach	2.75
Tref (R)	211.845
Re	592877

Post Processing	
Iterations (Coarse, Medium, Fine)	0, 0, 20000
Dimensionalize the solution	✓
Comments	Converged

E.3 Isothermal Case

Pre-Processing	
Orient meshes	✓
No negative volumes	✓
Check boundary conditions for gaps	✓
Initial Solution	Standard Case
Check reference conditions	✓
RefMach	2.75
XKInf	1E-6
RetInf	0.3
RefL (m)	0.06985
Ttot (K)	295.7
Ptot (Pa)	98000
Check the initial solution	✓
Remove orphan nodes	✓
Use most resent INTOUT file	✓

Input File	
Spatial order (FSO)	3
Time order (TFOSO)	1
Time-step scaling flag (ITIME)	1
CFL	5-20
Turbulence CFL (CFLT)	1
Turbulence order (FSOT)	1
Turbulence model	SST
Turbulent Input Quantities	
K	1E-6
Epsilon	0.3
Reference Quantities	
Mach	2.75
Tref (R)	211.845
Re	592877

Post Processing	
Iterations (Coarse, Medium, Fine)	0, 0, 20000
Dimensionalize the solution	✓
Comments	Converged

E.4 Modified Geometry Case

Pre-Processing	
Orient meshes	✓
No negative volumes	✓
Check boundary conditions for gaps	✓
Initial Solution	Initial
Check reference conditions	✓
RefMach	2.75
XKInf	1E-6
RetInf	0.3
RefL (m)	0.06985
Ttot (K)	295.7
Ptot (Pa)	98000
Check the initial solution	✓
Remove orphan nodes	✓
Use most resent INTOUT file	✓

Input File	
Spatial order (FSO)	3
Time order (TFOSO)	1
Time-step scaling flag (ITIME)	1
CFL	5-20
Turbulence CFL (CFLT)	1
Turbulence order (FSOT)	1
Turbulence model	SST
Turbulent Input Quantities	
K	1E-6
Epsilon	0.3
Reference Quantities	
Mach	2.75
Tref (R)	211.845
Re	592877

Post Processing	
Iterations (Coarse, Medium, Fine)	0, 0, 20000
Dimensionalize the solution	✓
Comments	Converged

E.5 All-Laminar Case

Pre-Processing	
Orient meshes	✓
No negative volumes	✓
Check boundary conditions for gaps	✓
Initial Solution	Initial
Check reference conditions	✓
RefMach	2.75
XKInf	1E-6
RetInf	0.3
RefL (m)	0.06985
Ttot (K)	295.7
Ptot (Pa)	98000
Check the initial solution	✓
Remove orphan nodes	✓
Use most resent INTOUT file	✓

Input File	
Spatial order (FSO)	3
Time order (TFOSO)	1
Time-step scaling flag (ITIME)	1
CFL	5-20
Turbulence CFL (CFLT)	1
Turbulence order (FSOT)	1
Turbulence model	SST
Turbulent Input Quantities	
K	1E-6
Epsilon	0.3
Reference Quantities	
Mach	2.75
Tref (R)	211.845
Re	592877

Post Processing	
Iterations (Coarse, Medium, Fine)	0, 0, 20000
Dimensionalize the solution	✓
Comments	Converged

E.6 Trip Case

Pre-Processing	
Orient meshes	✓
No negative volumes	✓
Check boundary conditions for gaps	✓
Initial Solution	All-Laminar Case
Check reference conditions	✓
RefMach	2.75
XKInf	1E-6
RetInf	0.3
RefL (m)	0.06985
Ttot (K)	295.7
Ptot (Pa)	98000
Check the initial solution	✓
Remove orphan nodes	✓
Use most resent INTOUT file	✓

Input File	
Spatial order (FSO)	3
Time order (TFOSO)	1
Time-step scaling flag (ITIME)	1
CFL	5-20
Turbulence CFL (CFLT)	1
Turbulence order (FSOT)	1
Turbulence model	SST
Turbulent Input Quantities	
K	1E-6
Epsilon	0.3
Reference Quantities	
Mach	2.75
Tref (R)	211.845
Re	592877

Post Processing	
Iterations (Coarse, Medium, Fine)	0, 0, 10000
Dimensionalize the solution	✓
Comments	Converged

E.7 Combined Case

Pre-Processing	
Orient meshes	✓
No negative volumes	✓
Check boundary conditions for gaps	✓
Initial Solution	Modified Geometry Case
Check reference conditions	✓
RefMach	2.75
XKInf	1E-6
RetInf	0.3
RefL (m)	0.06985
Ttot (K)	295.7
Ptot (Pa)	98000
Check the initial solution	✓
Remove orphan nodes	✓
Use most resent INTOUT file	✓

Input File	
Spatial order (FSO)	3
Time order (TFOSO)	1
Time-step scaling flag (ITIME)	1
CFL	5-20
Turbulence CFL (CFLT)	1
Turbulence order (FSOT)	1
Turbulence model	SST
Turbulent Input Quantities	
K	1E-6
Epsilon	0.3
Reference Quantities	
Mach	2.75
Tref (R)	211.845
Re	592877

Post Processing	
Iterations (Coarse, Medium, Fine)	0, 0, 20000
Dimensionalize the solution	✓
Comments	Converged

E.8 TKE Case

Pre-Processing	
Orient meshes	✓
No negative volumes	✓
Check boundary conditions for gaps	✓
Initial Solution	Initial
Check reference conditions	✓
RefMach	2.75
XKInf	1E-2
RetInf	0.3
RefL (m)	0.06985
Ttot (K)	295.7
Ptot (Pa)	98000
Check the initial solution	✓
Remove orphan nodes	✓
Use most resent INTOUT file	✓

Input File	
Spatial order (FSO)	3
Time order (TFOSO)	1
Time-step scaling flag (ITIME)	1
CFL	5-20
Turbulence CFL (CFLT)	1
Turbulence order (FSOT)	1
Turbulence model	SST
Turbulent Input Quantities	
K	1E-2
Epsilon	0.3
Reference Quantities	
Mach	2.75
Tref (R)	211.845
Re	592877

Post Processing	
Iterations (Coarse, Medium, Fine)	0, 0, 20000
Dimensionalize the solution	✓
Comments	Converged

E.9 MUT Case

Pre-Processing	
Orient meshes	✓
No negative volumes	✓
Check boundary conditions for gaps	✓
Initial Solution	Initial
Check reference conditions	✓
RefMach	2.75
XKInf	1E-2
RetInf	3.0
RefL (m)	0.06985
Ttot (K)	295.7
Ptot (Pa)	98000
Check the initial solution	✓
Remove orphan nodes	✓
Use most resent INTOUT file	✓

Input File	
Spatial order (FSO)	3
Time order (TFOSO)	1
Time-step scaling flag (ITIME)	1
CFL	5-20
Turbulence CFL (CFLT)	1
Turbulence order (FSOT)	1
Turbulence model	SST
Turbulent Input Quantities	
K	1E-2
Epsilon	3.0
Reference Quantities	
Mach	2.75
Tref (R)	211.845
Re	592877

Post Processing	
Iterations (Coarse, Medium, Fine)	0, 0, 20000
Dimensionalize the solution	✓
Comments	Converged

E.10 Standard Case with SST-GY

Pre-Processing	
Orient meshes	✓
No negative volumes	✓
Check boundary conditions for gaps	✓
Initial Solution	Standard Case
Check reference conditions	✓
RefMach	2.75
XKInf	1E-6
RetInf	0.3
RefL (m)	0.06985
Ttot (K)	295.7
Ptot (Pa)	98000
Check the initial solution	✓
Remove orphan nodes	✓
Use most resent INTOUT file	✓

Input File	
Spatial order (FSO)	3
Time order (TFOSO)	1
Time-step scaling flag (ITIME)	1
CFL	5-20
Turbulence CFL (CFLT)	1
Turbulence order (FSOT)	1
Turbulence model	SST-GY
Turbulent Input Quantities	
K	1E-6
Epsilon	0.3
Reference Quantities	
Mach	2.75
Tref (R)	211.845
Re	592877

Post Processing	
Iterations (Coarse, Medium, Fine)	0, 0, 20000
Dimensionalize the solution	✓
Comments	Converged

E.11 Standard Case with BSL

Pre-Processing	
Orient meshes	✓
No negative volumes	✓
Check boundary conditions for gaps	✓
Initial Solution	Standard Case with SST-GY
Check reference conditions	✓
RefMach	2.75
XKInf	1E-6
RetInf	0.3
RefL (m)	0.06985
Ttot (K)	295.7
Ptot (Pa)	98000
Check the initial solution	✓
Remove orphan nodes	✓
Use most resent INTOUT file	✓

Input File	
Spatial order (FSO)	3
Time order (TFOSO)	1
Time-step scaling flag (ITIME)	1
CFL	5-20
Turbulence CFL (CFLT)	1
Turbulence order (FSOT)	1
Turbulence model	BSL
Turbulent Input Quantities	
K	1E-6
Epsilon	0.3
Reference Quantities	
Mach	2.75
Tref (R)	211.845
Re	592877

Post Processing	
Iterations (Coarse, Medium, Fine)	0, 0, 5000
Dimensionalize the solution	✓
Comments	Converged

E.12 Flat Plate with SST

Pre-Processing	
Orient meshes	✓
No negative volumes	✓
Check boundary conditions for gaps	✓
Initial Solution	None
Check reference conditions	✓
RefMach	0.2
XKInf	1E-6
RetInf	0.3
RefL (ft)	1
Ttot (K)	302.39
Ptot (Pa)	386192
Check the initial solution	✓
Remove orphan nodes	✓
Use most resent INTOUT file	✓

Input File	
Spatial order (FSO)	3
Time order (TFOSO)	1
Time-step scaling flag (ITIME)	1
CFL	5-40
Turbulence CFL (CFLT)	1
Turbulence order (FSOT)	1
Turbulence model	SST
Turbulent Input Quantities	
K	1E-6
Epsilon	0.3
Reference Quantities	
Mach	0.2
Tref (R)	540
Re	5E6

Post Processing	
Iterations (Coarse, Medium, Fine)	5000, 5000, 220000
Dimensionalize the solution	✓
Comments	Converged

E.13 Flat Plate with K-Omega

Pre-Processing	
Orient meshes	✓
No negative volumes	✓
Check boundary conditions for gaps	✓
Initial Solution	Flat Plate with SST
Check reference conditions	✓
RefMach	0.2
XKInf	1E-6
RetInf	0.3
RefL (ft)	1
Ttot (K)	302.39
Ptot (Pa)	386192
Check the initial solution	✓
Remove orphan nodes	✓
Use most resent INTOUT file	✓

Input File	
Spatial order (FSO)	3
Time order (TFOSO)	1
Time-step scaling flag (ITIME)	1
CFL	5-40
Turbulence CFL (CFLT)	1
Turbulence order (FSOT)	1
Turbulence model	K-Omega
Turbulent Input Quantities	
K	1E-6
Epsilon	0.3
Reference Quantities	
Mach	0.2
Tref (R)	540
Re	5E6

Post Processing	
Iterations (Coarse, Medium, Fine)	0, 0, 180000
Dimensionalize the solution	✓
Comments	Converged

E.14 Flat Plate with SST-GY

Pre-Processing	
Orient meshes	✓
No negative volumes	✓
Check boundary conditions for gaps	✓
Initial Solution	Flat Plate with SST
Check reference conditions	✓
RefMach	0.2
XKInf	1E-6
RetInf	0.3
RefL (ft)	1
Ttot (K)	302.39
Ptot (Pa)	386192
Check the initial solution	✓
Remove orphan nodes	✓
Use most resent INTOUT file	✓

Input File	
Spatial order (FSO)	3
Time order (TFOSO)	1
Time-step scaling flag (ITIME)	1
CFL	5-40
Turbulence CFL (CFLT)	1
Turbulence order (FSOT)	1
Turbulence model	SST-GY
Turbulent Input Quantities	
K	1E-6
Epsilon	0.3
Reference Quantities	
Mach	0.2
Tref (R)	540
Re	5E6

Post Processing	
Iterations (Coarse, Medium, Fine)	0, 0, 180000
Dimensionalize the solution	✓
Comments	Converged

E.15 Flat Plate with BSL

Pre-Processing	
Orient meshes	✓
No negative volumes	✓
Check boundary conditions for gaps	✓
Initial Solution	Flat Plate with SST
Check reference conditions	✓
RefMach	0.2
XKInf	1E-6
RetInf	0.3
RefL (ft)	1
Ttot (K)	302.39
Ptot (Pa)	386192
Check the initial solution	✓
Remove orphan nodes	✓
Use most resent INTOUT file	✓

Input File	
Spatial order (FSO)	3
Time order (TFOSO)	1
Time-step scaling flag (ITIME)	1
CFL	5-40
Turbulence CFL (CFLT)	1
Turbulence order (FSOT)	1
Turbulence model	BSL
Turbulent Input Quantities	
K	1E-6
Epsilon	0.3
Reference Quantities	
Mach	0.2
Tref (R)	540
Re	5E6

Post Processing	
Iterations (Coarse, Medium, Fine)	0, 0, 180000
Dimensionalize the solution	✓
Comments	Converged

REPORT DOCUMENTATION PAGE			Form Approved OMB No. 0704-0188

1. REPORT DATE *(DD-MM-YYYY)*	2. REPORT TYPE	3. DATES COVERED *(From - To)*
01-10-2013	Technical Memorandum	

4. TITLE AND SUBTITLE
Understanding the Flow Physics of Shock Boundary-Layer Interactions Using CFD and Numerical Analyses

5a. CONTRACT NUMBER

5b. GRANT NUMBER

5c. PROGRAM ELEMENT NUMBER

6. AUTHOR(S)
Friedlander, David, J.

5d. PROJECT NUMBER

5e. TASK NUMBER

5f. WORK UNIT NUMBER
WBS 984754.02.07.03.13.02

7. PERFORMING ORGANIZATION NAME(S) AND ADDRESS(ES)
National Aeronautics and Space Administration
John H. Glenn Research Center at Lewis Field
Cleveland, Ohio 44135-3191

8. PERFORMING ORGANIZATION REPORT NUMBER
E-18767

9. SPONSORING/MONITORING AGENCY NAME(S) AND ADDRESS(ES)
National Aeronautics and Space Administration
Washington, DC 20546-0001

10. SPONSORING/MONITOR'S ACRONYM(S)
NASA

11. SPONSORING/MONITORING REPORT NUMBER
NASA/TM-2013-218081

12. DISTRIBUTION/AVAILABILITY STATEMENT
Unclassified-Unlimited
Subject Categories: 07 and 64
Available electronically at http://www.sti.nasa.gov
This publication is available from the NASA Center for AeroSpace Information, 443-757-5802

13. SUPPLEMENTARY NOTES
This report was submitted as a dissertation in partial fulfillment of the requirements for the degree of Master of Science to the University of Cincinnati, Cincinnati, Ohio, April 2013.

14. ABSTRACT
Computational fluid dynamic (CFD) analyses of the University of Michigan (UM) Shock/Boundary-Layer Interaction (SBLI) experiments were performed as an extension of the CFD SBLI Workshop held at the 48th AIAA Aerospace Sciences Meeting in 2010. In particular, the UM Mach 2.75 Glass Tunnel with a semi-spanning 7.75° wedge was analyzed in attempts to explore key physics pertinent to SBLI's, including thermodynamic and viscous boundary conditions as well as turbulence modeling. Most of the analyses were 3D CFD simulations using the OVERFLOW flow solver, with additional quasi-1D simulations performed with an in house MATLAB code interfacing with the NIST REFPROP code to explore perfect verses non-ideal air. A fundamental exploration pertaining to the effects of particle image velocimetry (PIV) on post-processing data is also shown. Results from the CFD simulations showed an improvement in agreement with experimental data with key contributions including adding a laminar zone upstream of the wedge and the necessity of mimicking PIV particle lag for comparisons. Results from the quasi-1D simulation showed that there was little difference between perfect and non-ideal air for the configuration presented.

15. SUBJECT TERMS
Shock waves; Boundary layers; Computational fluid dynamics

16. SECURITY CLASSIFICATION OF:			17. LIMITATION OF ABSTRACT	18. NUMBER OF PAGES	19a. NAME OF RESPONSIBLE PERSON
a. REPORT	b. ABSTRACT	c. THIS PAGE			STI Help Desk (email:help@sti.nasa.gov)
U	U	U	UU	126	19b. TELEPHONE NUMBER *(include area code)* 443-757-5802